Surface and Subsurface Damage Quantification using Multi-Device Robotics-based Sensor System and other Non-Destructive Testing Techniques

by

Harsh Rathod
Master of Technology, Nirma University, 2015
Bachelor of Technology, Nirma University, 2013

A Dissertation Submitted in Partial Fulfillment
of the Requirements for the Degree of

DOCTOR OF PHILOSOPHY

in the Department of Civil Engineering

We acknowledge with respect the Lekwungen peoples on whose traditional territory the university stands and the Songhees, Esquimalt and WSÁNEĆ peoples whose historical relationships with the land continue to this day.

Supervisory Committee

Surface and Subsurface Damage Quantification using Multi-Device Robotics-based Sensor System and other Non-Destructive Testing Techniques

by

Harsh Rathod
Master of Technology, Nirma University, 2015
Bachelor of Technology, Nirma University, 2013

Supervisory Committee

Dr. Rishi Gupta, Department of Civil Engineering
Supervisor

Dr. Min Sun, Department of Civil Engineering
Departmental Member

Dr. Caterina Valeo, Department of Mechanical Engineering
Outside Member

Abstract

North American civil infrastructures are aging. According to recent (2016) Canadian infrastructure report card, 33% of the Canadian municipal infrastructures are either in fair or below fair condition. The current deficit of replacing fair and poor municipal bridges (covers 26% of bridges) is 13 billion dollars. According to the latest report (2017) by American Society of Civil Engineers, the entire American infrastructure have been given a D+ condition rating. This includes some of the structural elements of infrastructures that pose a significant risk and there is an urgent need for frequent and effective inspection to ensure the safety of people.

Visual inspection is a commonly used technique to detect and identify surface defects in bridge structures as it has been considered the most feasible method for decades. However, this currently used methodology is inadequate and unreliable as it is highly dependent on subjective human judgment. This labor-intensive approach for inspection requires huge investment in terms of an arrangement of temporary scaffoldings/permanent platforms, ladders, snooper trucks, and sometimes helicopters.

To address these issues associated with visual inspection, the completed research suggests three innovative methods; 1) Combined use of Fuzzy logic and Image Processing Algorithm to quantify surface defects, 2) Unmanned Aerial Vehicle (UAV)-assisted American Association of State Highway and Transportation Officials (AASHTO) guideline-based damage assessment technique, and 3) Patent-pending multi-device robotics-based sensor data acquisition system for mapping and assessing defects in civil structures.

To detect and quantify subsurface defects such as voids and delamination using a UAV system, another patent-pending UAV-based acoustic method is developed. It is a novel inspection apparatus that comprises of an acoustic signal generator coupled to a UAV. The acoustic signal generator includes a hammer to produce an acoustic signal in a structure using a UAV.

An outcome of this innovative research is the development of a model to refine multiple commercially available NDT techniques' data to detect and quantify subsurface defects. To achieve this, a total of nine 1800 mm × 460 mm reinforced concrete slabs with varying

thicknesses of 100 mm, 150 mm and 200 mm are prepared. These slabs are designed to have artificially simulated defects like voids, debonding, honeycombing, and corrosion. To determine the performance of five NDT techniques, more than 300 data points are considered for each test. The experimental research shows that utilizing multiple techniques on a single structure to evaluate the defects, significantly lowers error and increases accuracy compared to that from a standalone test. To visualize the NDT data, two-dimensional NDT data maps are developed. This work presents an innovative method to interpret NDT data correctly as it compares the individual data points of slabs with no defects to slabs with simulated damage. For the refinement of NDT data, significance factor and logical sequential determination factor are proposed.

Table of Contents

List of Tables

List of Figures

Acknowledgments

First and foremost, I would like to express my sincere gratitude to my dear supervisor and a true mentor Dr. Rishi Gupta for his consistent and invaluable support, encouragement and mentorship during my studies at the University of Victoria. I would also like to thank my supervisory committee members; Dr. Caterina Valeo and Dr. Min Sun, for their invaluable advice during my research work.

I am very thankful to Canada-India Research Centre of Excellence (IC-IMPACTS), Mitacs Inc., Department of Civil Engineering and Graduate Studies at the University of Victoria for their financial assistance.

I acknowledge the support received by Butler Brothers, Department of Science and Technology-India, Southern Indian Railways, SureSpan Structures, BC Ministry of Transportation and Infrastructure, and Ministry of Forests, Lands, Natural Resource Operations & Rural Development.

I would like to extend my appreciation to Dr. Armando Tura (Laboratory Supervisor), Matthew Walker (Technical Support), Co-op students; Mitch Anderson, and Adrian Hou and Mitacs Exchange Student; Diego Plata Frescas for their assistance during my experimental work.

My sincere thanks to Jerome Etwaroo (Associate Director, Coast Capital Savings Innovation Centre), Tyler West (Program Coordinator, Coast Capital Savings Innovation Centre), and Michael Shannon (Executive in Residence, Coast Capital Savings Innovation Centre) for helping me stay focused during my doctoral studies.

Last but not the least, I would like to thank my parents, my partner Miaoxin Cui, and my friends and colleagues; Kalpesh Prajapati, Kishan Patel, Nirav Bhatt, Boyu Wang, Sean Blaney, Adham Elnewihy, Dr. Mohit Garg, and Pejman Azarsa for their constant motivation and support.

Dedication

To my beloved parents

Chapter 1: Introduction

This chapter highlights the background and motivation, summary of non-destructive testing techniques, contribution to the existing knowledge, research objectives, dissertation organization, and statement of contribution.

1.1 Background and Motivation

The concept of civil Structural Health Monitoring (SHM) is not new, and dates back more than 20 years. This concept has become very popular recently as it has the potential to address the global aging infrastructure problem. Some of the recent catastrophic structural failures (Morandi Bridge in Italy, the newly constructed Pedestrian bridge at Florida International University in Miami, and Metro Bridge in Mumbai) have reminded us about the possibilities of engineering design flaws, construction errors, and extreme weather conditions. 33% of the Canadian municipal infrastructures are either in fair or below fair condition. The current deficit of replacing fair and poor municipal bridges (covers 26% of bridges) is 13 billion dollars (Halsall, 2016). The entire American infrastructure have been given a D+ condition rating with some of the structural elements posing significant risk (and ASCE, 2013). The D+ rating suggests that the infrastructure is in poor to fair condition and mostly below standard, with many elements approaching the end of their service life. A large portion of the system exhibits significant deterioration. Condition and capacity are of serious concern with strong risk of failure. In the U.S., on average there are 188 million trips taken across a structurally deficient bridge every day (ASCE, 2013). In the U.S., almost 4 in 10 bridges are 50 years or older. In the past 10 years, there have been 10 of the deadliest bridge collapses world-wide causing a total of more than 200 deaths and more than 400 injuries. This possesses a strong need for periodic monitoring of at least some important and critical structures if not all.

SHM refers to periodic assessment of the "condition" of the materials, the different elements, and the full assembly of these elements constituting the structure as a whole. SHM as a whole consists of a number of components including Non-Destructive Testing (NDT) (Balageas et al., 2010). A number of NDT techniques can be converted into integrated sensors for real-time SHM. Figure 1 shows the basic components of SHM. This figure illustrates how these components are interconnected with each other. For example, the use of sensors/actuators can determine not only the condition of the material but the structure as a whole. The integrated sensors such as accelerometers, tilt-meters, and displacement gauges provide the information on the vibrational behaviour of structures. Other sensors such as strain, temperature, and humidity measurement provide the information on the structural steel and concrete quality. All of these sensors provide real time data on the material locally and the structure as a whole. The non-integrated sensors such as ultrasonic pulse velocity measurement, ground penetrating radar, half-cell measurement and UAV mountable sensors such as optical cameras, infrared cameras, and impact hammers can determine the condition of the material at one point in time. To analyse the sensors' data, it requires computation using smart software and signal processing techniques. As illustrated in Figure 1, all of these components interact with each other to complete SHM. There are advantages and disadvantages of the different type of sensors. For instance, sensors that are integrated with the structures can provide real time information about the material degradation. However, it is very difficult to maintain these

sensors and they require a significantly higher computational power to analyse their data due to the size of the data. On the other hand, non-integrated and UAV mountable sensors can provide valuable information at a one point in time in a cost-effective way.

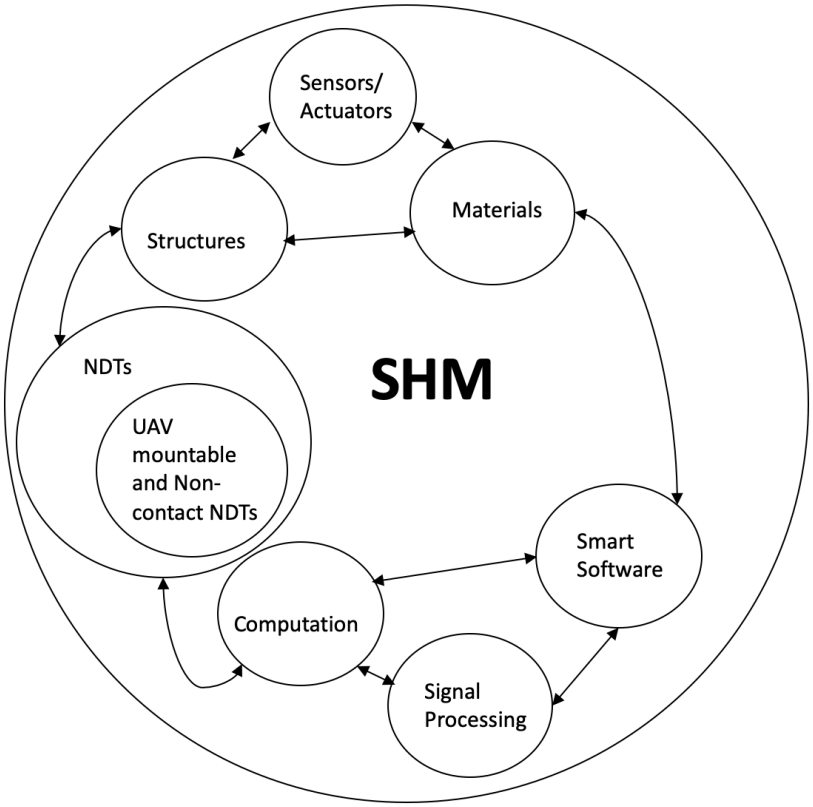

Figure 1: The Basic Components of SHM (Modified from (Balageas et al., 2010))

This study focuses on damage detection and quantification in bridges as these are one of the most important elements of any transportation network. There is a strong need for continuous monitoring and maintenance to check the safety and serviceability of bridge structures. The maintenance of bridges is of prime importance as it provides connectivity links for industrial and domestic movement of vehicles every day. Apart from personal mobility, the bridges support commerce and economic vitality.

Visual inspection is a commonly used technique to detect and identify surface defects in bridge structures as it has been considered the most feasible method for decades. However, there are several challenges with the current methodology. Current methodology (visual inspection) is inadequate and not reliable as it is highly dependent on subjective human judgment. The labor-intensive approach for inspection requires huge investment in terms of an arrangement of temporary scaffoldings/permanent platforms, ladders, snooper trucks, and sometimes even helicopters. This approach involves traffic closure and is time-consuming, managerial intensive, and even dangerous. Due to this inspection method, infrastructure owners pay a very high price and spend hours inspecting structures. There is a strong need for an improved methodology that is faster and data driven to avoid subjective human judgement.

Most common defects in Reinforced Concrete (RC) bridge decks are voids, spalling, corrosion of reinforcement, leaching, scaling, cracking, honeycombing and delamination. Different NDT techniques have been adopted to identify different defects and its severity in the bridge elements. Previous research work indicates that no particular technique is complete, and each has its own advantages and limitations (Conde et al., 2017 and Breysse et al., 2012). There are problems like measuring errors, uncertainty and noise in relation to the different sensors and measuring techniques (Wenzel, 2008), and lack of knowledge about the integration of the data from the point in time of NDT technique and from continuous monitoring in the assessment of the condition rate that needs to be addressed. In addition, most of the previous research work was limited to the development of structural damage models (Huth et al., 2005; Hanif et al., 2018). There exists a need for the material damage model and development of SHM protocols using the minimum number of NDT techniques that give reliable data and the combination of these techniques for damage detection in RC bridges.

1.2 Non-Destructive Testing Techniques

American Concrete Institute (ACI) committee report 228.2R (ACI 228.2R, 2013) lists twenty different NDT techniques for concrete structures. A summary of these techniques is given in Table 1. Out of these twenty different techniques, seven techniques are used in this dissertation work due to non-availability of other techniques. Note that these seven techniques are most commonly used techniques in the field. Table 1 also includes the limitations or advantages of all twenty techniques for their potential use in the field. Description of the techniques used in this dissertation work is expanded further in subsequent chapters.

Table 1: List of NDT techniques

Method and Principle	**Adoption in the dissertation work**	**Remarks**
Visual Inspection – Observe, classify and document the appearance of distress on exposed surfaces of the structure	✓	Modified version is used in this dissertation due to limitations of the current method
Ultrasonic Pulse Velocity (UPV) – Measure the travel time of a pulse of ultrasonic waves over a known path length to determine the relative condition of concrete	✓	Easy to use and widely used in the field. Cost effective way to determine the quality of concrete and also used to detect delamination and voids
Ultrasonic-echo- Transducer emits short pulses of ultrasonic waves which is reflected by opposite side of member or an internal defect; arrival of reflected pulse is recorded by an adjacent receiver, and round-trip travel time is determined	X	Primarily a research tool

Table 1: List of NDT techniques (Continued)

Method and Principle	**Adoption in the dissertation work**	**Remarks**
Impact-echo – Receiver adjacent to impact point monitors arrival of stress waves as they undergo multiple reflections between surface and opposite side of plate-like member or from internal defects	✓	Modified method is used in this dissertation due to limitations of the current method
Spectral analysis of surface waves- Impact is used to generate a surface wave and two receivers monitor the surface motion; signal analysis allows determination of wave speed as a function of wavelength; inversion process determines elastic constants of layers	X	Alternate method is used
Sonic-echo – Hammer impact on surface and a receiver monitors reflected stress wave. Time-domain analysis used to determine travel time	X	Used for deep foundations (Piles and piers)
Impulse-response – Test is similar to sonic-echo method except that signal processing involves frequency-domain analysis of the received signal and the impact force history	X	Used for deep foundations (Piles and piers)
Impedance logging – Test is similar to sonic-echo or impulse-response, but the use of more complex signal analyses (time and frequency domain) analysis of the received signal and the impact force history	X	Determine the approximate 2-dimentional shape of the deep foundation
Crosshole sonic logging – Analogous to the ultrasonic pulse velocity test, but transducers are positioned within tubes cast into the deep foundation or holes drilled after construction	X	Alternative method- UPV is used
Parallel Seismic- Receiver is placed in hole adjacent to the foundation. Foundation is struck with a hammer and signal from receiver is recorded. Test is repeated with receiver at increasing depth	X	Determine the foundation depth and determine whether it is of uniform quality

Table 1: List of NDT techniques (Continued)

Method and Principle	Adoption in the dissertation work	Remarks
Direct Transmission Radiometry- Measure the intensity of high energy electromagnetic radiation after passing through concrete	X	Determine in-place density of fresh or hardened concrete
Backscatter radiometry- Measure the intensity of high-energy electromagnetic radiation that is backscattered (reflected) by the near surface region of a concrete member	X	Determine in-place density of fresh or hardened concrete
Radiography- The intensity of high energy electromagnetic radiation which passes through a member is recorded on photographic film	X	Locate reinforcing and prestressing steel, conduits, pipes, voids, and honeycombing. Alternative methods are used due to the high cost of Radiography
Gamma-gamma logging- see direct transmission and backscatter radiometry	X	Locate regions of low density along length of foundation
Cover meter- A low frequency alternating magnetic field is applied on the surface of the structure; the presence of the embedded reinforcement alters this field, and measurement of this change provides information on the reinforcement	✓	Locate embedded steel reinforcement, measure depth of cover, and estimate diameter of reinforcement. Easy to use and cost-effective
Half-Cell Potential – Measure the potential difference (voltage) between the steel reinforcement and a standard reference electrode; the measured voltage provides an indication of the likelihood that corrosion is occurring in the reinforcement	✓	Identify region or regions in a reinforced concrete structure where there is a high probability that corrosion is occurring at the time of the measurement. Easy to use and cost-effective
Polarization methods- Measure the current required to change by a fixed amount the potential difference between the reinforcement and a standard reference electrode; the measured current and voltage allow determination of the polarization resistance, which is related to the rate of corrosion	X	Complex method. Rarely used in the field

Table 1: List of NDT techniques (Continued)

Method and Principle	Adoption in the dissertation work	Remarks
Penetrability methods- Measure the flow of a fluid (air or water) into concrete under prescribed test conditions; the flow rate depends on the penetrability characteristics of the concrete	X	Primary a research tool
Infrared Thermography- The presence of flaws within the concrete affects the heat conduction properties of the concrete and the presence of defects are indicated by differences in surface temperatures when test object is exposed to correct ambient conditions	✓	Locates delamination in pavements and bridge decks. Non-contact nature of this method makes it very useful in the field application
Ground Penetrating Radar (GPR)- Analogous to the ultrasonic-echo methods except that electromagnetic waves are used instead of stress waves. Interface between materials with different dielectric properties results in reflection of a portion of incident electromagnetic pulse	✓	Higher accuracy and feasible to use it in the field

1.3 Contribution to the Existing Knowledge

This research work contributes to the following areas of condition assessment, monitoring, and management of bridge structures.

1. Visual Inspection

Three new methodologies have been developed to replace/improve the existing visual inspection technique. The first methodology uses a fuzzy logic-based decision-making tool along with the image processing algorithm. The developed image processing software is used with the fuzzy set framework to calculate the damage indices for various deterioration mechanisms like corrosion, alkali-aggregate reaction, freeze-thaw attack, sulfate attack, acid attack/loading, fatigue, shrinkage, and honeycombing. This will reduce the errors associated with the subjective human judgment. In the second methodology, to expedite the condition assessment procedure, a UAV-assisted AASHTO guideline-based (AASHTO, 2011) condition rating system is developed. It utilizes a combination of a UAV system, an image processing tool, and a bridge element inspection guideline published by AASHTO to inspect long span railway bridges. It also highlights the differences between two different inspection methods; the damage computed solely by conducting a traditional on-site visual inspection, and the damage calculated using image processing tool integrated with the AASHTO guide manual. In the third newly invented patent-pending method, a combination of multiple sensors is proposed to be integrated into a UAV system. These sensors include two optical cameras, an infrared camera, an acoustic assembly, and two

laser sensors. The sensors are integrated into such that the data collected could be overlaid to detect and quantify damage more accurately and reliably.

2. UAV-based subsurface damage detection

A patent-pending UAV-based acoustic method was developed to detect subsurface voids and delamination. It is a novel inspection apparatus that comprises of a UAV and an acoustic signal generator coupled to the UAV. The acoustic signal generator includes a hammer having a contact surface situated with respect to the UAV to be movable by the UAV to produce an acoustic signal in a structure. An acoustic detector is coupled to the UAV and situated to receive acoustic signals from the structure in response to the acoustic signal produced in the structure. Using signal processing techniques, field inspectors will be able to detect and even quantify voids and delamination in concrete structures.

3. Refinement of NDT data based on the significance of the defects

This particular research contributes to the knowledge of the performance of NDT techniques in terms of their errors when applied to the RC slabs. An outcome of this innovative research was the development of a model to refine multiple commercially available NDT techniques' data to detect and quantify subsurface defects. To determine the performance of each NDT technique, more than 300 data points were considered. The experimental research shows that utilizing multiple techniques on a single structure to evaluate the defects, significantly lowers error and increases accuracy compared to that from a standalone test.

4. Interpretation of NDT data

To visualize and interpret the NDT data, two-dimensional NDT data maps are developed. This work is a foundation and is an innovative method to interpret NDT data correctly as it compares the individual data points of slabs with no defects and the slabs with simulated damage. These data maps will help researchers to develop similar experiments with different simulated damage to determine NDT techniques' capability in detecting and quantifying subsurface damage.

5. Determination of Rebar characteristics

There are a number of bridge decks that are old and without structural drawings. The research conducted as a part of this study contributes to the existing knowledge of identifying the rebar information such as rebar diameter, spacing, and cover depth. This research demonstrates the applicability of the Profoscope and GPR to determine rebar information. To achieve this, an accuracy model of GPR and Cover meter is developed. This model will be very valuable to the infrastructure owners (e.g., Ministry of Forest (MFLNRO) in making necessary decisions for managing their structures. It also highlights the key challenges faced during the deployment of both the NDT techniques.

1.4 Research Objectives

The objectives of this dissertation work are succinctly summarized below.

1. Develop image processing algorithms to detect and quantify surface defects in concrete structures.

2. Develop a damage assessment software tool to assign condition assessment rating for civil structures.

3. Determine the performance of commercially available NDT techniques in detecting and quantifying subsurface defects using a new NDT data refinement model.

4. Integration of a UAV system into a visual inspection-based guideline to detect and quantify condition of surface defects.

5. Development of a multi-device robotics-based sensor data acquisition system for mapping and assessing defects in civil structures.

6. Development of UAV-based acoustic technique for mapping subsurface defects in civil structures.

1.5 Dissertation Organization and Statement of Contribution

Some of the research work presented in this doctoral dissertation is a part of an international research collaboration, led by Professor Rishi Gupta at the University of Victoria, Victoria BC, Canada. This research was funded by the Canada-India Research Centre of Excellence (IC-IMPACTS) based out of University of British Columbia and the Department of Science and Technology (DST), India. This dissertation includes a total of 5 chapters. Chapter 1 is an introductory chapter. Chapter 2 and 3 focuses on the detection and quantification of surface and subsurface defects respectively. Chapter 4 includes the integration of UAV-based techniques and images processing algorithms into the existing bridge element inspection guideline. In addition it also includes the two novel UAV-based NDT techniques. Chapter 5 concludes the work carried out in this dissertation. Following is the organization of individual chapters and statement of contribution.

Chapter 2 describes the use of fuzzy logic as a decision-making tool integrated with image processing algorithms to evaluate the condition of infrastructure. This innovative technique has the potential to expedite the inspection process and improve the current visual inspection technique. This work (Pragalath et al., 2018) was published in the ASCE Journal of Performance of Constructed Facilities. I contributed towards the development of the image processing algorithm along with the other researcher Seshathiri, S. My contribution also includes identification of the type of damage, modelling of damage rating framework, and assignment of damage rating. The idea of implementation of Fuzzy logic system along with the image processing was conceived by Pragalath, H., Gupta, R., and Esakki, B.

Chapter 3 outlines the development of a model to refine multiple commercially available NDT techniques' data to detect and quantify subsurface defects. To achieve this, a total of nine 1800 mm × 460 mm reinforced concrete slabs with varying thicknesses of 100 mm, 150 mm and 200 mm were prepared. These slabs were designed to have artificially simulated defects like voids, debonding, honeycombing, and corrosion. To determine the performance of each NDT technique, more than 300 data points were collected. The content presented in this chapter is my original work. This work (Rathod et al., 2019a) was published in the Journal of Construction and Building Materials, Elsevier. Under the supervision of Gupta, R., I was responsible for the entire work starting from the ideation stage to the final modelling and implementation stage. Dr. Gupta contributed to the manuscript. The NDT data maps that are an integral part of chapter 3 are included after the article. These data maps were solely developed by me. The data maps were peer-reviewed and published in the open access Data in Brief Journal (Rathod et al., 2019b). At the end

of Chapter 3, application of GPR and a rebar detector is elaborated to obtain rebar information of existing concrete structures. This work includes the use of two techniques; GPR and Cover meter (Profoscope) to determine rebar spacing, cover depth, and diameter. This work (Rathod et al., 2019c) was published in the Journal of Case Studies in Construction Materials (Open access). Debeck, S. helped me collect the experimental data and helped me with some of the modeling work to represent the data. The experimental idea was conceived by me and is my original work performed under the supervision of Gupta, R.

Chapter 4 focuses on the advancement of AASHTO-based condition assessment guideline by the use of a UAV system and image processing to quantify surface defects. This work (Rathod et al., 2019d) was submitted in the journal Infrastructures. Ranagasamy, M. helped me collect the data using the aircraft. He also helped me pre-process the images using the Adobe- Photoshop Software. In addition to this, Esakki, B. assisted me in editing the chapter (manuscript) under the guidance of Gupta, R. Other than this, the experimental idea was conceived by me. A new methodology (IPA = AASHTO-based image processing) that utilizes a combination of a UAV system, an image processing tool, and a bridge element inspection guideline published by AASHTO to inspect a long span railway bridge was developed by me. At the end of Chapter 4, two patent pending UAV-based techniques (Rathod et al., 2019e; Rathod et al., 2019f) to detect and quantify damage have been included. Both the techniques were co-invented by me and Gupta, R. at the University of Victoria. The work related to both the techniques has been submitted to the United States Patent Office. Please note that Klarquist Sparkman, LLP (Intellectual property law firm) and UVIC Industry Partnerships have assisted me in writing some of the legal content of these two novel techniques.

Chapter 5 presents the scope of future work and concluding remarks of this dissertation study written by me.

All the related references are combined and presented at the end of this dissertation.

Publications

A list of publications submitted/published during this doctoral study that have formed a part of this dissertation is given below.

Journal Papers

Published

1. Pragalath, H., Seshathiri, S., Rathod, H., Gupta, R., and Esakki, B., 2018, "Deterioration Assessment of Infrastructure Using Fuzzy Logic and Image Processing Algorithm", *Journal of Performance of Constructed Facilities,* vol. 32, no. 2, pp. 4018009. https://doi.org/10.1061/(ASCE)CF.1943-5509.0001151
2. Rathod, H. & Gupta, R. 2019a, "Subsurface simulated damage detection using Non-Destructive Testing Techniques in reinforced-concrete slabs", Construction and Building Materials, vol. 215, pp. 754-764. https://doi.org/10.1016/j.conbuildmat.2019.04.223
3. Rathod, H. & Gupta, R. 2019b, “Two-Dimensional Non-Destructive Testing data maps for Reinforced Concrete slabs with simulated damage”, Data in Brief Article, Volume 25, 104127, ISSN 2352-3409 (Open Access) https://doi.org/10.1016/j.dib.2019.104127

4. Rathod, H., Debeck, S., Gupta, R. & Chow, B. 2019c, "Applicability of GPR and a rebar detector to obtain rebar information of existing concrete structures", Case Studies in Construction Materials (Open access), vol. 11, pp. e00240. https://doi.org/10.1016/j.cscm.2019.e00240

Submitted/In-Review

1. Rathod, H., Gupta, R., Rangasamy, M., and Esakki, B., 2019d, "UAV-assisted Condition Assessment of Long Span Railway Bridges", Infrastructures. (Submitted) (June 10th, 2019).

Conference Proceedings (not included in this dissertation)

1. Gupta, R., and Rathod, H., 2018, "Non-contact NDT techniques for Structural Health Monitoring", 3rd R.N. Raikar Memorial International Conference and Gettu-Kodur International Symposium on Advances in Science and Technology of Concrete, 14-15 December, Mumbai, India.
2. Rathod, H., Gupta, R., Esakki, B., and Blaney, S., 2017, "Non-Contact Non-Destructive Infrared Thermography-based Evaluation of Reinforced Concrete Structures" 6th international conference on Engineering Mechanics and Materials, CSCE 31st May-June 3, Vancouver, Canada.
3. Rathod, H., Gupta, R., Kaya, Y., and Esakki, B., 2018, "Condition Assessment of Bridges using Non-Contact Vibration Measure-A Pilot Study" 1st International Conference on New Horizons in Green Civil Engineering (NHICE-01), Victoria, BC, Canada, April 25 – 27.

Patents

1. Rathod, H., Gupta, R., 2019e "Multi-device Robotics-based Sensor Data Acquisition System for Mapping and Assessing Defects in Infrastructure", USPTO Provisional Patent, Application No. 62828781; Klarquist Ref. No. 2847-102346-01 (Submission Date- April 15th, 2019) (Licensed to HRG Infrastructure Monitoring Inc.).
2. Rathod, H., Gupta, R., 2019f "UAV-based Acoustic Technique for Mapping Defects in Civil Infrastructure", Patent Filed under Patent Cooperation Treaty - Ref. No. GUPRI-T3147; Klarquist Ref. No. 2847-100745-01 (Submission Date- May 1, 2019) (Licensed to HRG Infrastructure Monitoring Inc.).

Chapter 2: Deterioration Assessment of Infrastructure Using Fuzzy Logic and Image Processing Algorithm

Article Link : https://doi.org/10.1061/(ASCE)CF.1943-5509.0001151

Haran Pragalath[1], Sankarasrinivasan Seshathiri[2], Harsh Rathod[3], Balasubramanian Esakki[4], and Rishi Gupta[5]

[1]Post Doctorate Researcher, Department of Civil Engineering, Vel Tech University, Chennai, Tamilnadu, India. email: haran5441@gmail.com

[2]Research Associate, Centre for Autonomous System Research, Vel Tech University, Chennai, Tamilnadu, India. email: sankarsrin@gmail.com

[3]PhD Scholar, Department of Civil Engineering, University of Victoria, Victoria BC, Canada. email: hmrathod@uvic.ca (Corresponding Author)

[4]Associate Professor, Centre for Autonomous System Research, Vel Tech University, Chennai, Tamilnadu, India. email: esak.bala@gmail.com

[5]Associate Professor, Department of Civil Engineering, University of Victoria, Victoria BC, Canada. email: guptar@uvic.ca

Note: This chapter is adapted in part from published work (Pragalath et al., 2018) in ASCE Journal of Performance of Constructed Facilities, with permission where appropriate. This chapter highlights the development of a novel damage assessment tool to improve/replace existing visual inspection method for detecting and quantifying surface defects in civil structures. The tool uses fuzzy logic-based decision making and image processing algorithms to assign a condition assessment rating in civil structures.

2.1 Abstract

Safety and serviceability of civil infrastructure have to be ensured either as part of a periodic inspection program or immediately following a given hazardous event. Use of digital imaging techniques to identify the deformed or deteriorated surfaces of the structure is a substantial area of research and aims to investigate several unknown parameters, including damage quantification and condition rating. This manuscript illustrates the integration of previously developed fuzzy logic-based decision-making tool with the currently developed image processing algorithm to quantify the damage for the condition rating of civil infrastructures. The proposed integrated framework exploits visual specifics of different elements of infrastructure to perform an automated evaluation of structural anomalies such as cracks and surface degradation. Two different image segmentation tools a) Bottom Hat Transform and b) Hue, Saturation, Color (HSV) thresholding are applied to identify the surface defects. The developed image processing software is used with the fuzzy set framework proposed in the previous research to gauge the damage indices due to various deterioration like corrosion, alkali-aggregate reaction, freeze-thaw attack, sulfate attack, acid attack/loading, fatigue, shrinkage, and honeycombing. Case studies of a long span bridge and a warehouse building are illustrated for concept validation. The refined comprehensive method is premeditated as a Graphical User Interface (GUI) to ease the real-time condition assessment of civil infrastructures.

2.2 Introduction

Civil Structural Health Monitoring (SHM) has become an important requisite for diagnosis of the material condition and structural integrity as a whole to ensure the safety of critical civil infrastructures (Chang et al. 2003). It involves the condition assessment of civil infrastructures such as bridges, heritage structures, dams, power plants, pipelines, and other offshore structures. SHM is an efficient tool which can provide early warnings not only to safeguard the structure but also for the safety of end users. SHM can serve as an important tool to facilitate periodic infrastructure inspections. In many parts of the world, civil infrastructure is under tremendous strain due to increased traffic loads, shortened construction time, and lack of resources for inspection, maintenance, and repair of structures. Moreover, an inspection of civil infrastructure after a natural calamity, hurricanes, tornados, and fire can also greatly benefit from innovative SHM techniques. The sudden collapse of structures including bridges can cause a large number of causalities. In these circumstances, SHM can be an invaluable tool to manage and maintain the structural integrity and also guarantee the residual capacity of civil structures. Acquired knowledge on the condition of the structure through SHM paradigm will enable to take preventive measures to avoid catastrophic failures, leading to prolonged service life and ultimately reduce life cycle cost. The structural evaluation in terms of strength, serviceability, and durability offer awareness to the user and public for maintenance, repair, rehabilitation, and decommissioning. The accumulated information can be maintained in a database which can help us to formulate design guidelines for effective condition monitoring. One of the components of SHM is continuous monitoring using sensors and their related smart software (Dong et al. 2003). The present study describes the development of a graphical tool inculcating a fuzzy system and image processing module for appropriate estimation of structural damage condition index (SCI). The collected information can be used as a database to formulate the design guidelines for effective condition monitoring.

Initial sections of this paper describe the use of fuzzy logic developed by Jain and Bhattacharjee (2012a, 2012b) for decision making and later to assess the damage indices for various structural defects such as corrosion, alkali-aggregate reaction, sulfate attack, acid attack, fatigue, shrinkage, and honeycombing. A list of other deterioration mechanisms (along with their possible causes) not covered by this model can be found in the PCA guidelines (Portland Cement Association, 2002). It should be noted that more detailed findings presented in this paper are a result of integrating image algorithms with the fuzzy logic-based decision-making protocol which can be used to expedite the overall SHM process through automatic detection of multiple defects such as cracks, efflorescence and other surface degradation as shown in Figure 2.

Recent trends in digital acquisition and image analysis are becoming a crucial factor in nondestructive testing of civil structures (Yao and Pakzad 2012; Jahanshahi and Masri 2012). The novel digital protocols can bring fundamental advances over conventional strategies and can expedite the overall inspection activity significantly (Sankarasrinivasan et al. 2015; Jahanshahi et al. 2009). Such innovative protocols provide essential support for proficient monitoring and diagnosis activities. To establish such automated systems, the developments of sophisticated image processing tools are of foremost requisite in assessing critical infrastructural defects. The authors believe that the developed software module can facilitate image-oriented or image-assisted evaluation and corresponding structural damage

assessment with reduced uncertainty brought in by human judgment. The main objective of this manuscript is to demonstrate the development and application of this image-based software module for inspection of the civil infrastructure.

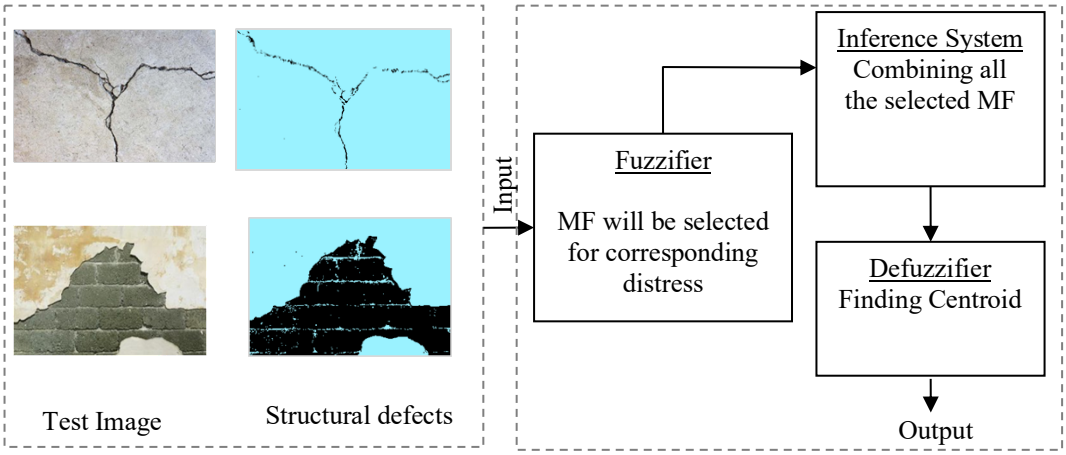

Figure 2: Integration of image processing tool with the fuzzy logic framework for decision making: a) image analysis; b) fuzzy concept

2.3 Fuzzy Approach for Condition Assessment of Structures

The fuzzy logic framework is an artificial intelligence technique to provide solutions to solve complex problems using linguistic terms (Mamdani and Assilian, 1975). It involves the development of Membership Functions (MFs), fuzzy logic actions, and defuzzification. The MFs are used to characterize the fuzzy set based on whether the selected elements are discrete or continuous in representing graphical form with an essence of fuzziness. MFs are classified into triangular, Gaussian, trapezoidal and Z shape. In general, triangular MFs are widely used because of its simplicity in constructing fuzzy sets (Zhao, J., and Bose, B. K, 2002). After selecting appropriate MFs, the relationship between input and output parameters is formulated by a set of linguistic statements called as fuzzy rules, and normally IF-THEN rules are adopted. The number of fuzzy rules corresponds to the number of fuzzy sets for each input variable. The evaluation of conditional statements occurs in parallel to tune the system randomly. Assessed fuzzy rules are used to provide an output for any input within the range of the fuzzy processes. However, an output of fuzzy inference needs to be a scalar quantity to determine the performance characteristics of the considered system. For which, defuzzification is carried out to convert the fuzzy values into a required output wherein a fuzzy quantity is transformed into a precise quantity.

Few researchers have employed Fuzzy Set Theory (FST) for the evaluation of deterioration of civil structures. Blockley (1975, 1977) used FST to deal with structures failing due to causes other than the stochastic variations in loads and strengths. Brownand Yao (1983), Wang and Elhag (2007) used FST as a decision-making tool for the damage assessment of a structure and subsequent repairs. Similarly, researchers have dealt with similar topics such as: structural damage assessment (Ogawaet et al. 1984; Souflis and Grivas 1986; Savage et al. 1988; Hathout 1993; Furuta et. al.2000; Liang et al. 2001), performance evaluation (Hadipriono 1988), expert system for damage assessment (Ross et

al. 1990), and condition assessment ratings (Arliansyah et al.2003; Sasmal et al.2006; Sasmal and Ramanjaneyulu 2008). Fwa et al. (2003) proposed a condition rating and maintenance need assessment system for airport pavement using fuzzy logic systems, which related distress condition directly to maintenance needs. Kim et al. (2006) reported FST-based assessment system for Reinforced Concrete (RC) building structures to estimate the current state of buildings and to provide guidelines for future maintenance and management.

Visual inspection of any deteriorating structure is an integral aspect of routine assessment practices. Data collected through visual inspection is primarily qualitative and subjective because it rarely involves precise measurements and depends heavily on the expertise of the site-inspection team. To deal with these concerns, Jain and Bhattacharjee (2012a, 2012b) proposed a methodology using fuzzy concepts for visual inspection-based condition assessment. They developed a tool using Visual Basic application that can be accessed in Microsoft Excel. The present study utilizes this framework of Fuzzy Logic (FL) to obtain Structural Condition Index (SCI) of civil infrastructure and its working principle is outlined further.

In the context of condition assessment, the fuzzy logic formulation is carried out initially by selecting MFs and the parameters to define these MFs are based on the user inputs as per the condition rating of structural elements. These MFs are further processed to account for the severity of deterioration either occurring as local or global in a structural element by using linguistic hedges/modifiers. However, elements of any structure have many distresses and hence each has to be assigned appropriate MFs. The accumulation of MFs is obtained using the fuzzy weighted average technique. These combined MFs are evaluated using a set of Fuzzy rules normally, "If-Then" rules which are used further for assessing the condition of the structure. In the present study, various codes are assigned for different distresses, and its severity levels and they have been utilized to determine the damage condition of an element. The conclusions drawn from these fuzzy rules are made available as crisp output to the user in the defuzzification process using the centroid method.

To prepare these MFs, a series of questionnaires were prepared related to commonly occurring distress manifestation (such as Corrosion, Delamination, Poor workmanship and Acid attack) and distributed among professionals (experts) from the field of construction engineering. This work was carried out by Jain and Bhattacharjee. This rating varies from 0 to 5 where '0' represents a condition that doesn't require any repair, and '5' represents critical conditions that require immediate action (Jain and Bhattacharjee, 2012a). This study reported questionnaire responses from 26 practicing senior experts/consultants, 3 scientists, 22 academicians, and 15 international experts. However, the responses from individual experts seem to differ due to varied perceptions to predict the distress rates of the structure. Hence, these observations need to be incorporated in a systematic way through developing membership functions in FST.

In the present study, various response data from individual experts are captured by following multiple steps to develop MFs. The collected response data are appropriately assigned a condition rating and evaluated further. Initially, if the intermediate condition rating is smaller than predecessor and successor, then, the average of these ratings is considered as an intermediate rating. For example, R_0, R_1, R_2, R_3, R_4, and R_5 are obtained as condition ratings, in which, R_4 is lower than both R_3 and R_5, then R_4 is revised as the

average of R_3 and R_5. In order to apply the Fuzzy Set Theory, the condition rating values should be in increasing order. For example, R0, R1, R2, R3, R4, and R5 are obtained as condition ratings, in which, R4 is lower than both R3 and R5, then R4 is revised as the average of R3 and R5. Different condition ratings (R0 to R5) on the same structure are given based on the repair priority of the structure at once (no replicated inspections) as suggested in the literature by Mitra et al. (2010). In simple terms, experts could have different opinions on the same defects present on the structure or structural element. For example, a structure/a structural element could be given any rating (R0 to R5) by an expert for the same deterioration mechanism or distress. Secondly, in order to neglect the small contribution of expert opinion in an evaluation of distress levels where the condition rating of an individual is less than the specific percentage of summation of total respondents, then the same is updated to zero. A typical scenario where R_0 is less than a certain percentage (assume 10%) of summation of R_0, R_1, R_2, R_3, R_4, and R_5, then, R_0 is updated to zero. Further, arrived condition ratings are normalized with respect to the peak number of responses. Later, the evaluated fractional values are considered as degrees of MFs (μ) corresponding to its condition ratings. The obtained MFs are modified using linguistic hedges/modifiers (Mitra et al. 2010) to account for a local and global level of defects, which are given by,

$$\begin{aligned} Local:\ & \mu_{x_i},local = \mu_{x_i}^{1/2} \quad for\ \ x_i \le x_0 \\ & \mu_{x_i},local = \mu_{x_i}^{2} \quad for\ \ x_i \ge x_0 \end{aligned} \tag{2.1}$$

$$\begin{aligned} Global:\ & \mu_{x_i},global = \mu_{x_i}^{2} \quad for\ \ x_i \le x_0 \\ & \mu_{x_i},global = \mu_{x_i}^{1/2} \quad for\ \ x_i \ge x_0 \end{aligned} \tag{2.2}$$

Where, x_i = condition rating (0–5) and x_0 = condition rating where MF is maximum

The exponential terms, μ_x^2 involving square of the MF values reduce the magnitude of MF value at x. In contrast, $\mu_x^{1/2}$ increases the same. The use of modifiers ensures that if a certain severity of distress occurs "locally," then distress would warrant less repair action and "global" warrant higher repair action (Jain et al. 2012 and Mitra et al. 2010).

The terms "Local" and "Global" are used in determining the extent of each distresses and have been accounted for by means of limits in the definition of membership functions. For example, the local extent will be considered if an element under study has <=15% damage. Global will be considered if the damage is present all over the area under study. The philosophy behind this is given in the literature by Mitra et al. (2010).

So far, MFs have been developed for various defects individually. However, any structural element can undergo more than one deteriorations and that has to be accounted for evaluating damage condition of civil structures. In view of this, each distress can be assigned with applicable MFs and the generalized fuzzy rule will be formulated. In order to account for the combination of defects, a combined MF has to be developed using the following steps. MFs are initially rescaled using the following relation.

$$x_i^{j'} = \frac{x_i^j}{a - x_i^j} \tag{2.3}$$

Where $x_i^{j'}$ = scaled condition rating for i^{th} MF at j^{th} distress; x^j_i= unscaled condition rating for i^{th} MF at j^{th} distress and a = spread of the universe of discourse ≈5. To avoid any discontinuity, 'a' has been assumed slightly greater than 5.0. (5.0001). As a user, you could select any value slightly greater (Value + 1 x 10^{-3}) than the actual rating. If the actual rating

value is used (in this case 5), then both a and x_i^j being 5 would render x_i^j to be mathematically undefined.

Further, by using the vertex method (Dong and Shah, 1987), the scaled MFs are aggregated to obtain combined MFs as given by,

$\mu_i \mid x_i^{j'}$ for

$$\mu_i \in \{0,0.1,0.2,.....0.9,1.0,1.0,0.9,0.8,.....,0.2,0.1,0\} \tag{2.4}$$

Where, $x_i^{j'} = \sum_j x_i^{j'}$ = aggregation of MF on a modified scale.

Finally, the scaled MFs are reverted to the original scale using Eq. (2.5)

$$x_i^{j'} = \frac{a x_i^j}{1 + x_i^j} \tag{2.5}$$

where x_i = Original scale rating corresponding to MF value μ_i

After formulating the combined distress effects, defuzzification is carried out using the centroid method (Madau and Feldkamp, 1996). The centroid is calculated based on the following formula,

$$Centroid = \sum_{i=1}^{n} \frac{1/6 (x_{i+1} - x_i)(2x_i y_i + x_{i+1} y_i + x_i y_{i+1} + 2x_{i+1} y_{i+1})}{0.5(x_{i+1} - x_i)(y_i + y_{i+1})} \tag{2.6}$$

Where x = Condition rating, y= degree of MFs, i = number of areas which varies from 1 to 'n'

The resulting centroid represents the condition index of an element. Initially, this is performed for all the elements which correspond to an individual deterioration mechanism. Later, using the weighted average method, structural condition indices will be determined. In the weighted average method, each element condition index is assigned with a weightage depending upon the significance of an element. The ratio of summation of weighed condition index to the summation of weights is calculated as SCI to examine the damage condition of the structure.

In order to understand more clearly the distress manifestation conditions along with severity, a code is generated as 'deterioration–distress–severity–extent'. For example, 'CORR-CRACK-MOD-G' represents corrosion as deterioration, cracks as distress, severity at a moderate level and extent as global level as similar to previous work (Jain and Bhattacharjee, 2012b). Similarly, MFs are generated for all the inspection condition codes. Different deterioration mechanisms considered in this study are corrosion, alkali-aggregate reaction, freeze-thaw attack, sulfate attack, acid attack, fatigue, shrinkage, and honeycombing. The detailed procedure for developing MFs is explained further in the Appendix at the end of the manuscript.

2.4 Image Algorithm for Detection and Quantification of Structural Defects

The formation of cracks is an early indication of deterioration, especially in reinforced concrete structures. Cracks can lead to a reduction in the structural integrity of structures or catastrophic failure if not assessed regularly and adequately. The traditional crack monitoring methods are performed by professionals in which, crack patterns have to be located and sketched manually. Such detection methods are laborious, time-consuming and

subjective. In order to accelerate the process, image processing-based crack detection method is suggested in this study and proven to be effective in estimating surface defects.

Jahanshahi et al. (2009) explored the survey of vision-based crack and corrosion detection approaches. Rose et al. (2014) reviewed experimental systems to determine the cracks in the concrete bridges. Ikhlaset al. (2003) compared four crack detection techniques namely Fast Haar Wavelet Transform (FHWT), Fast Fourier Transform (FFT), Sobel and canny edge detectors. Yamaguchiet al. (2008, 2010) considered scalable image processing method to analyze larger images. Prasanna et al. (2012) proposed a histogram-based feature extraction and statistical interference algorithm to identify the cracks. Lattanzi et al. (2014) exploited the intrinsic characteristics of images through segmentation based on Canny and K-means methods. Torok et al. (2014) reconstructed 3D profiles and subsequently measured the geometrical characteristics including cracks of collapsed building structures. Though crack detection algorithms are predominantly successful, the quantification aspect is still challenging and dependent on a lot of practical issues Zou et al. (2012). Limited research outcomes are published comprising morphological filter (Nguyen et al. (2012), scanning electron microscopy Vidal et al. (2016) and depth perception techniques Jahanshahi and Masri (2013)). In contrast to prevailing literature, the proposed methodology incites rapid and computationally inexpensive inspection system that can be operative for both color and grayscale images. The paper also highlights crucial parameters for structural damage forecast such as crack length and surface degradation.

In this successive section, an effective crack detection algorithm is formulated considering both morphological and color features of cracks. The Hough-based filtration is adopted to eliminate unnecessary edges which are not representing cracks. In addition, quantification of the crack is obtained based on vision technique to examine the criticality of the damage of infrastructure. A study has also been conducted to calibrate the developed model. The description of the proposed approach is enumerated below.

Morphological Approach

The morphological filter is widely used for detection of structural patterns, feature analysis, and shape extraction from binary and grayscale images. As concrete cracks possess some distinct pattern, the paper proposes a specific morphological filter for crack detection. In order to examine these characteristics; suitable image filters are to be incorporated. Initially, the test images are converted into greyscale, and bottom hat transform is performed. Then, images are skeletonized, and Hough line filter is applied to remove the unnecessary regions. Finally, erosion and post-processing of filtered images provide the quantification of cracks. The detailed description of each morphological parameter is described below.

Bottom Hat Transform (BHT)

BHT is a morphological filter capable of extracting images' features which are dark toned and satisfies specific structural geometry. The mathematical expression is given by the difference of the image and its closing by a structural element as in Eq. 2.7

$$B\_out = (Img \,.\, s) - Img \tag{2.7}$$

Where '*Img*' and 's' refers to the test image and structural element, respectively. *B_out* is the output binary image. In a structure being studied by the authors, the structural element matrix of 3× 3 size and the output corresponds to pixel elements which are smaller in size.

In general, the size of the structural element has to be calibrated in par with acquisition parameters such as capturing distance and resolution. In order to evaluate the proposed image algorithms, various cracks on the walls are considered which are shown in Figure 3a.

Though the performance of the BHT is satisfactory, the results obtained are often redundant. They provide inaccurate information in real time scenario where thin dark edges resulting from wall curvature, door edges, and other corners of the structure appear as cracks. The simulation results for random test image (Figure 3b) using BHT transform shows both cracks along with other erroneous dark edges/corners. Hence, it needs additional filtration to remove the excessive edges other than cracks.

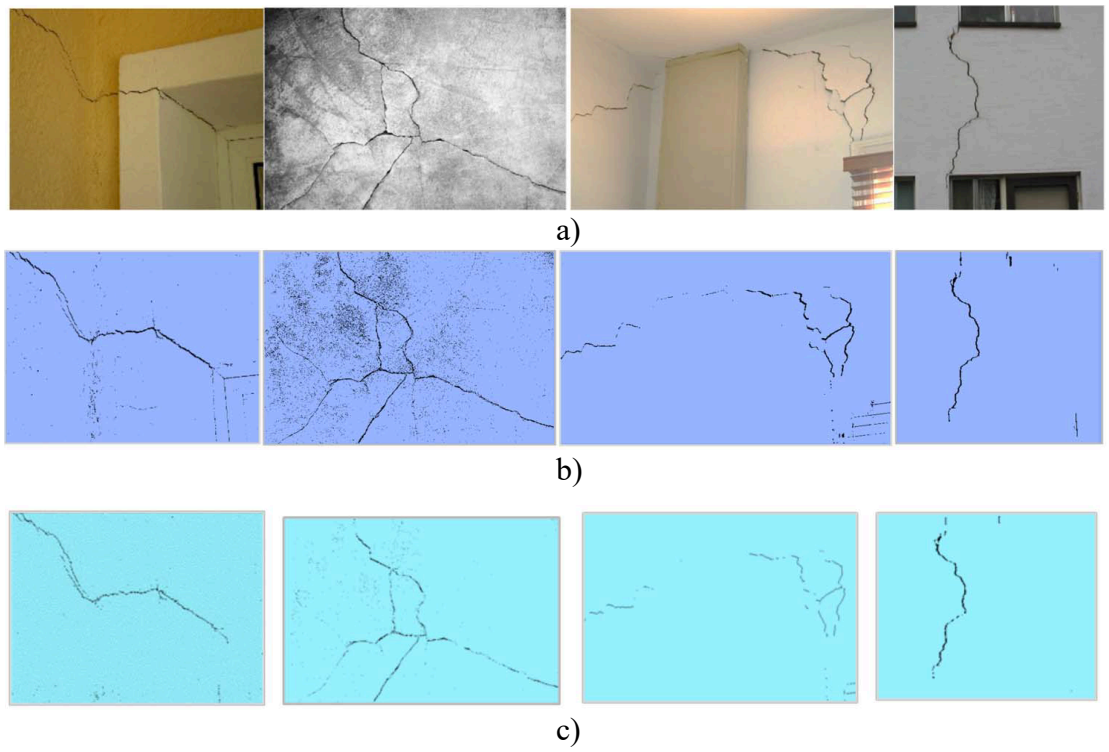

Figure 3: Test images and detection of cracks: (a) various cracks on the walls; (b) BHT transform output; (c) improved crack results

Skeletonization

This process is carried out to convert the detected edges into a single-pixel-wide line. During this process, redundant edge pixels are removed, which assists in appropriate segmentation. As the crack length quantization relies on the unique representation of cracks, this step is foremost important in removing surplus pixels. Once the skeletonizing is done, the Hough transform is applied to remove the perfectly straight edge segments.

Hough Line Elimination Filter

Hough Transform is a mapping of image pixels in spatial (x, y) domain to (r, θ) Hough space. Under such transformation, the presence of collinear points in the spatial domain is represented by a point with a similar angle and distance in Hough space. The problem of classifying dark corners and edges from the detected cracks is critical in crack

quantification. Hence, the paper proposes the application of Hough transform, to identify straight line edges. Further, by setting a proper threshold, the unwanted edges can be nullified in the output image. Hence the straight line edges present in the output image can be eliminated by setting a proper threshold. Figure 3c shows the output after incorporation of Hough filter where it can be clearly seen that all the straight line edges are removed except the cracks.

Erosion and Other Processing

Erosion removes all the insignificant regions which are negligible in relation with detected segments. Especially it is very effective in the removal of isolated points and small regions which cannot be eliminated by Hough and BHT filters (Figure 3c). Further processing comprises removing isolated points and maintaining continuity of the edge pixels.

HSV (Hue, Saturation, Color) Thresholding- Color-based Approach

In this approach, the color information of the test image is manipulated to discriminate crack pixels. The test images are converted from RGB (Red, Green, Blue) color space to hue space for its robustness and accuracy. The HSV images are skeletonized then Hough line filter has been applied to remove the unwanted regions. Further, erosion of images and post-processing resulting in the quantification of cracks.

Extensive experiments are conducted to derive thresholding limit, and it has been found that cracks are characterized by lower saturation and value in HSV space. The algorithm is tested for various test images, and the results shown in Figure 4 confirm the detection of cracks.

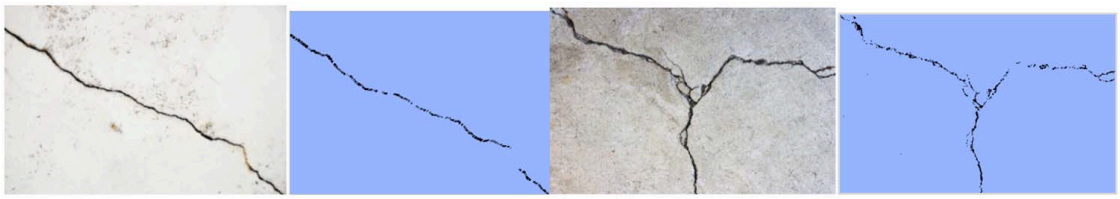

Figure 4: HSV thresholding crack output

Quantification of Cracks

Data acquisition method and image protocols are of prime importance in quantifying the cracks. The acquisition phase involves capturing images normal to the surface with an acquisition distance of 30cm-50cm with an RGB image resolution of 640 × 480 pixels. A test database was created that comprised of 20 images with different crack length and width. These images were taken during the evening hours in fairly bright condition.

To validate the accuracy of the developed protocols, some of the sample database images are tested using image segmentation approach to detect the edges of cracks and later used to find the crack width and length. In this approach, initially, the test images are converted into the binary images. The cracks and void structure to be segmented should differ greatly in contrast to the background. The gradient and threshold of the test images have been calculated and applied to create a binary mask containing the segmented cracks and voids. In order to achieve these tasks, edge and Sobel operators have been used. Figure 5a shows images of concrete prism that have undergone flexural loading. It should be noted that there

are black lines on the specimens that were drawn using black ink to facilitate positioning of the specimen during testing. These drawn lines do not represent any cracking. In addition, quantified crack lengths are given in Table 2.

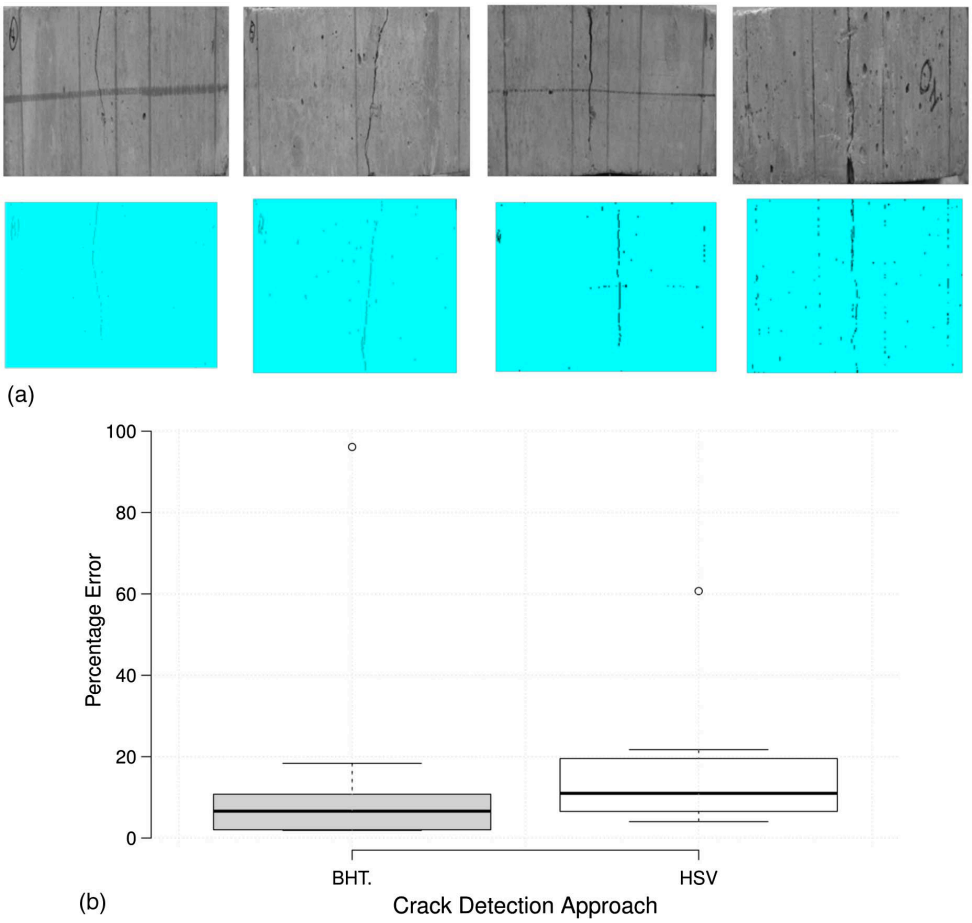

Figure 5: (a) Image database of samples with different crack sizes; (b) percentage error for BHT and HSV approach in comparison with actual measurements

Table 2: Comparison table for the Actual crack length vs. algorithm output

Image	**Actual measured Length of the crack (in cm)**	**No. of Crack Pixels**	**Computed Crack Length (in cm)**
Test Image a	10	643	9.18
Test Image b	12	872	12.457
Test Image c	10.5	793	11.36
Test Image d	10	1022	14.6
Note- Ratio of area in pixels to cm^2 = 877.71			

The crack length is obtained by considering all the detected crack pixels (no linearity is assumed). For example, if there are 'N' detected crack pixels (during the Calibration) where the distance between any pixels corresponds to '*x*' cm, then the overall N pixels corresponds to (N-1) * *x* cm. So, the algorithm performance depends on how effectively filters are

performing the classification and from Figure 5a it is obvious that detection efficiency is good to obtain close to the actual value. The actual measured length of crack was obtained using a handheld microscope.

In order to evaluate the overall performance of the developed algorithm, the whisker plots are provided (to show the overall percentage error) as shown in Figure 5b. It can be inferred from the plots that BHT and HSV perform with a percentage error of 10 and 20% respectively. Hence, the structural-based approach is preferable for its exactness and eliminates detection of other surface degradations from cracks.

Estimation of Surface Quality

The other important aspect of assessing the quality of civil infrastructure is to estimate surface deterioration. Surface degradation is characterized by the formation of color patches or loss of outer layer resulting in degradation of concrete/masonry surfaces. The primary cause is due to the prolonged exposure to environmental loadings such as heat, moisture, and chemicals. The histogram-based image thresholding is proven to be an effective strategy to quantify the surface deteriorations (Vázquez et al. 2011).

The proposed algorithm requires a user to select the unaffected area in a test image as an initial step. In the subsequent process, thresholding limits are automatically computed to classify the normal and degraded sections. The surface quality of images is assessed through histrogram analysis after identifying the affected area from the greyscale of test images.

The sample images shown in Figure 6a and Figure 6c are considered for the analysis. The processed images are shown in Figure 6b and Figure 6d. It can be observed that the finishing layer (plaster surface) of the test surface is degraded and severely spalled. To estimate this degradation, the histogram is applied to the test images, and the resulting output images are shown in Figure 6b and Figure 6d. The thresholding bounds are extracted from the user indicated surface area (in the red box) as shown in Figure 6a. The damaged area is computed in proportion to the image pixels belonging to the affected area.

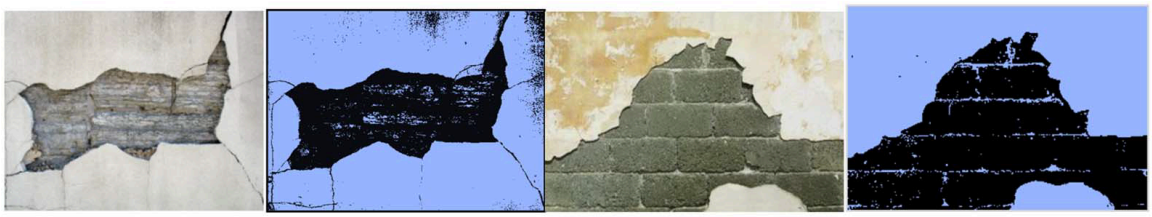

(a) (b) (c) (d)

Figure 6: Surface quality assessment using the developed image processing tool: (a) test surface 1; (b) test output 1; (c) test surface 2; (d) test output 2

2.5 Development of Graphical User Interface (GUI) and its Validation

A user-friendly graphical interface has been developed using MATLAB functions to examine the structural condition of civil infrastructures. This tool incorporates six structural deteriorations, as shown in Figure 7 that are considered to be prominent for evaluating the health conditions of structures. For each deterioration, various surface defects are accounted for. For example; for corrosion, there are three different defects that are considered as shown in Figure 7 and in which the severity level of damage is rated as the minimum (min), moderate (mod) and extensive (ext). The developed image processing

algorithm is integrated into the graphical user interface (GUI) to quantify the crack and other surface defects. In addition, fuzzy logic framework to generate MFs is also interfaced with the GUI where the user can visualize the condition rating of structures. The combination of image processing and fuzzy logic algorithms provide an effective evaluation strategy of civil infrastructures. After selecting the deterioration and corresponding defects, the cumulative damage is assessed as an element condition index. The calculated index value represents the criticality of the structure.

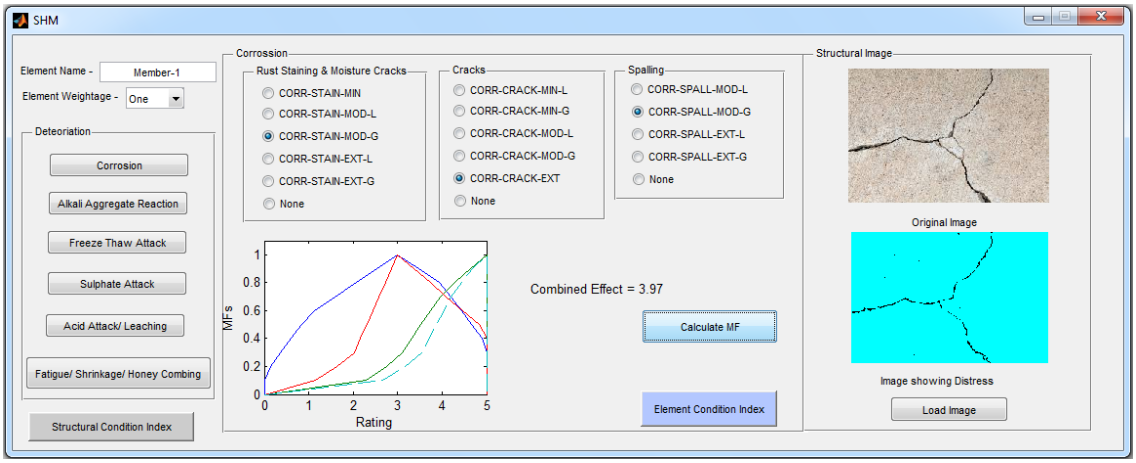

Figure 7: SCI evaluation using developed tool; distress and selected MF are for demonstration purposes only

The designed GUI for SHM, as shown in Figure 7 has two sections wherein Fuzzy sets and image algorithms are inculcated. The first section takes into account the deterioration effects based on corrosion, alkali-aggregate reaction, fatigue, shrinkage, honeycombing, acid attack, sulfate, and freeze-thaw attack. The other section computes the quantity and quality of the damage based on developed image algorithms. Captured images are loaded into the GUI using “Load image” option, correspondingly crack pattern, quantification of crack length, and quality of surface are computed. The properties of crack such as thin segmentation and random structural geometry are crucial to determine the length of the crack. Initially, the bottom hat transform filter is adapted to capture the thin segmentation, dark nature and random orientation. The unwanted edges are removed using Hough-based filter. The standard library tools available in Matlab are utilized to perform bottom hat filter, Hough transform and morphological operation such as erosion and dilation. In the case of detecting surface deterioration, a HSV-based filter technique is implemented. Initially, the algorithm is trained with several images having known crack lengths and accordingly thresholding parameters and filter size are optimized. The trained algorithm was further used for 20 images having varied crack lengths and the results were found to be consistent with manual measurements. The processed and original images are further helpful to identify the type of distress that has occurred, and they also can be used to identify global or local damage level. The image-based distress estimation is further utilized to quantify the SCI. On the selection of appropriate distress levels and by clicking the “Calculate” button on the GUI, the intensity level of combined distress is automatically computed and displays the result under “Combined Effect”. A sample calculation and the corresponding generation of MF is shown in Figure 7.

2.6 Case Studies

In order to validate the developed tool for civil infrastructures, a southern railway bridge located at Manavur, Tiruvallur and a storage building located near to Avadi, TamilNadu, India were selected as a case study. It should be noted that the discussion presented in this section is limited by a combination of some assumed damage initiation mechanisms and available list of deterioration codes presented in previous studies.

The digital images of bridge elements were captured and it was found that no remarkable damages have occurred on load-bearing elements. However, the authors believe that this bridge has predominantly been affected by heavy rain events and corrosion, which is the primary concern. Sample images shown in Figure 8a are fed into the developed GUI, and corresponding surface quality is evaluated, which are shown in Figure 8b and Figure 8a.

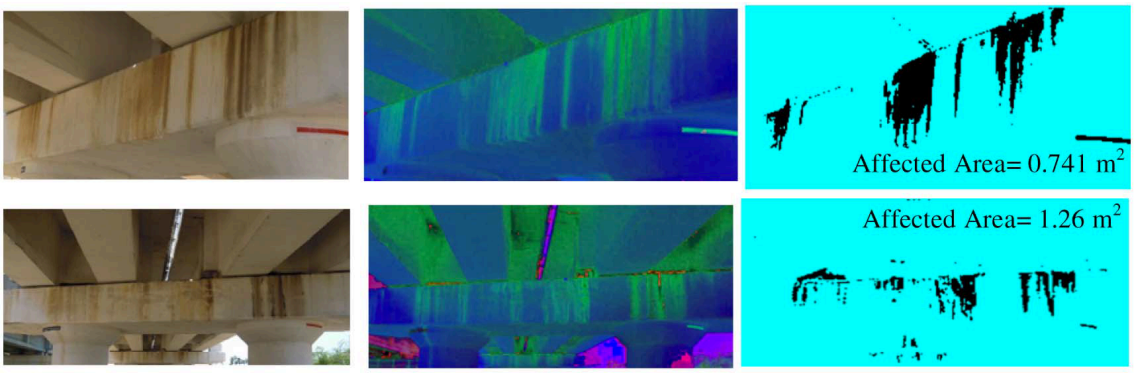

Figure 8: Pier cap of the railway bridge span 2 and 12: (a) site image; (b) HSV color space; (c) image showing distresses.

At this stage, rather than relying completely on human judgment, the surface staining can be quantified using the image algorithms discussed earlier in this paper and this value can be very useful in assigning a distress rating level. In Figure 8c it can be observed that the extent of staining seems fairly large, however since the damage is only superficial (aesthetic only) and not “erosion”, the deterioration component under the assigned code is selected as “ACID-ERO-MIN-G”. Moreover, it should be noted that due to the lack of a more suitable code in this existing study, “acid attack” has been selected as the primary mechanism. This results in a structural damage condition index (SCI) of 2.33. Since the bridge does not have any other degradation, the criticality of damage in the bridge structure is deemed minimal.

Similarly, for the condition assessment of the storage structure, a series of photographs are taken. The building is divided into four elements; Northside, East side, West side, and South side walls. Figure 9a shows a real image of outside and inside walls of selected elements. Northside wall is not considered in this study as it is free from any deterioration as it was covered by Asbestos Cement Roofing sheets. RGB images are fed into the GUI tool to detect the various distresses. Figure 9 shows the corresponding distress identified for the East wall element based on the developed algorithms. These RGB images and distress identified images will be used further to select the associated distress codes, which in turn evaluate the condition index for the East side wall element that is found to be 3.74. Similarly, condition index is calculated for other walls, as shown in Figure 10 and Figure

11. SCI considering equal weightage for all the elements are calculated as 3.68 as given in Table 3 based on the average weighted method that signifies the criticality of the structure. According to the evaluated SCI, it can be said that the building has medium damage condition. The entire storage building has been evaluated by considering the condition of each wall (individual MF), and then the overall combined effect of all the walls is considered. As can be seen that the individual wall has a condition rating of about 3 and more (as the cracks have more severe damage condition rating than the surface deterioration), the combined condition of all the walls turned out to be 3.68.

Table 3: SCI for the Storage building

Element Name	**Element Weightage**	**Assigned Codes**	**SCI due to each deterioration mechanism**	**Combined SCI for Each element**	**Combined SCI for the Structure**
East Wall	1	SHRINK-CRACK-EXT	3.4	3.7	**3.7**
		CORR-STAIN-EXT-G	3.0		
		SA-CRACK-EXT	3.4		
South Wall	1	SHRINK-CRACK-EXT	3.4	3.6	
		CORR-STAIN-EXT-G	3.0		
West Wall	1	SHRINK-CRACK-EXT	3.4	3.7	
		SA-CRACK-EXT	3.4		
		CORR-STAIN-EXT-G	3.0		

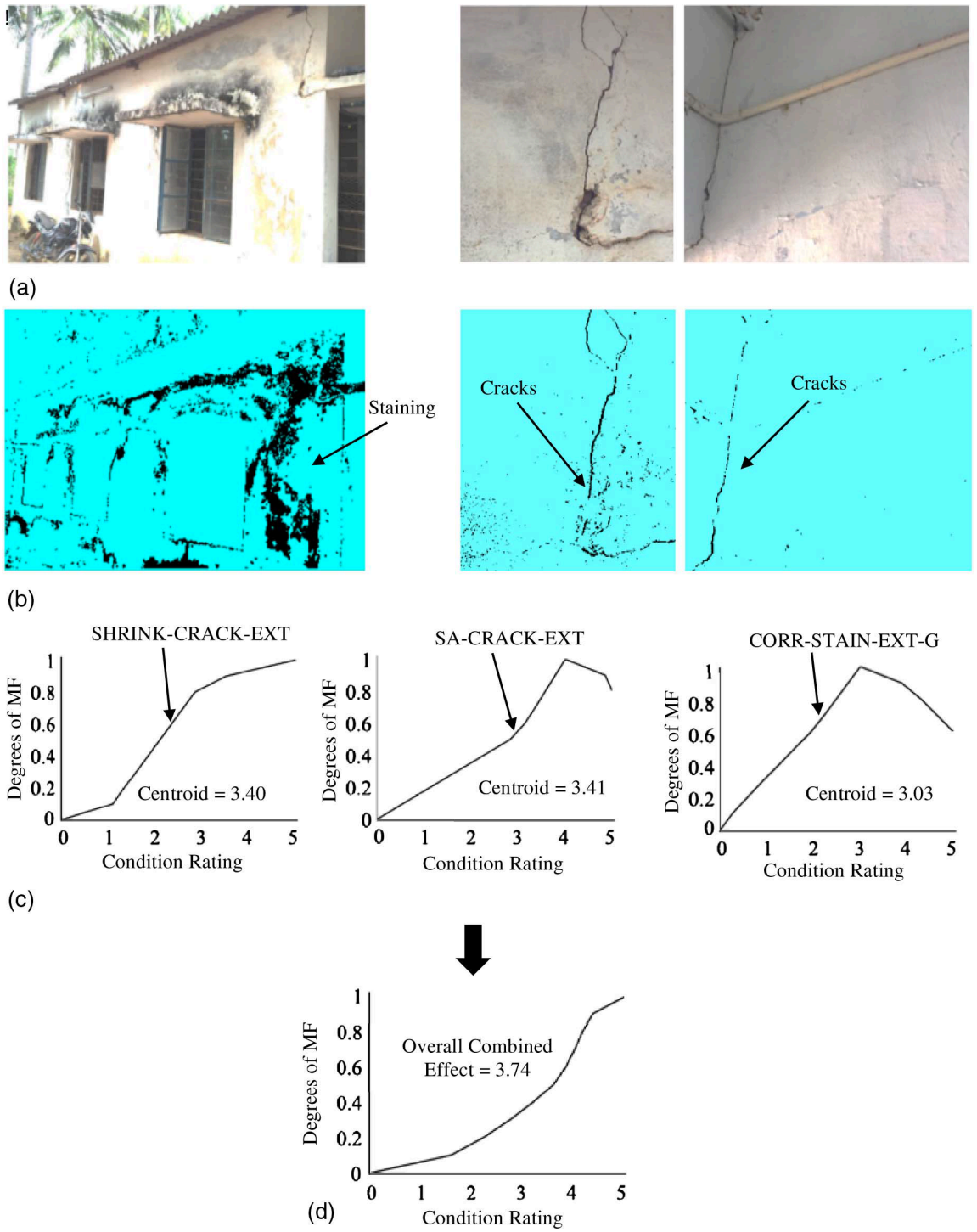

Figure 9: East side wall of storage building: (a) unprocessed images; (b) corresponding distress-identified images; (c) effect for each deterioration;

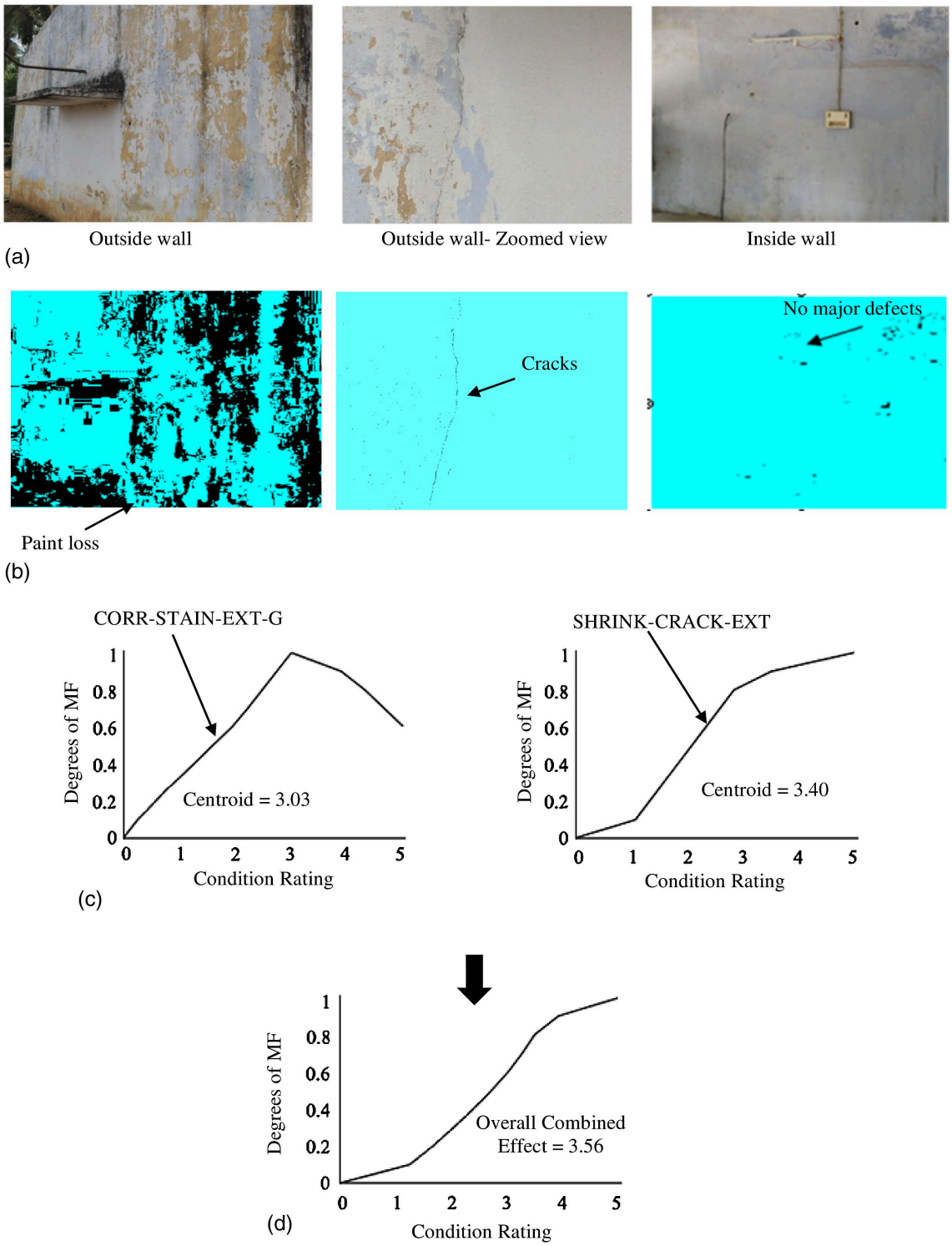

Figure 10: South side wall of storage building: (a) unprocessed images; (b) corresponding distress-identified images; (c) effect for each deterioration;

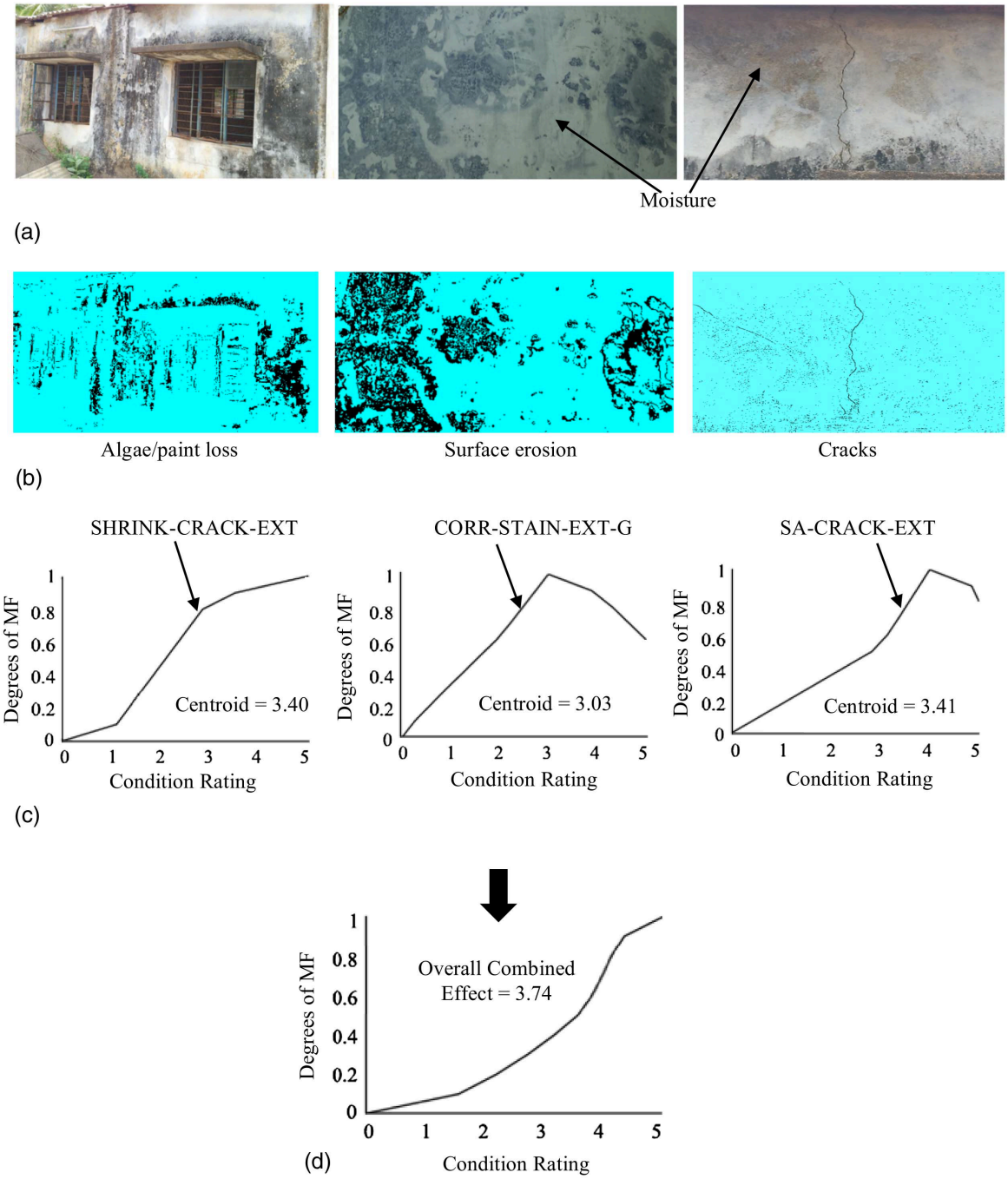

Figure 11: West side wall of storage building: (a) unprocessed images; (b) corresponding distress-identified images; (c) effects for each deterioration;

2.7 Conclusions

A GUI tool for rapid estimation of damage indices of civil infrastructure is developed. The formulated protocol bestows image functionalities and fuzzy sets to ascertain several structural distresses. Diverse imaging strategies are incorporated to accomplish detection and quantification of structural defects and also to provide a comprehensive evaluation of civil structures. In crack detection, BHT yielded an average error of 5% in comparison with HSV. The surface degradation is effortlessly appraised with HSV and grayscale thresholding methodologies. A simplified GUI tool is developed in MATLAB environment to ease the assessment of structures. Case studies are presented to examine the level of deterioration. Results reveal that the evaluated bridge attained 2.33 and the storage building had 3.68 as the damage index, which signifies the criticality of damage of each structure. In the future, robust sensor modules such as infrared thermal imaging and stereo mapping can be integrated for enhanced data acquisition and structural assessment. This inclusion provides sophisticated hardware-cum-software utility for rapid and effective evaluation of bridges, dams, monuments, buildings, and other structural members.

Chapter 3: Subsurface Simulated Damage Detection using Non-destructive testing techniques in reinforced-concrete slabs

Article Link : https://doi.org/10.1016/j.conbuildmat.2019.04.223

Harsh Rathod[1], Rishi Gupta[2]

[1]PhD Research Scholar, Department of Civil Engineering, University of Victoria, Victoria, BC, Canada, 778-350-7779, hmrathod@uvic.ca
[2]Associate Professor, Department of Civil Engineering, University of Victoria, Victoria, BC, Canada, 250-721-7033, guptar@uvic.ca

Note: This chapter is adapted in part from published work (Rathod et al., 2019a) in Construction and Building Materials, Elsevier, with permission where appropriate. This chapter presents the development of a model to refine multiple commercially available NDT techniques' data to detect and quantify subsurface defects. It uses 300 data points and multiple images of a total of 9 slabs to develop NDT data maps to detect and quantify subsurface defects. NDT data maps are given in section 3A of this chapter. At the end of this chapter in section 3B, GPR and cover meter are elaborated further to determine their applicability in identifying rebar characteristics in concrete structures.

3.1 Abstract

Most commonly occurring defects in RC bridge decks include voids, spalling, corrosion of reinforcement, leaching, scaling, cracking, honeycombing and delamination/debonding. Research related to the use of different NDT techniques to locate and identify different defects and its severity has been conducted in the past. Previous research work indicates that no particular technique is complete and each has its own advantages and limitations. This paper discusses the error values in the identification of the damage in reinforced concrete using NDT techniques. This research uses a total of five NDT techniques and their combination to detect the defects. For this, a total of nine 1800 mm × 460 mm reinforced concrete slabs with varying thicknesses of 100 mm, 150 mm and 200 mm have been prepared. These slabs have been embedded with artificial defects like voids, debonding, honeycombing, and corrosion. The experimental research shows that combining multiple techniques together in evaluating the defects give significantly lower error and higher accuracy compared to that from a standalone test. Combination of multiple techniques such as stress wave, electromagnetic wave, infrared thermography, and other electrochemical methods have been used for damage detection in reinforced-concrete slabs.

3.2 Introduction

Bridges are considered one of the most important elements of the transportation network in any country. Therefore, periodic monitoring and maintenance should be performed to check the safety and serviceability of these structures. The maintenance of bridges is of prime importance as it provides connectivity links for industrial and domestic movement of vehicles daily. Apart from personal mobility, the bridges support commerce and economic vitality. There is a significant number of bridges in Canada that are aging. According to recent (2016) Canadian infrastructure report card (Halsall, 2016), the current

deficit of replacing fair and poor municipal bridges (covers 26% of bridges) is 13 billion dollars. It should be noted that according to the report card, there are 57% of bridges that are in good condition. However, in order to save repair and maintenance costs in the future, the condition of these bridges should be monitored on a timely basis to make informed decisions.

Most common defects in RC bridge decks are voids, spalling, corrosion of reinforcement, leaching, scaling, cracking, honeycombing and delamination (AASHTO, 2011). Different NDT techniques have been adapted to detect different defects and their severity in the bridge elements. Previous research work shows that no particular technique is fully complete and each has its own advantages and limitations (Conde et al., 2017; Breysse et al., 2012). This paper discusses the use of a combination of multiple NDT techniques in identifying the subsurface damage in RC slabs.

Non-Destructive Testing techniques

American Concrete Institute committee report 228.2R (ACI-228.2R, 2013) lists about twenty different NDT techniques with their summary of potential application. The discussion below is limited to the NDT techniques that were used in this study. Only the NDT techniques that were used, are described here.

Ground Penetrating Radar (GPR)

The most common and wide use of GPR has been found for mapping delamination in RC, detecting pipes, finding steel rebars and identifying the thickness of pavements for several years (Zhao et al., 2017 and Ayala-Cabrera et al., 2011). Apart from the identification of the defects in RC, GPR is also being used for verifying design plans by mapping the true rebar grid layout and prestressing tendons (Cruz et al., 2010).

GPR technique detects the changes in electromagnetic properties of the material from the reflected electromagnetic waves that are sent into the material's subsurface. The technique uses frequency modulation, synthetic pulse-radar, and pulse systems for structural applications. However, pulsed system method has been found to be used widely in most of the equipment. It uses high-frequency-pulsed electromagnetic waves (from 10 to 3000 MHz) (often being called as radar waves) to acquire subsurface information. The present research uses a GPR that utilizes 2600 MHz electromagnetic waves transmission antenna to detect the subsurface flaws.

The GPR equipment normally consists of two antennas, a transmitter, and a receiver. In addition, the system consists of a radar control unit, data acquisition system, and display devices. A 3-dimensional mapping function provided by GSSI (Geophysical Survey Systems Inc.) has been used in this research to map the subsurface anomalies as a function of the depth of slabs.

GPR's popularity is due to its advantages over the other techniques. Benedetto et al., 2015 describes the advantages of GPR and the major GPR strengths for its use in the field of civil engineering. These include the non-destructive nature, rapidness, lower costs compared to the traditional methods, and higher reliability in the measurement.

Infrared Thermography (IRT)

Flaws in concrete can be detected using an infrared camera by capturing the thermal difference produced between the flaws and surrounding sound concrete. The difference in

the temperature between flaws and surrounding sound concrete is created by the radiant heating from the sun. The heat is conducted through the concrete and disrupted by the presence of flaws in the concrete and creates the temperature variation at the surface of the concrete.

ASTM D4788, 2013 standardizes IRT for detecting delamination in bridge decks. According to the standard, an infrared camera could possibly identify the delamination if there is a temperature difference, between the delaminated or debonded area and the adjacent solid concrete of at least 0.5ºC and weather condition includes sunshine. The same has been confirmed with other research work on IRT (Clark et al., 2003 and Washer et al., 2009).

IRT is capable of detecting concrete defects (e.g., delamination) as small as 50 mm in width (Bhalla et al., 2009). To verify this capability, Bhalla et al. performed an experiment in which specimens of size 100 x 100 x 500 mm were first heated up using four 1 kW halogen lamps for about 30 min. Defects in the form of 90 x 50 x 0.5 mm thick glossy printer paper sheets were detected using the thermal images. Conclusive remarks by Bhalla et al. are referred to the size of the defect and not the depth at which it can be detected using infrared thermography.

Similar work has been done by Yehia et al., 2007. In their work, three slabs with induced defects at different depths were cast. To mimic the real bridge deck situation three main types of defects were simulated: cracks, delamination, and voids. Defects were detected using infrared thermography. Current research uses a modified simulation of these defects. Further description of this is given in the experimental section of this paper.

Infrared thermography has many more advantages such as scanning a larger area, detecting defects between layers and the cost-effectiveness (Yehia et al., 2007). Another advantage of this technique is that the infrared camera can be mounted on an Unmanned Aerial Vehicle (UAV) to inspect inaccessible areas of the bridge.

Electrical Resistivity (ER)

ER of a concrete surface is an indication of the concrete's resistance to penetration of chloride ions. Higher the resistance better the concrete quality.

Based on the AASHTO (TP 95-11, 2013) guidelines, an alternating current (AC) potential difference is applied by the Wenner probe at the outer pins of the Wenner array that generates the flow of current. The inner pins of the Wenner probe measure the potential difference. The surface resistivity of concrete is calculated by accounting the current used, applied potential and the affected area. Depending upon how closely the tip of Wenner probe is spaced, the penetration depth of the current flow can be identified. However, the determination of an absolute value of the depth is complicated due to the factors that affect electrical resistivity. The apparent resistivity can be calculated using equation 3.1,

$$\rho = 2\pi aR \tag{3.1}$$

Where,

$\rho =$ Apparent Resistivity

$a =$ tip spacing

$R =$ Resistance

Minimum tip spacing suggested in TP 95 is 38 mm. The resistivity, in Kilohms-centimeters (kΩ-cm), has been found to be related to the resistance of the specimen to chloride ion penetration. TP 95 gives the chloride penetration level based on the resistivity value. It should be noted that the values are obtained for the cylinders of size 100 × 200 mm and 150 × 300 mm and cannot be applied directly to the RC test specimens used in the experimental study here.

Test Standards of ER (TP 95-11, 2013 and ASTM-C1202, 2017) report that the Wenner probe setup should not be used on the samples containing rebars as the presence of rebar modifies the current distribution and the potential drop of a four-electrode arrangement in concrete specimens and components. However, research shows that with the modification and consideration of the rebar factor based on the geometry, the setup can be used on RC slabs (Garzon et al., 2014). A practical compromise appears to be an electrode spacing of 30 to 50 mm (Polder, 2001). In the current investigation, the authors have used the probe with a tip spacing of 38 mm to avoid the influence of rebar. It should also be noted that the ER results are affected by the environmental parameters such as moisture content, and temperature (Sengal, 2014). In the present research, in order to avoid the environmental effect, the data were collected at the same time on all the slabs.

The ER has been applied on the concrete samples to determine the coefficient of variation of repeatability, reproducibility and local variability. It has been found that the technique has very low (about 5%) coefficient of variation of repeatability, reproducibility and local variability (Lataste, 2013).

Ultrasonic Pulse Velocity (UPV)

A number of stress wave techniques such as impact echo, resonant frequency test, UPV and acoustic emission etc. have been used on bridges for damage detection (Xiao et al., 2015 and Miller et al., 2013). Due to UPV's simplicity, current research uses UPV as one of the stress wave techniques. The test was performed according to (ASTM-C597, 2016).

Researchers have found multiple relationship models of compressive strength of concrete and velocity in the concrete (Haung et al., 2011 and Leslie et al., 1949) UPV includes three types of measurements 1) Direct 2) Semi-direct and 3) In-direct measurement. The direct pulse velocity measurement is the most accurate method. However, it is not feasible in most of the cases. Transducers are kept perpendicular to each other on two different surfaces in the semi-direct method. In the in-direct method only one surface is used and the transducers are kept at a certain distance on the same surface of the concrete.

UPV technique applied on Frontenac Dam located in the Eastern Townships region of the Province of Quebec, Canada shows that the technique could be used to identify and compare the damage in spillway concrete piers qualitatively (Saint-Pierre et al., 2016). During their research, the authors proposed Concrete Quality Designation (CQD) technique to determine the degree of damage in concrete relative to its original and undamaged condition. It should be noted that all the piers were inspected using the semi-direct method.

UPV performed on RC specimens was correlated to the dynamic modulus of elasticity of the specimens. Also, using the different transit time of the P-wave (fastest UPV wave), delamination at a different level of the slabs were found (Petro et al., 2012). The research

stated that the transit time of P-wave obtained during direct tests was consistent with the transit time of P-wave obtained during indirect tests.

Practitioners should be careful when interpreting the results from the UPV as without additional knowledge about the interior condition of the concrete. The reduced pulse velocity could be incorrectly interpreted as a low compressive strength or poor quality concrete (ACI-228.2R, 2013). In the current research, the data obtained using UPV (Only P-Wave velocities were considered) has been correlated with the other NDT techniques in order to interpret the results correctly.

Half- Cell Potential (HCP)

The technique measures the potential difference between a standard portable half-cell, normally a copper/ copper sulfate (Cu/CuSO4) standard reference electrode placed on the surface of the concrete with steel reinforcement underneath. The steel reinforcement is required to be connected to the voltmeter to measure the potential. Based on the half-cell potential readings, the probability of the corrosion can be determined. ASTM C876, 2015 standardizes the corrosion probability based on potential values.

HCP is one of the electrochemical-based methods to detect the corrosion in concrete structures. It is proven to be an accurate electrochemical-based method to find the probability of corrosion in the concrete structures. The advantage of HCP measurements is that it indicates corroding rebars not only in the most external layers of reinforcement facing the reference electrode but also in greater depth (RILEM TC-154-EMC, 2004). However, it should be noted that the half-cell potential is influenced by the concrete cover, chloride content, compressive strength and moisture content (Yodsudjai et al., 2017). In the present research by the authors, half-cell values were compared by keeping the aforementioned parameters constant in all the slabs.

3.3 Experimental Methodology

The Experimental methodology consists of the preparation of the RC test specimens, and data collection using NDT techniques.

Preparation of RC test specimens

A total of nine 1800 mm × 460 mm RC slabs with varying thicknesses of 100 mm, 150 mm and 200 mm have been prepared using 25 MPa concrete. The slabs were designed as a one-way slab with l/b = 3.9. The slabs were prepared with varying thicknesses to determine the performance of NDT techniques at different depths. Steel reinforcement of diameter 10M (CSA standard notation) =11 mm was used in both longitudinal and transverse directions. Total of 0.68%, 0.46% and 0.34% flexural steel (Longitudinal direction) was used in 100 mm, 150 mm and 200 mm slab respectively. It should be noted that the slabs were not designed for a particular moment of resistance. However, based on the Canadian design standard (CSA A23.3) maximum steel spacing limit of 250 mm was met. Transverse steel was used just to avoid the shrinkage cracks in the concrete. Bottom cover to the reinforcement was kept as 12.5 mm to promote the spalling of concrete during accelerated corrosion cycles later in the future. Side cover was kept as 40 mm.

Table 4 shows the types of defects induced inside the RC slabs. As mentioned earlier, the embedded artificial defects are modified from (Yehia et al., 2007). In Yehia et al.'s research, void/delamination was created using the Styrofoam blocks, however during the

preliminary phase of the proposed research work it was found that, it is difficult to ensure that the styrofoam blocks are completely dissolved. In order to avoid this problem, voids were created using cardboard paper box, as shown in Figure 12. Present research work also includes the specimens with sea salt ingress for the corrosion of rebar mesh. It should be noted that the sea salt was added only in the middle third portion of the slab during casting of the slabs to accelerate the corrosion progress. The amount of sea salt by weight of water (190 kg/m^3) content in RC slabs is mentioned in Table 4.

Table 4: Types of induced defects in each slab

Type of Defect	**Approximate Dimension (mm×mm×mm)**	**Location in 100 mm, 150 mm and 200 mm slab**
Void (created using cardboard paper box)	178×76×38 and 87×76×38	30 mm, 80 mm, 130 mm (from top)
Honey combing (Pocket of loose aggregates)	50×50×20	80 mm, 130 mm, 180 mm (from top)
Debonding (Sand sleeves around rebars)	Cylindrical sleeve of 20 mm dia.	80 mm, 130 mm, 180 mm (from top)
Sea salt/Corrosion	3.4 % of the weight of the water in concrete	Middle third portion of the slab

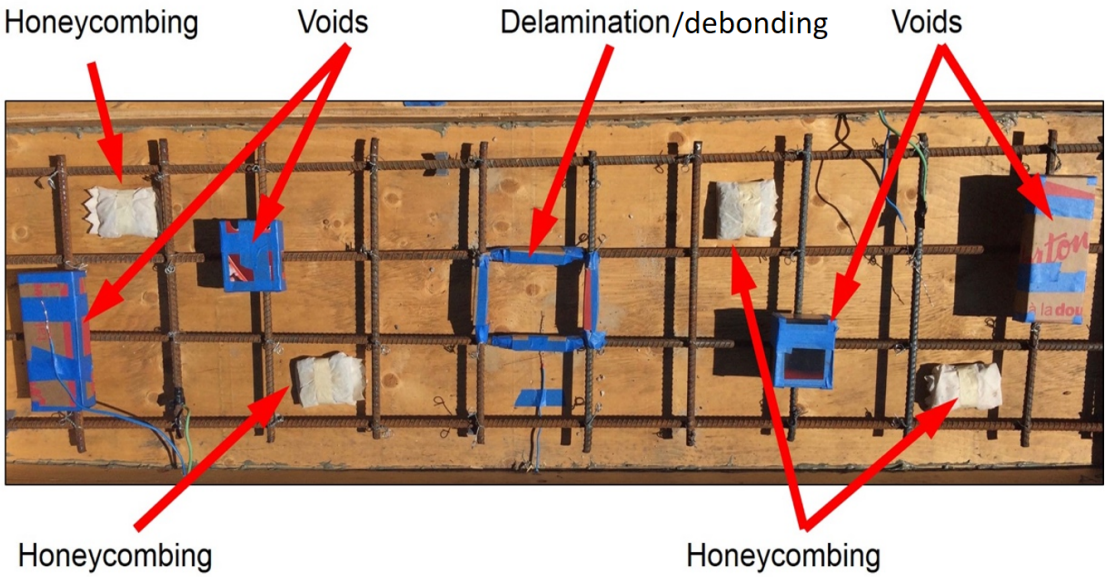

Figure 12: Details of Embedded Defects

Out of the total 9 specimens, 3 specimens with artificial defects and 3 with sea salt were cast. The remaining 3 were used as control specimens to validate the results obtained by proposed NDT techniques. Figure 12 and Figure 13 show the details of size, shape, and depth of the defects at which they were embedded in the slabs. There were two each type of defects embedded in the RC test slabs to check the accuracy of NDT technique in identifying the same type of defect at multiple locations. Figure 13 shows that voids and

debonding were embedded at rebar level while honeycombing defects were created at the bottom of the slabs. Due to varying thicknesses of the slabs, the distance of the defects from the top surface of the slabs are different. This allowed NDT techniques to identify the defects at different depths.

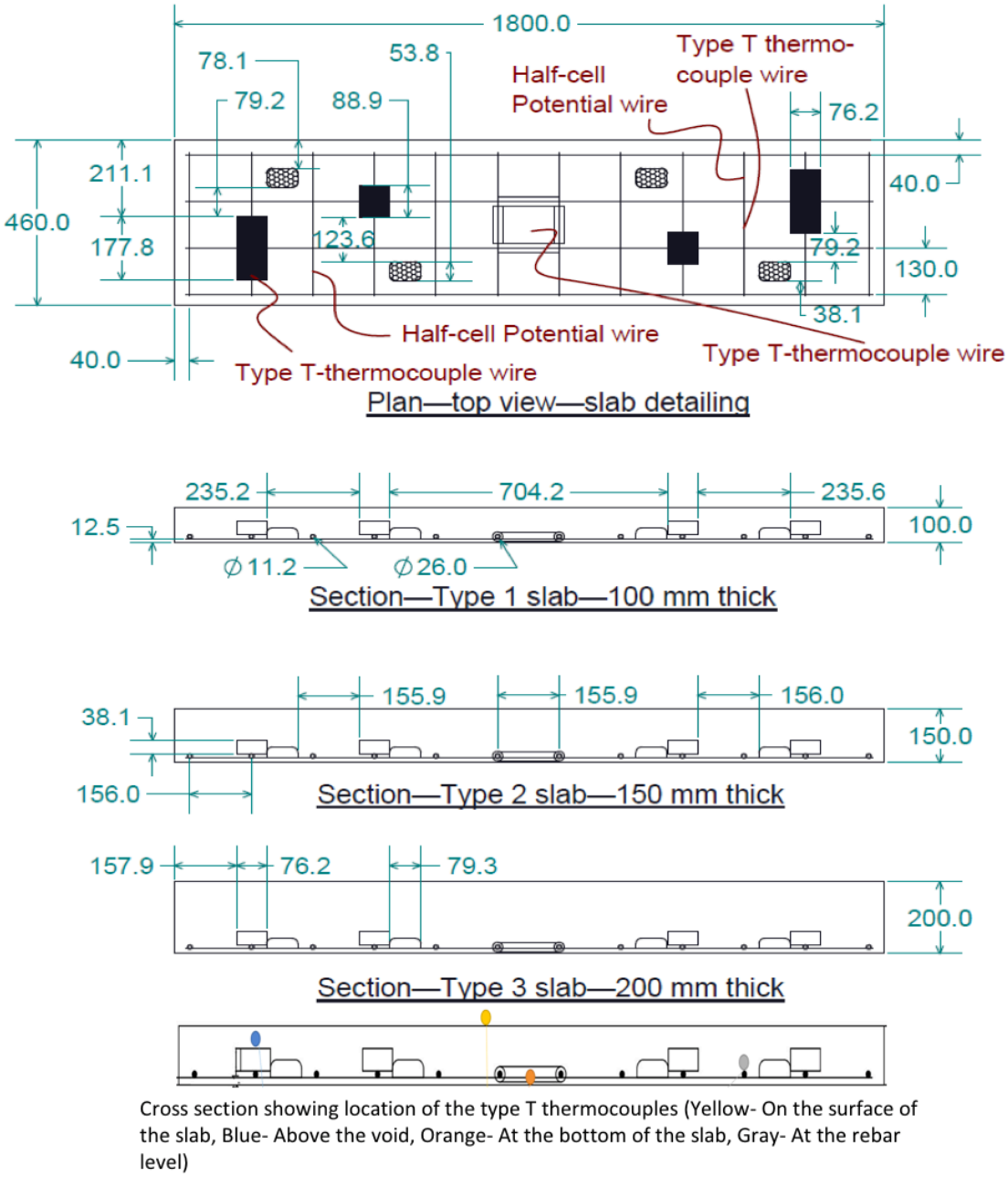

Cross section showing location of the type T thermocouples (Yellow- On the surface of the slab, Blue- Above the void, Orange- At the bottom of the slab, Gray- At the rebar level)

Figure 13: Details of RC test specimens with embedded defects

In order to measure the subsurface temperature of the RC slabs, type T thermocouples were embedded at different locations as shown in Figure 13. The subsurface temperature was used to correlate with the infrared-based thermographic measurements. The subsurface temperature data was monitored using the type T thermocouple- Humbolt- Data

Acquisition System (DAQ) system. The maximum data logging rate with this system was one measurement at every 30 min.

It should be noted that all the NDT techniques were performed in the ambient environmental conditions. The slabs were subjected to the winter and summer cycles while being monitored. In Victoria, BC, Canada, the temperature range during summer hours is 12 ºC – 24 ºC and during winter hours is 3ºC – 9ºC. These numbers are long-term historical averages based on climate data (provided by Environment Canada) gathered from 1981 to 2010. The effect of summer and winter cycles will be useful in determining the chloride ion diffusion for long –term using HCP.

The experimental set up is shown in Figure 21, where all nine test specimens were placed together on 1.5 feet high concrete blocks to access the slabs from the bottom as well if required in the future.

Data Collection using NDT techniques

As mentioned in the previous sections of this paper, data were collected using different NDT techniques. Methodology for each NDT is described in this section.

As shown in Table 9, a handheld FLIR E60 camera was used to acquire infrared thermographs of the test specimens. The acquisition distance was kept as 3 ft. (about 0.9 m) constant to the top surface of the slabs so as to cover the third portion of the slab. Total three thermographs per each slab were captured to cover the entire slab. Thermographs were taken only of the top surface of the slabs.

For the UPV test, two transducers and a Data Acquisition (DAQ) System from Proceq were used to collect indirect data from the test specimens. As highlighted in the introduction section, the indirect transmission is not an accurate method of measurement however, it is the most feasible. The transducers having a frequency of 54 kHz were used in this study. Both the transducers were kept approximately 130 mm apart on the rebar grid points (longitudinal and transverse rebar junction points) to obtain the velocity values of the RC slabs. This resulted in a total of 44 points per slab.

For measuring the surface electrical resistivity of the RC test slabs, four-point Wenner probe setup (Resipod) from Proceq was used. Since the presence of reinforcement affects the electrical resistivity results, as per the suggestion of Proceq operating manual, Resipod was set in such a manner (as shown in Table 9) that it avoids the influence of rebars.

In order to measure the corrosion potential of the RC slab, a copper-copper sulfate probe called half-cell was used along with a voltmeter. Measurements were taken on the same grid of 132 mm × 156 mm as used for the UPV and ER. It should be noted that the chosen density of readings is quite high. This is in order to enable the establishment of a good correlation between the techniques.

GPR equipment- StructuresScan Mini from GSSI (Geophysical Survey Systems, Inc.) requires finer grid/mesh when scanning the RC elements. A mesh size of 2 inches × 2 inches (50 mm × 50 mm) was used when collecting the data which resulted in a total of 15 scans for both the directions.

3.4 Results and Discussion

Data collected using the NDT techniques were mapped onto contour and image intensity maps (Included in 3A). The maps were presented in a set of three to visualize them more

effectively. Errors are calculated for each NDT based on the following five categories of defects identification,

1) Detection Capability
2) Locating Capability
3) Calculating the affected area
4) Calculating the depth of the defect
5) Calculating the volume of the defect

Equations for calculating error values (in percentage) for each category are listed below.

$$\text{Detection } (F_1) = 100 - \left(\frac{\text{No. of Defects Detected}}{\text{nd}} \times 100\right) \quad (3.2)$$

$$\text{Location } (F_2) = 100 - \left(\frac{\text{No. of Defects Located}}{\text{nd}} \times 100\right) \quad (3.3)$$

$$\text{Area } (F_3) = \frac{\sum_{j=1}^{j=nd}[\%\text{error in area}]}{\text{nd}} \quad (3.4)$$

$$\text{Depth } (F_4) = \frac{\sum_{j=1}^{j=nd}[\%\text{error in depth}]}{\text{nd}} \quad (3.5)$$

$$\text{Volume } (F_5) = \frac{\sum_{j=1}^{j=nd}[\%\text{error in volume}]}{\text{nd}} \quad (3.6)$$

Where,
nd = Total Number of defects present

Equation 3.2 determines the detection error by calculating the number of defects detected by individual NDT methods. Equation 3.3 determines the location error by calculating the number of defects detected at the correct location by individual NDT methods. Similarly, equations 3.4-3.6 are used to determine the total percentage error related to the area, depth, and volume by calculating the percentage errors (at all the location) in determining the correct area, depth and the volume of the defects respectively. Result obtained for each NDT technique is discussed below individually.

1. Ground Penetrating Radar (GPR)

As mentioned in the earlier section, a 3-D mapping feature provided by GSSI was used to present the data in the form of intensity maps presented in Figure 22 and Figure 23. The 3-D mapping feature identifies the peak of hyperbolas on X, Y and Z (Depth) co-ordinates to present it as a 3-D map. It should be noted that the input information used in 3-D map is from the GPR line-scan. The feature is helpful in identifying and mapping defects without manually marking the peak of set of hyperbolas in a line scan. As can be seen from the maps, due to the difference in the dielectric constants of steel and concrete, rebars were easily identified with an accurate spacing. As the thickness of the slab increases, signal attenuation was observed due to high-frequency antenna.

It was found that the 2600 MHz antenna does not work well to identify the layout of the bottom layer of rebar when the slabs have a thickness greater than 200 mm.

It can be seen that the GPR can detect subsurface anomalies based on the difference in dielectric constant between the concrete and the flaws. Using the GPR, various depth slices can be obtained to inspect the subsurface information at various depths. The intensity maps show the depth slice just above the bottom rebar grid to identify the flaws. The defects that

were detected are labeled in the figure with a check (✓) mark, and the ones that were not detected are highlighted with a cross (X) mark.

Area, depth and volume of defects were also determined using the GPR. These calculations are shown in Figure 24 and Table 5.

Table 5: GPR- Error values for area, depth and volume categories

Calculation of area of voids (mm^2)					
Thickness of slab	Area 1	Area 2	Area 3	Area 4	% Error (F_3) (Equation 3.4)
100 mm	12500	8750	7500	7500	24
150 mm	17250	6750	4400	11250	20
200 mm	20700	7425	5280	14062	22
Calculation of depth of voids from the top surface (mm)					
Thickness of slab	Depth 1	Depth 2	Depth 3	Depth 4	% Error (F_4) (Equation 3.5)
100 mm	25	25	25	25	17
150 mm	76	76	76	76	5
200 mm	114	114	114	114	12
Calculation of volume of voids (mm^3)					
Thickness of slab	Volume 1	Volume 2	Volume 3	Volume 4	% Error (F_5) (Equation 3.6)
100 mm	656250	459375	393750	393750	48
150 mm	888375	347625	226600	579375	33.5
200 mm	1314450	471488	335280	892937	88

It should be noted that in order to calculate the area, depth and volume, the defect was enclosed by a rectangular box. The area of the box was determined by the width and the height of the enclosing box from the GPR 3D grid map. The area of the rectangle was used in calculating the area and volume of the defect. Figure 14 shows the error of GPR in identifying the subsurface defects in the RC slabs. The error values for the defects that were not detected (considered as 100) using GPR, are not plotted in Figure 14. It can be seen that the GPR was successful in detecting all the voids present in the slabs.

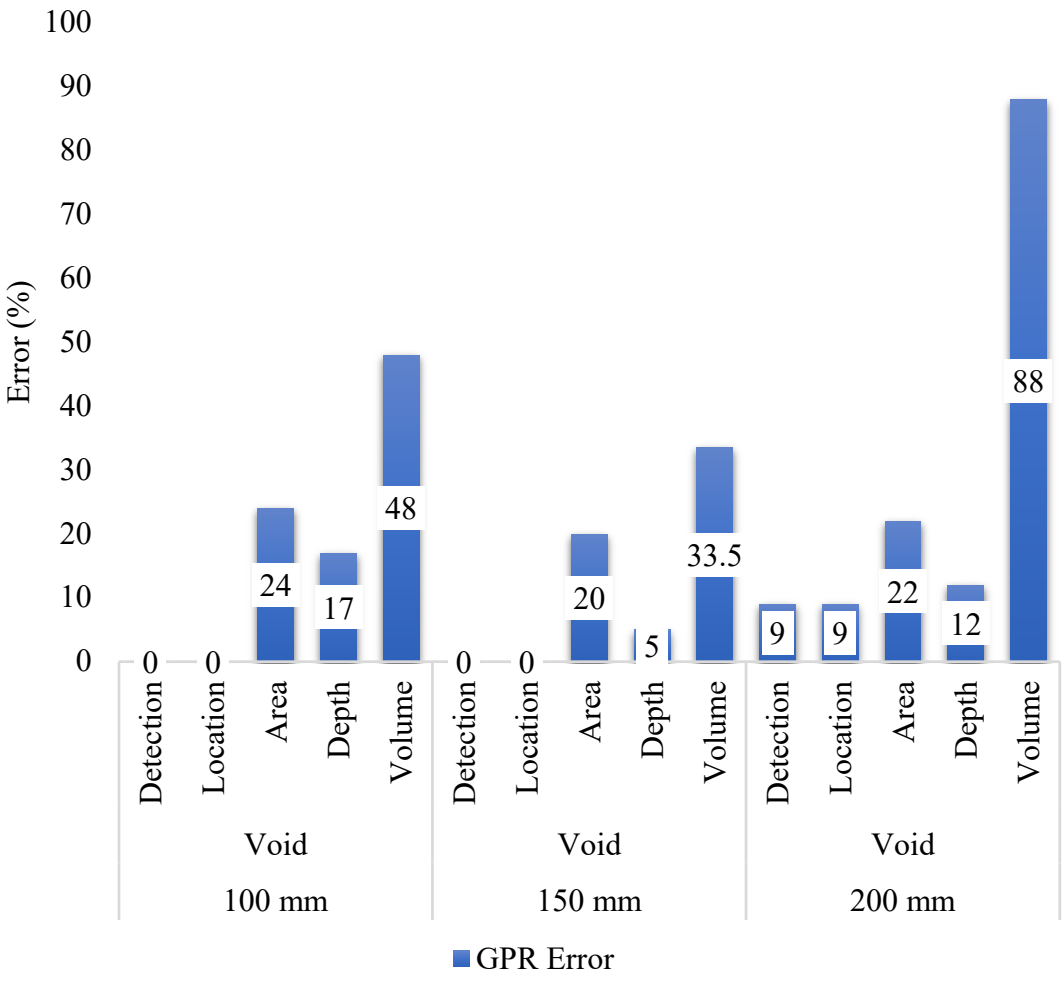

Figure 14: Error of GPR in identifying the subsurface damage in reinforced concrete

2. Infrared Thermography (IRT)

As mentioned in the introduction section, the capabilities of IRT in detecting defects in the concrete are highly dependent on the environmental conditions. The environmental (outdoor) conditions vary depending upon the geographic location. As noted earlier, in Victoria, BC, Canada, the temperature range during summer hours is 12 ºC – 24 ºC and during winter hours is 3 ºC – 9 ºC. Due to such low range of temperature, IRT was limited to detecting voids only in the 100 mm thick RC slab. The infrared thermographs are shown in Figure 25. The thermographs show that only voids were detected in 100 mm slab. In order to calculate the area of these voids, the infrared thermographs were processed in MATLAB software. Following four steps were followed in order to calculate the area of voids,

1) Each IR image was converted into a numerical array and combined to get an equivalent array that represents an image,

2) The matrix of 240 × 960 pixels was converted into 456 ×1824 pixels to match the dimension of the RC slab-460 × 1800 mm,

3) In order to calculate the area of voids using segmentation in MATLAB, the matrix data type was changed from double to logical using the function imbinarize, and

4) To get close to the exact solution, an adaptive threshold with a sensitivity of 0.71 and close mask with rectangle was applied. The function adaptthresh computes a locally adaptive threshold for a 2-D grayscale image or 3-D grayscale volume. The adaptthresh function chooses the threshold based on the local mean intensity (first-order statistics) in the neighborhood of each pixel.

Table 6 shows the calculation of error in identifying the area of the voids. The error was calculated using equation 3.4 noted earlier. It should be noted that before calculating the percentage error between actual area and area in pixels, areas in pixels were converted into mm^2 using the ratio of actual area to the pixels' area.

Table 6: IRT- Error values for area category

Ratio of act area in mm^2 to calculated area in px	**Area-void 1**		**Area -void 2**		**Area - void 3**		**Area - void 4**		**Error (F_3) for 100 mm thick slab**
	Act	px	Act	px	Act	px	Act	px	
1.026	13528	17354	6612	8355	6612	9140	13528	19139	36.8

Act= Actual
px = Pixels

Subsurface temperature data obtained using the thermocouples during the summer hours show that the temperature difference between the void and a few millimeters above the void (void surface) decreases as the depth of slab increases as can be noticed in Figure 15. For a 100 mm thick slab, the temperature differences ΔT_1, ΔT_2, and ΔT_3 were found to be higher than that of the 150 and 200 mm thick slabs, as shown in Figure 15. For the 150 mm slab, ΔT_1, ΔT_2, and ΔT_3 were found to be almost 0. It can also be inferred from the thermocouple data that as the thickness of the slabs increases, the subsurface temperature of the voids shows a slight shift (a lag in subsurface temperature) in the profile due to higher thermal conductivity but lower heat capacity. The time lags (Δt) in 100 mm, 150 mm and 200 mm thick slabs were found to be 0 hour, 1 hour and 4 hours respectively. It should be noted that the temperature differences ΔT and time lags Δt were calculated during the heating hours of the day. The same can be calculated during the cooling hours as well. The only difference would be that, in the infrared thermographs, the temperature profile of the voids would be different (opposite) during the cooling and heating hours.

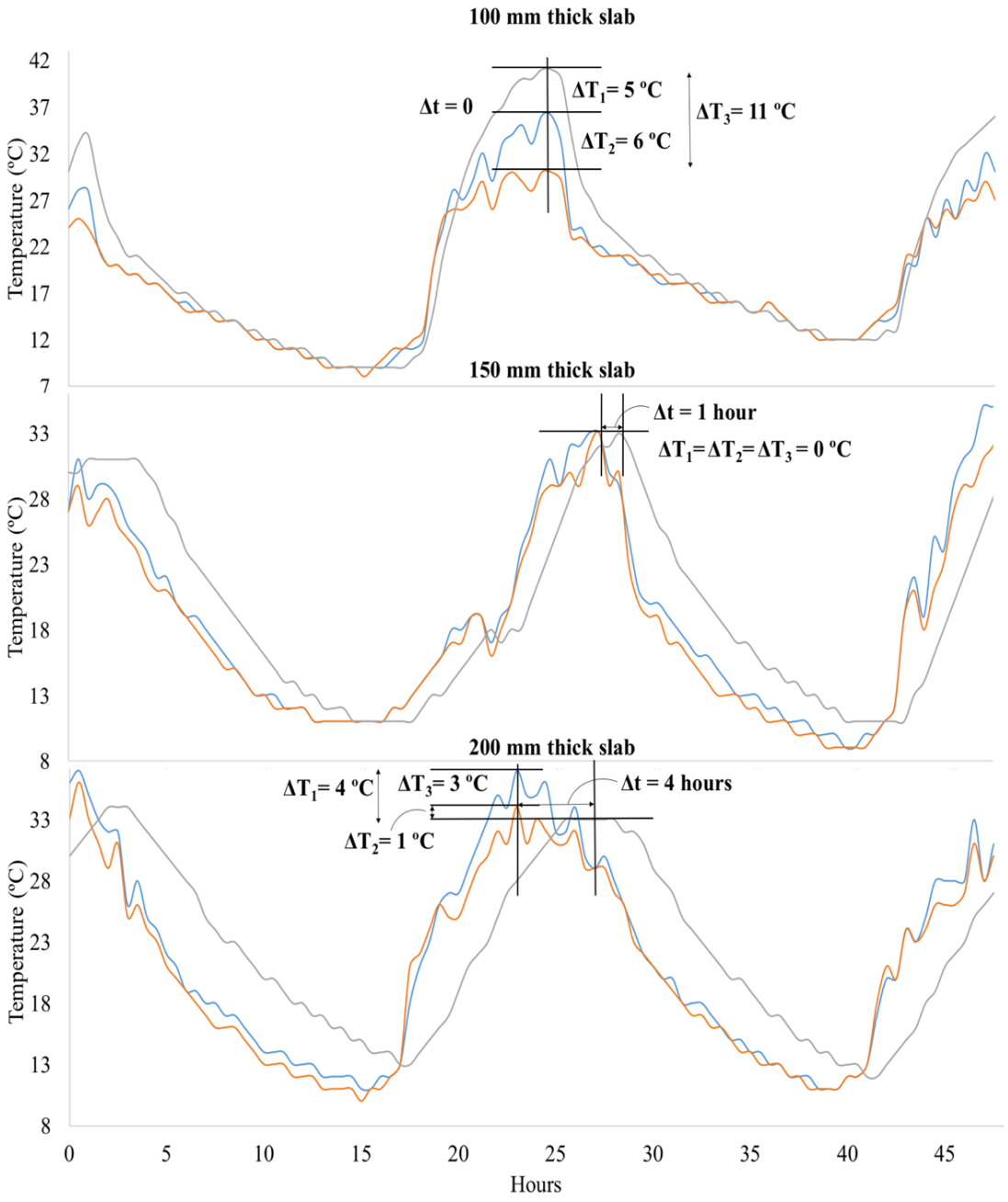

Figure 15: Temperature lag and time lag between void and sound concrete -100 mm, 150 mm and 200 mm slabs

Figure 16 shows the errors for IRT in identifying defects in only 100 mm slab. It should be noted that the error value for 150 and 200 mm slabs is 100.

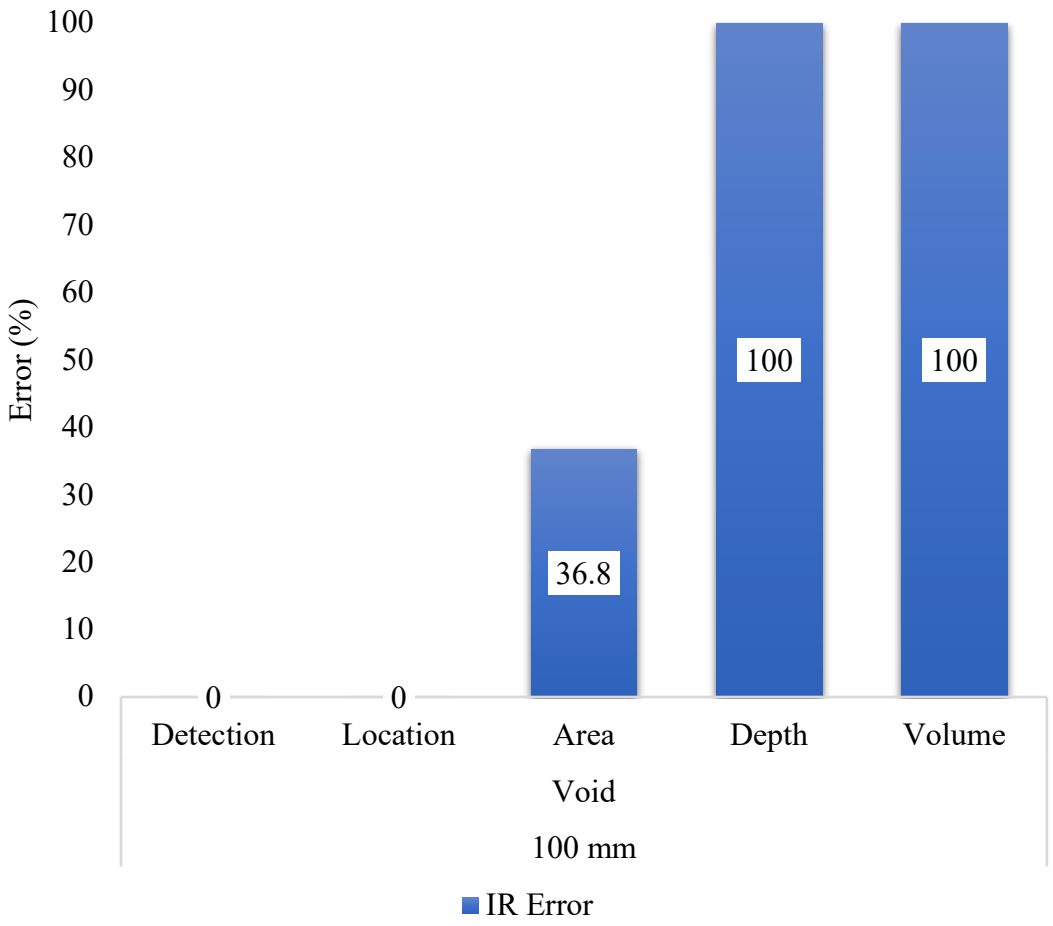

Figure 16: Error of IRT in identifying the subsurface damage in reinforced concrete

3. Electrical Resistivity (ER)

The data collected by the Wenner probe was manually recorded and plotted on contour maps. These contour maps are shown in Figure 27 and Figure 28. It can be seen from the contour maps of the control slabs, that there is variation in data even for control slabs. However, the spread of data is within 60kΩcm. This data was treated as a baseline to identify defects in the other slabs. A threshold value of ≥ 80 kΩcm was chosen to detect defects in all slabs. This threshold value is nothing but the average ER value of the control slab. It should be noted that even though the concrete having higher resistivity values has the low potential of chloride penetration (Azarsa et al., 2017), in this study surface resistivity values of concrete near voids were found higher compared to the surrounding concrete due to the fact that air has higher ER compared to concrete.

The errors were calculated based on the number of defects detected. Error value of 0 was assigned if all the defects (e.g., voids) are detected. When not even a single defect was detected, error value of 100 was assigned. This can be seen in Figure 17. It was observed that the error for 100 mm slab was found to be higher than for 150 and 200 mm slabs. The authors hypothesize that other than the implicit errors associated with the ER technique, the lack of void detection could be due to the uneven concrete surface and lack of probe contact (Azarsa et al., 2017).

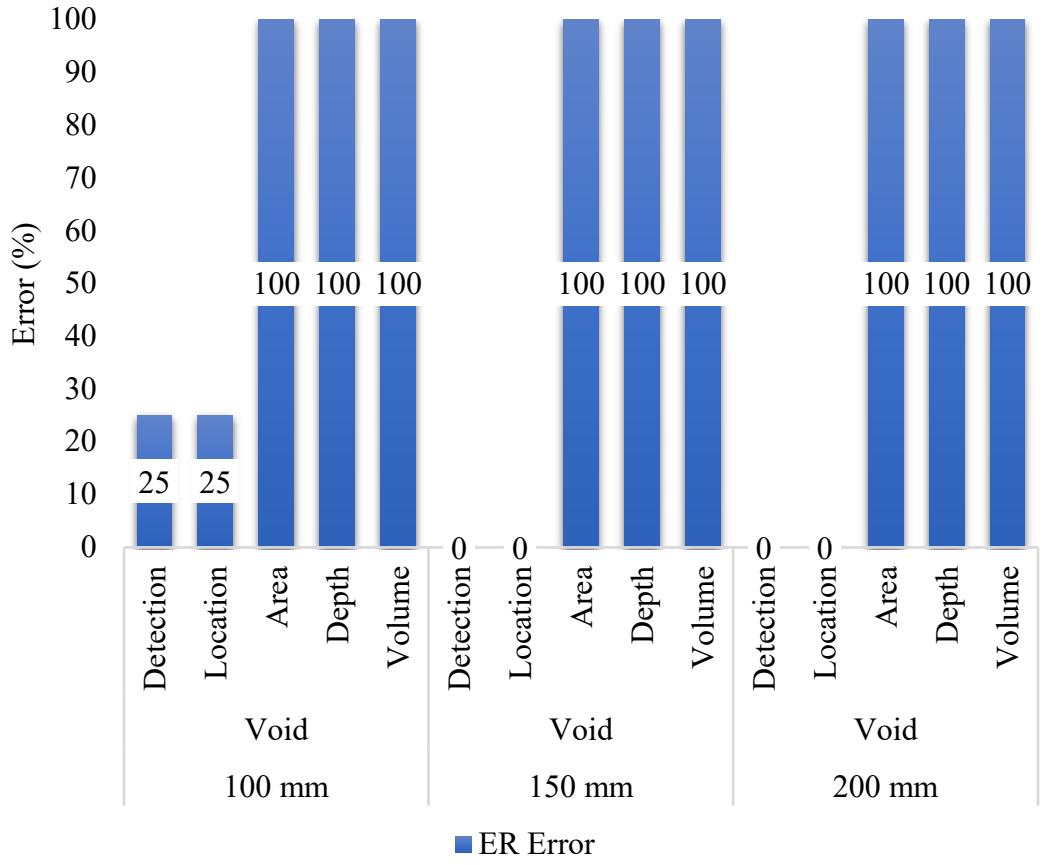

Figure 17: Error of ER in identifying the subsurface damage in reinforced concrete

4. Ultrasonic Pulse Velocity (UPV)

Like ER, significant variation was observed in the pulse velocities even in the control slabs. The control slabs' data was considered as a baseline, and the following threshold values were considered for defect identification,

For 100 mm slabs, values ≤ 2900 m/s = affected area

For 150 mm slabs, values ≤ 2300 m/s = affected area

For 200 mm slabs, values ≤ 2300 m/s = affected area

Figure 29 and Figure 30 are the contour maps for control and slabs with defects, respectively. For control slabs, the UPV values were ranging between 2000-3500 m/s. Similar to other NDT techniques, the defects detected were highlighted with (✓) mark and the undetected defects were highlighted using (X) mark.

From the error plot (Figure 18) it can be observed that UPV was able to locate and detect void and honeycombing with minimum errors. However, UPV was unable to determine the affected area, volume and the depth at which the defect is present. It should be noted that the debonding was not detected by any of the techniques.

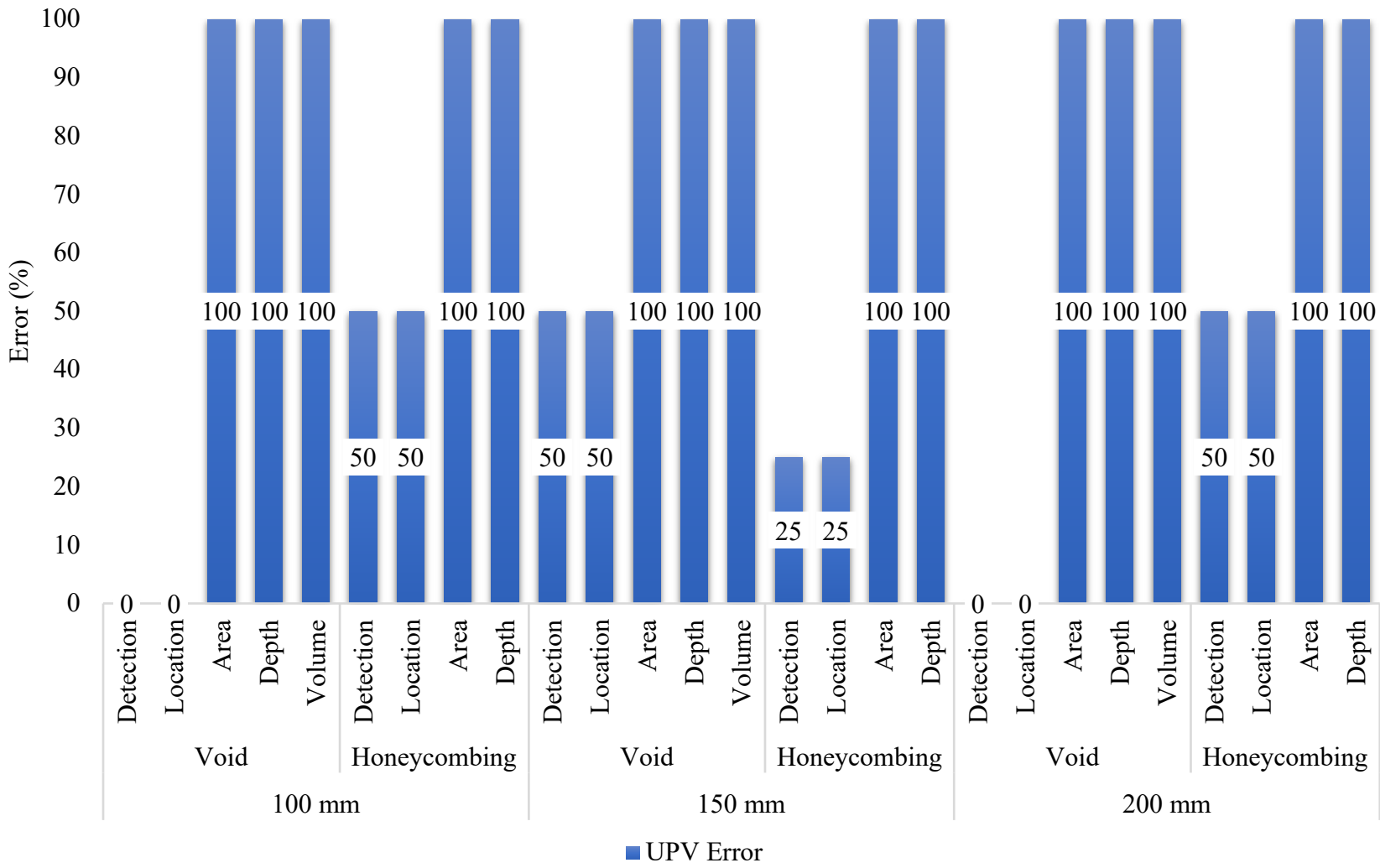

Figure 18: Error of UPV in identifying the subsurface damage in reinforced concrete

5. Half-Cell Potential (HCP)

HCP was used only to determine the corrosion potential and the technique was applied to the slabs with sea salt ingress. In the control slabs, there was not much variation observed in the HCP values. Both maps, for control and slabs with sea salt, are shown in Figure 31 and Figure 32.

The contour map of the slab with sea salt shows the variation in HCP values due to the presence of sea salt in the slabs. It should be noted that the sea salt was added only in the middle third part of the slab. However, due to the rain (wetting and drying cycles), there was diffusion of chloride ions, and as a result, the higher HCP values were recorded outside the middle third portion as well which can be noticed in the map. Due to chloride ions diffusion, it is very difficult to create a boundary while collecting the data. Hence, the values obtained using HCP were assumed to be accurate.

3.5 Refinement of NDT data based on the significance of the defects and their category

In order to refine the NDT data, defects were assigned a significance factor (as shown in Table 7) and each category of the error value was assigned a Logical Sequential Determination Factor (LSDF) as shown in Table 8. Selection of significance factors was made based on its impact on the material (hence change in section properties) and durability of the material as shown in Table 7.

Table 7: Selection of Significance Factors

Type of Defect	**Section Property**	**Durability**	**Overall (Average of Strength and Durability)**
Void	5	3	4
Honeycombing	3	3	3
Debonding	2	3	2.5
Sea salt ingress/Corrosion	1	4	2.5

Where,

5- Very High, 4- High, 3- Medium, 2- Low and 1- Very low

Table 8: Assignment of Significance and LSDF to the defects and error values

Type of Defect	**Significance Factors (SF)**	**LSDF to error values**				
		Detection	**Location**	**Area**	**Depth**	**Volume**
Void	4	5	4	3	2	1
Honeycombing	3	5	4	3	2	1
Debonding	2.5	5	4	3	2	1
Sea salt ingress/corrosion	2.5	5	4	3	2	1

The philosophy of assignment of significance factors originates from the AASHTO Guide Manual (AASHTO, 2011), where depending upon the type and significance of the material defect, the structure is assigned a damage factor. Voids were assigned the highest factor based on the fact that it has the highest impact on the loss of section properties of concrete. Honeycombing and debonding were assigned a section property factor of 3 and 2, respectively. Sea salt/Corrosion was assigned the highest durability factor and lowest section property factor based on the fact that it has a lesser impact on the material strength but higher impact on the durability. Furthermore, based on the fundamentals of the strength of materials, the simulated defects have following incremental order of mass loss and moment of inertia loss.

1. Voids
2. Honeycombing
3. Delamination
4. Sea salt

It should be noted that the impact of material defects on the bridge structure is not only dependent on the size of the defect but also the location, orientation, and other factors.

The 5 different categories (Detection, Location, Area, Depth and Volume) of the defects were assigned LSDF. As the name LSDF suggests, the categories are sequentially dependent in the following order,

1. Detection
2. Location
3. Area
4. Depth
5. Volume

For example, if a defect is not detected by an NDT technique, all the other 4 categories cannot be identified. On the other hand, if it is detected, there might be a possibility to identify the other categories as per the aforementioned order.

Factored error values for each NDT techniques were calculated using equation 3.7,

$$\text{Factored Error } (FE) = \frac{F_i}{SF_k \times LSDF_i} \tag{3.7}$$

$$\text{Combined Factored Error } (CFE) = \frac{(\Sigma_{j=1}^{j=nd}(\Sigma_1^5\,(Min.[FE_i]))}{4} \tag{3.8}$$

Where,

F_i = Defect catagory, SF_k = Significance factor,

$LSDF_i$ = Logical Sequential Determination Factor, i=1 to 5 corresponding to the five categories

Figure 19 is a stacked column chart showing factored error values (calculated using equation 3.7) of all the NDT techniques in identifying subsurface damage in RC slabs. The error values of each NDT technique for all 5 categories are shown in the chart. The determined error values in each category is labeled on the column. As mentioned earlier, no NDT technique could detect the debonding. All five NDT techniques performed well in detection category for voids,

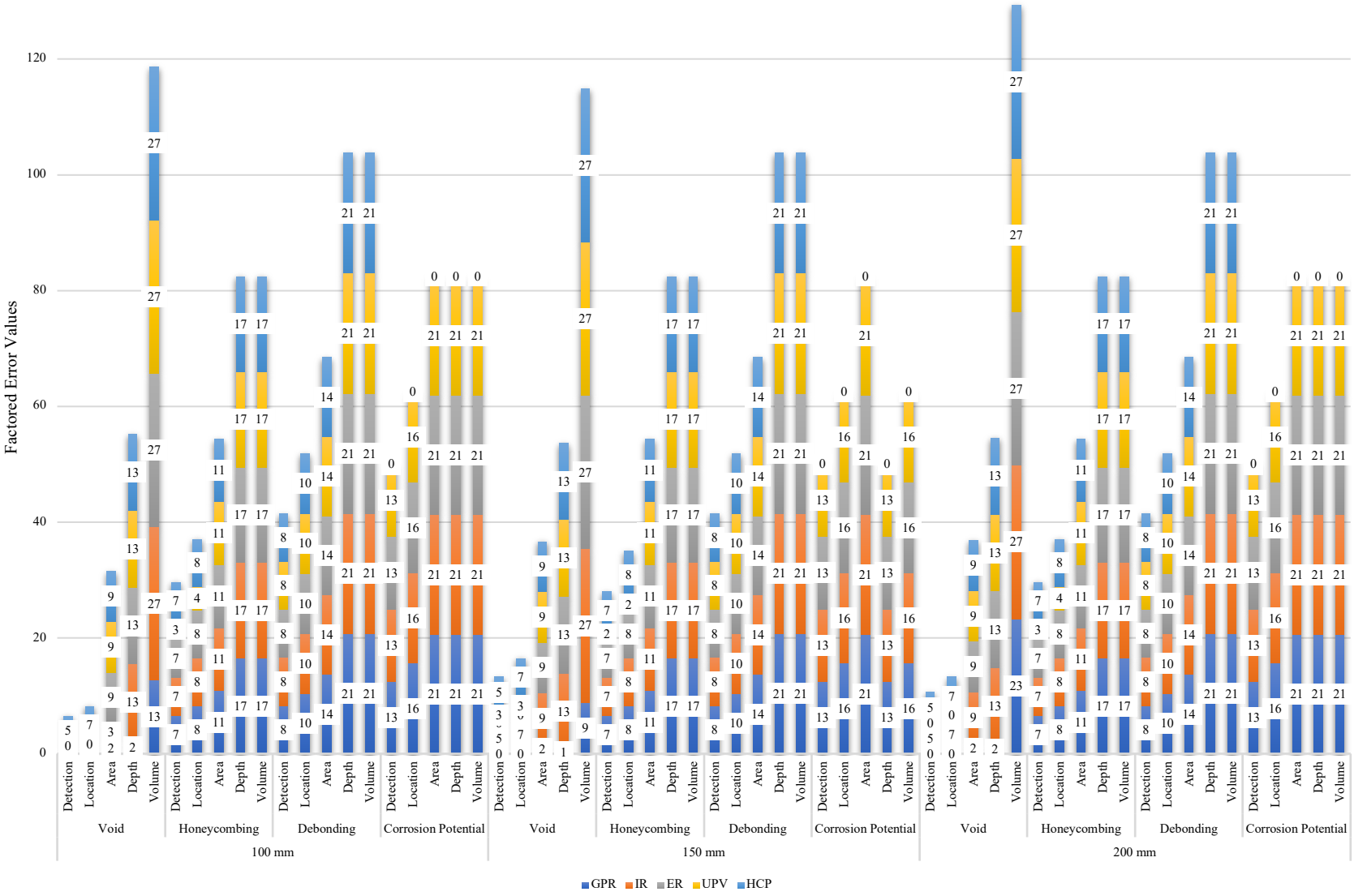

Figure 19: Factored error values of all the NDT techniques in identifying the subsurface damage in reinforced concrete

Honeycombing was detected using only UPV. Voids were detected by all four NDT techniques. HCP demonstrated excellent use for determining corrosion potential as can be noticed from the plots. From the plot, it can be observed that GPR proved to be excellent for detecting voids. Taking the advantage of each of these NDT techniques in detecting a particular type of defect, a set of NDT techniques can be proposed when identifying the subsurface damage in RC. Combination of multiple NDT techniques in identifying subsurface damage increases the accuracy significantly (reduces error) compared to a standalone technique. However, it should be noted that if the NDT techniques are not combined strategically, the reduction in the error values could be insignificant. It can be seen from Figure 20 (calculated using equation 3.8) that the combination of ER, IR, UPV and GPR, ER, HCP have significantly higher factored error values compared to the combination of GPR, UPV, HCP. The error values of the combination of all five NDT techniques were found to be the same as the combination of three NDT techniques- GPR, UPV, and HCP. This is due to the fact that GPR has the lowest error values in detecting voids, UPV has the lowest error values in detecting honeycombing, and HCP has the lowest error values in detecting sea salt.

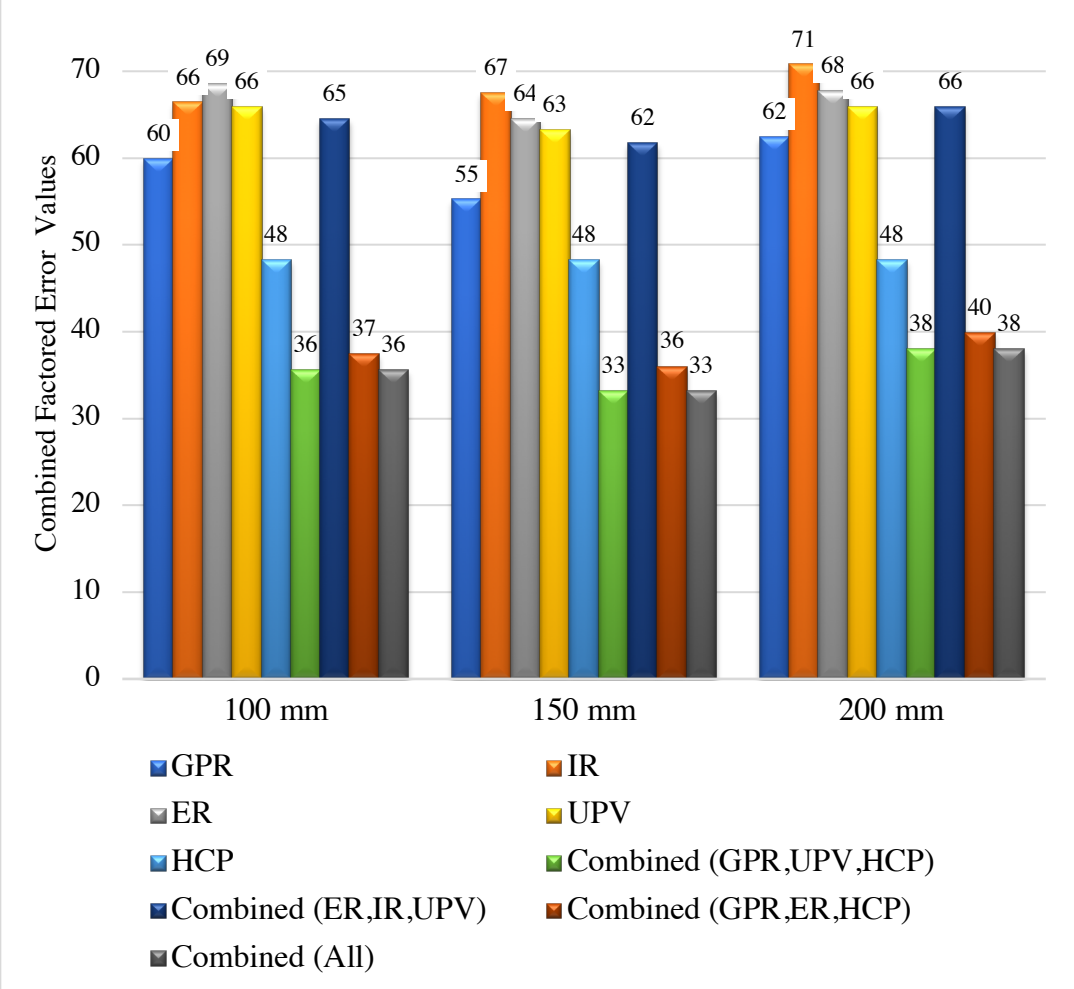

Figure 20: Combined Factored error values of NDT techniques in identifying the subsurface damage in reinforced concrete

3.6 Conclusions

The research work presented uses a total of five NDT techniques to determine their effectiveness in identifying subsurface damage in RC. This research investigates the performance of NDT techniques in identifying a total of four defects embedded in the RC slabs. It should be noted that the present research has only considered subsurface damage. All other major surface defects such as spalling, discoloration, efflorescence, and cracking were not considered in this study. To determine the performance of each NDT technique, more than 300 data points were considered. From this research, following conclusions can be drawn,

1. As suggested in the literature, a single NDT technique is not enough to detect all the defects. For instance, GPR, UPV, and HCP when used individually, the average (considering all the thicknesses) factored percentage errors were 60, 66 and 48 respectively. However, when all three techniques were applied together, the percentage error dropped down to 36.
2. GPR was found to be the most accurate for detecting voids, UPV for Honeycombing, and HCP for corrosion potential.
3. None of the NDT techniques could detect the simulated delamination.
4. The defect detection capability of IRT was found to be highly dependent on the depth of the defect and environmental factors.
5. The data collected by ER and UPV had a very high coefficient of variation compared to the other 3 techniques.

3A: Data article- Two-Dimensional Non-Destructive Testing data maps for Reinforced Concrete slabs with simulated damage

Article Link : https://doi.org/10.1016/j.dib.2019.104127

Harsh Rathod[1] and Dr. Rishi Gupta[2]

[1]PhD Research Scholar, Department of Civil Engineering, University of Victoria, Victoria, BC, Canada, 778-350-7779, hmrathod@uvic.ca
[2]Associate Professor, Department of Civil Engineering, University of Victoria, Victoria, BC, Canada, 250-721-7033, guptar@uvic.ca

Note: These data maps are adapted in part from published work (Rathod et al., 2019b) in Data in Brief, Elsevier, with permission where appropriate. Journal of Construction and Building Materials publishes all the supplementary material as an article in the Data in Brief. These data maps are an integral part of Rathod et al., 2019a. Field inspectors and NDT practitioners will be able to use these data maps to interpret the NDT results accurately.

3.1a Abstract

This research presents the use of a total of five NDT techniques and their combination to detect and quantify subsurface simulated defects in Reinforced Concrete Slabs. The NDT techniques were applied on a total of nine 1800 mm × 460 mm reinforced concrete slabs with varying thicknesses of 100 mm, 150 mm and 200 mm. Contour data maps from each technique were prepared. This Data article presents the Non-Destructive Testing Techniques' specifications, experimental set-up and converted 2-Dimensional NDT data maps for reinforced concrete slabs with simulated damage. The experimental research shows that combining multiple techniques together in evaluating the defects give significantly lower error and higher accuracy compared to that from a standalone test. For more details on the accuracy model of the NDT techniques, refer to the full-length article entitled "Subsurface simulated damage detection using Non-Destructive Testing Techniques in reinforced concrete slabs."
https://doi.org/10.1016/j.conbuildmat.2019.04.223

3.2a Value of the data

- The data maps presented here are of control (no defects) reinforced concrete slabs and slabs with simulated subsurface damage. The maps highlight the comparison of different NDT techniques in detecting and quantifying the damage.
- The maps allow NDT practitioner in the field to identify potential damage by correctly interpreting the NDT data.
- This data maps will help the researcher to develop similar experiments with different simulated damage to determine NDT techniques' capability in detecting and quantifying subsurface damage.

- The work presented here is a foundation to interpret NDT techniques' data correctly as it compares the individual data points of slabs with no defects and the slabs with simulated damage.

3.3a Data

Each data point collected from Reinforced concrete slabs with simulated damage and control slabs were converted into either intensity maps or contour maps to determine the performance of NDT techniques. Table 9 below shows the experimental setup and details related to data collection.

Table 9: NDT techniques' specifications and experimental setup

NDT technique	Equipment	Company	Specification	Experimental Setup
GPR	Structure Scan Mini	GSSI	Max Depth = 50 cm Antenna Frequency = 2600 MHz	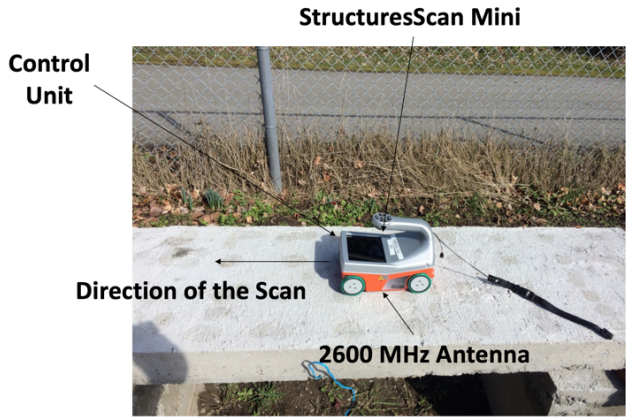
IRT	E60	FLIR	IR Resolution= 320 x 240 pixels Spatial Resolution =1.36 mrad Thermal Sensitivity = <0.05 °C	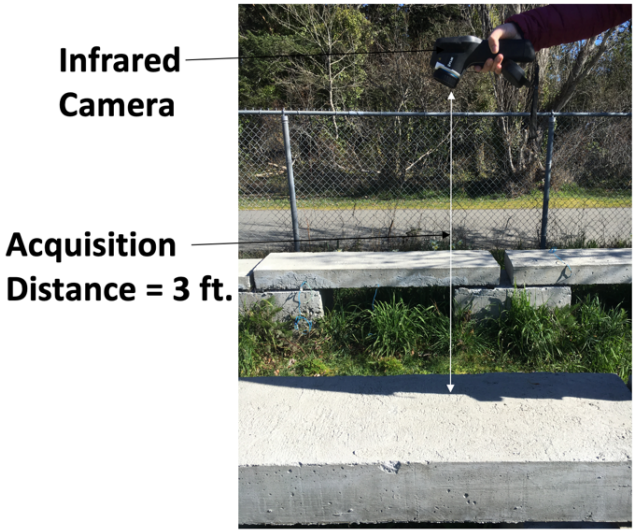

Table 9: NDT techniques' specifications and experimental setup (Continued)

NDT technique	Equipment	Company	Specification	Experimental Setup
ER	Resipod	Proceq	Frequency = 40 Hz Resolution (nominal current 200µA) = ±0.2 kΩcm or ±1% (whichever is greater) Resolution (nominal current 50µA) = ±0.3 kΩcm or ±2% (whichever is greater) Resolution (nominal current <50µA) = ±2 kΩcm or ±5% (whichever is greater)	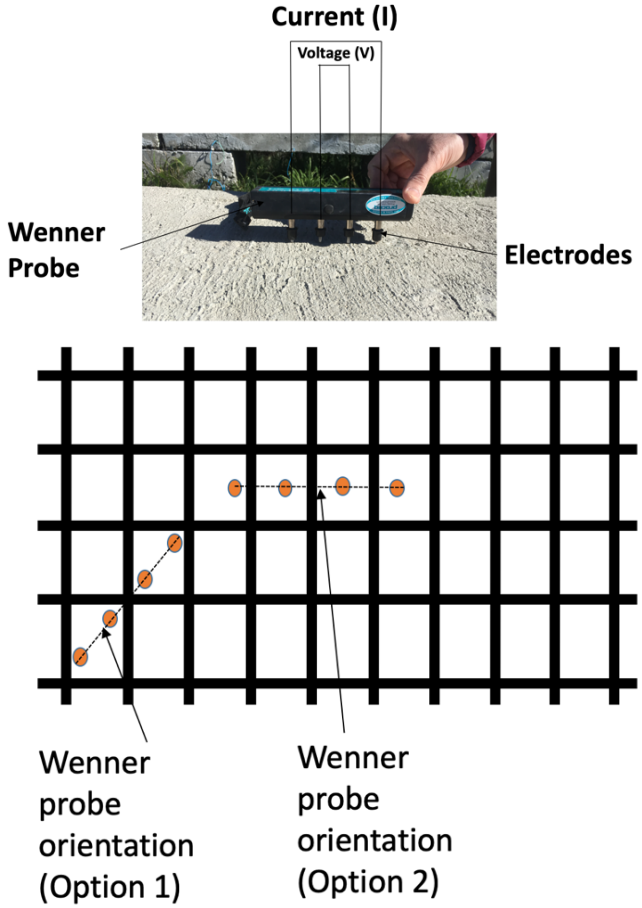

Table 9: NDT techniques' specifications and experimental setup (Continued)

NDT technique	Equipment	Company	Specification	Experimental Setup
UPV	Two Transducer Probes	proceq	Resolution = 0.1 µs Bandwith =54kHz	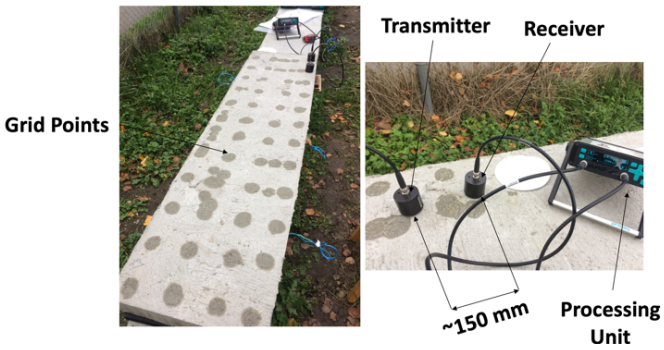
HCP	Single Point Probe	Tinker and Rasor	Model – 6B Type= Copper-Copper Sulphate	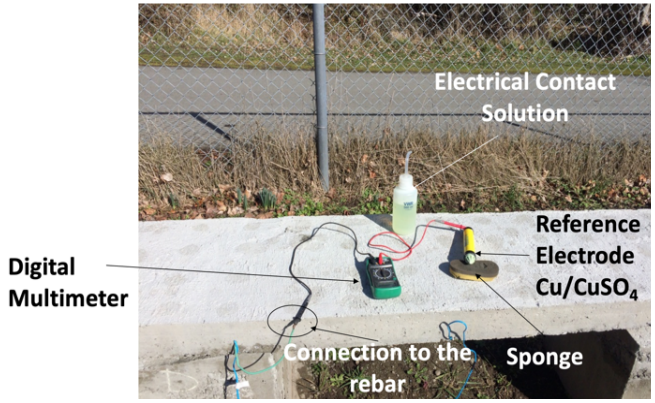

The experimental set up is shown in Figure 21, where all nine test specimens were placed together on 1.5 feet high concrete blocks to access the slabs from the bottom as well if required in the future. Figure 22, Figure 23, Figure 24 are data maps of Ground Penetrating Radar.

3.4a Figures

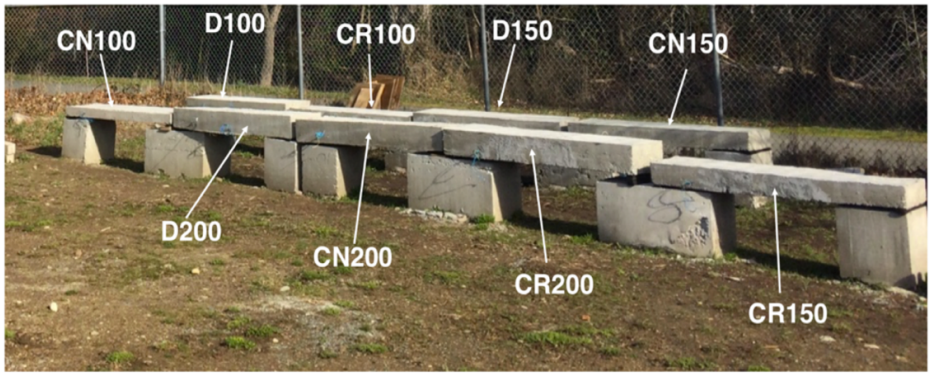

CN = Control
D= with induced defects
CR = with induced chloride ions

100 = 100 mm slab thickness
150 = 150 mm slab thickness
200 = 200 mm slab thickness

Figure 21: Experimental setup of the nine RC test specimens

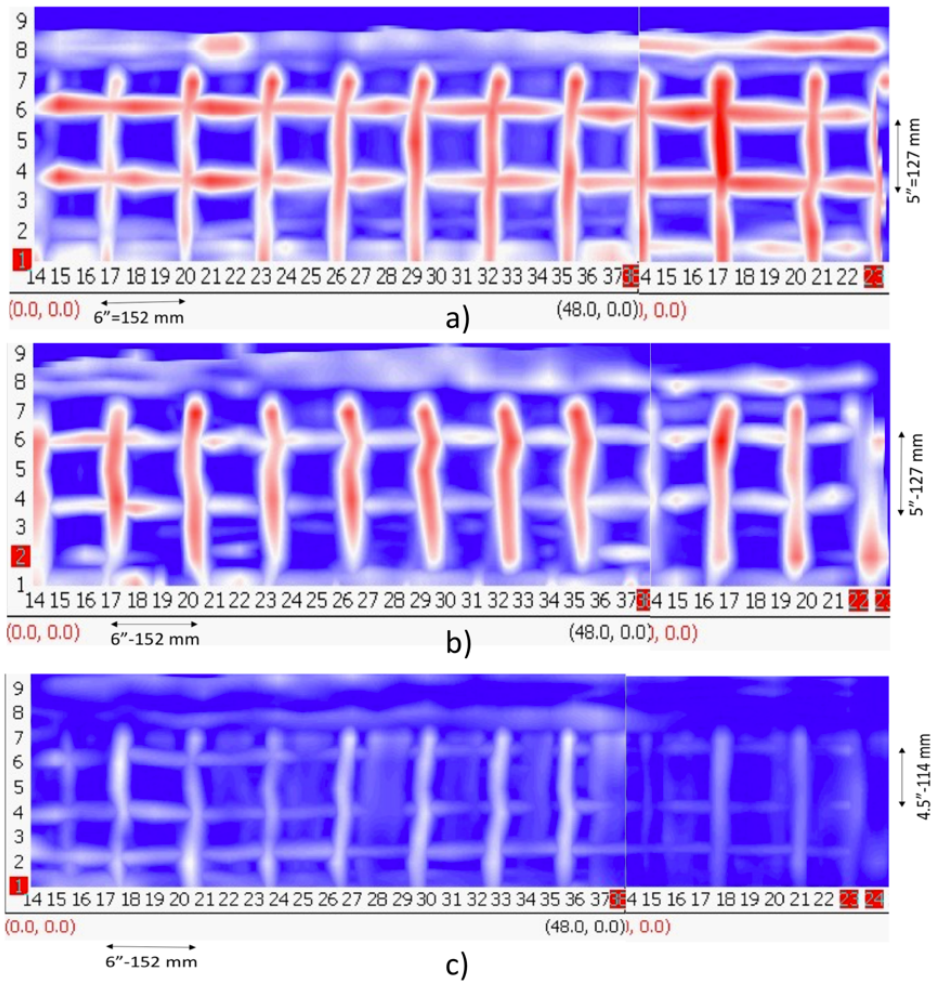

Figure 22: GPR Maps – control slabs - a) 100 mm, b) 150 mm, and c) 200 mm

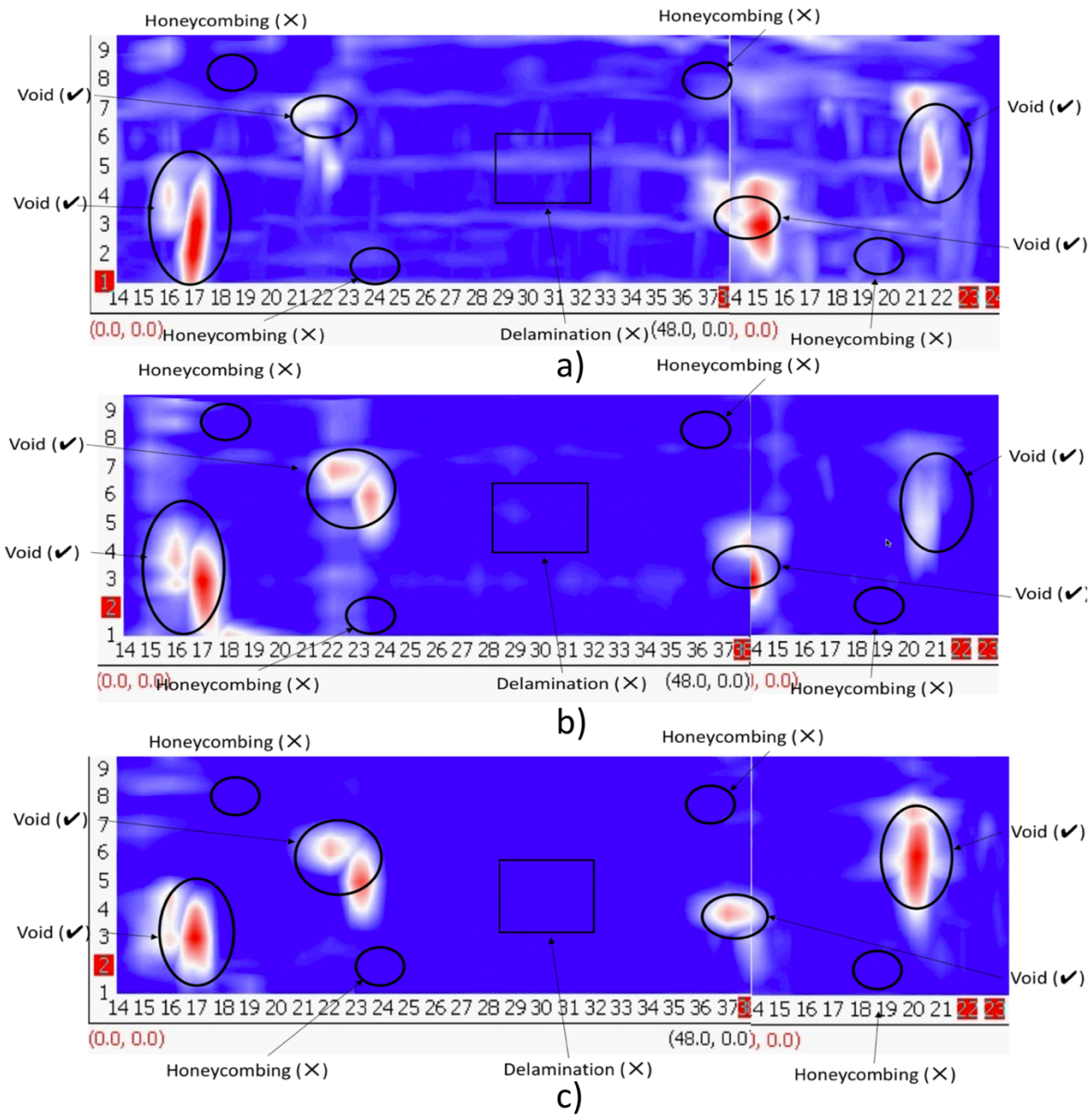

Figure 23: GPR Maps – slabs with subsurface defects - a) 100 mm, b) 150 mm, and c) 200 mm

Figure 25 is an Infrared Thermograph captured to identify the temperature difference between the embedded voids and surrounding sound concrete. Figure 26 shows the processed map to compute the area of voids.

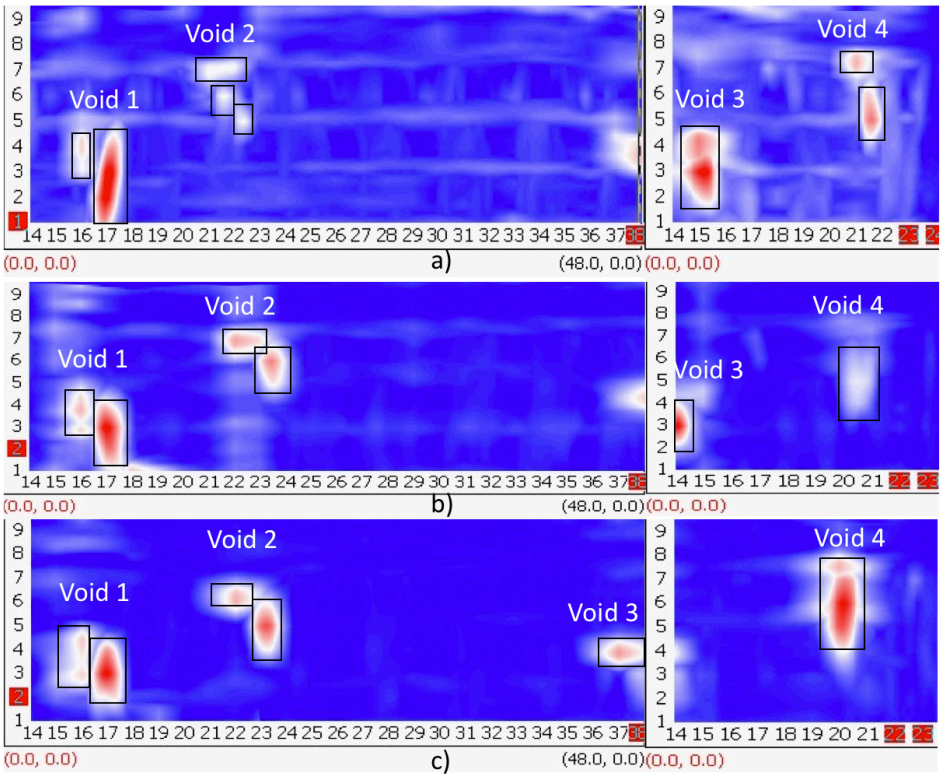

Figure 24: GPR- Area, Depth and Volume Accuracy Computation: a) 100 mm, b) 150 mm, and c) 200 mm

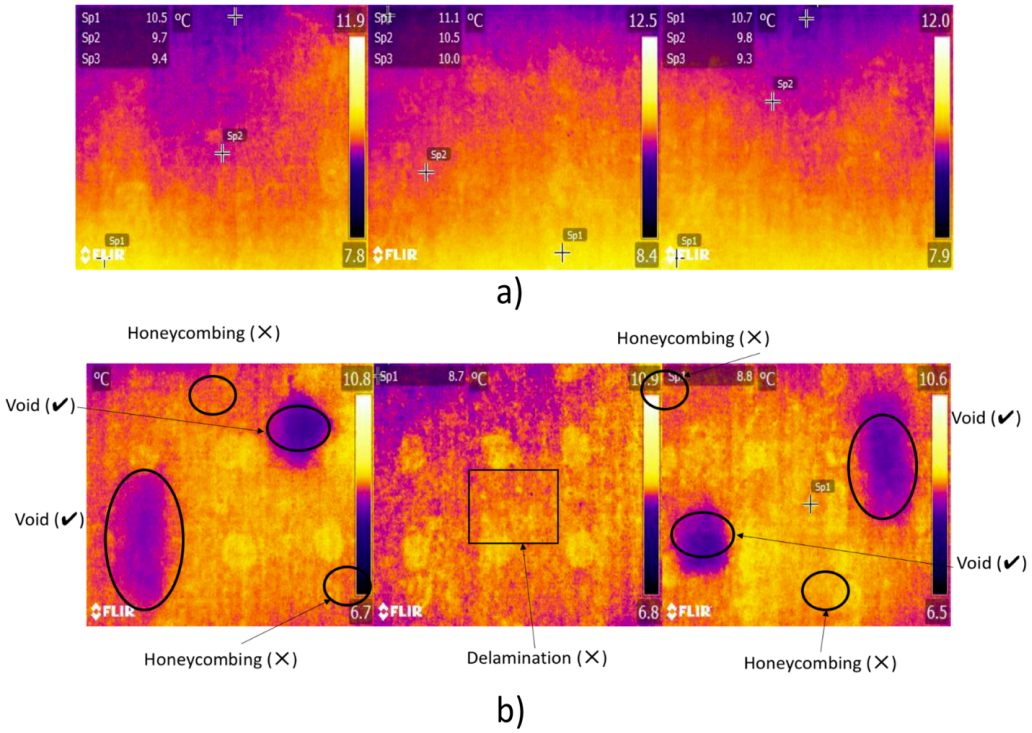

Figure 25: IR Thermographs – control and slab with defects -100 mm

Figure 26: IRT- Area accuracy computation:100 mm slab using MATLAB Software

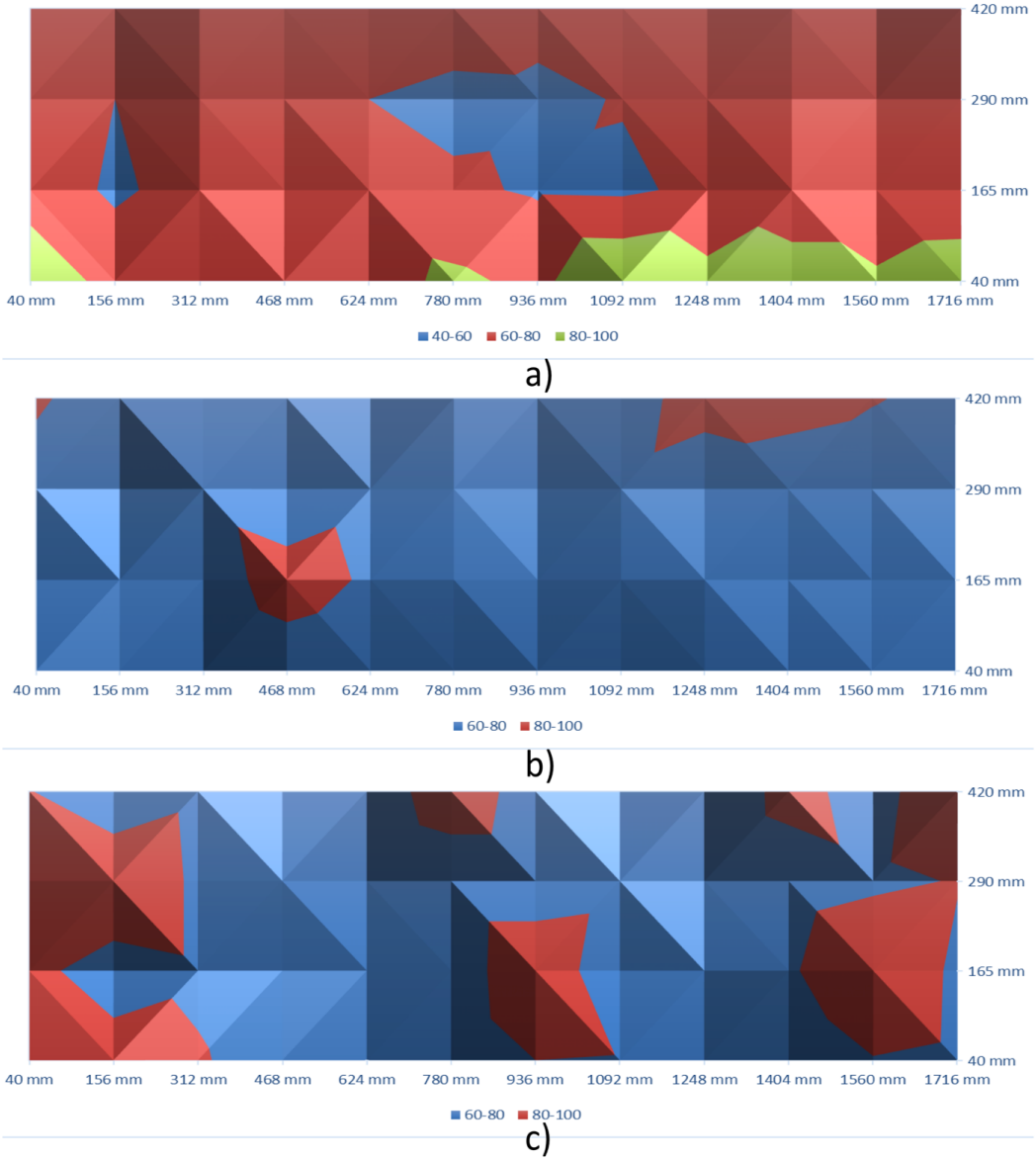

Figure 27: ER Contour Maps - control slabs - a) 100 mm, b) 150 mm, and c) 200 mm

Figure 27 and Figure 28 are Electrical resistivity contour maps.

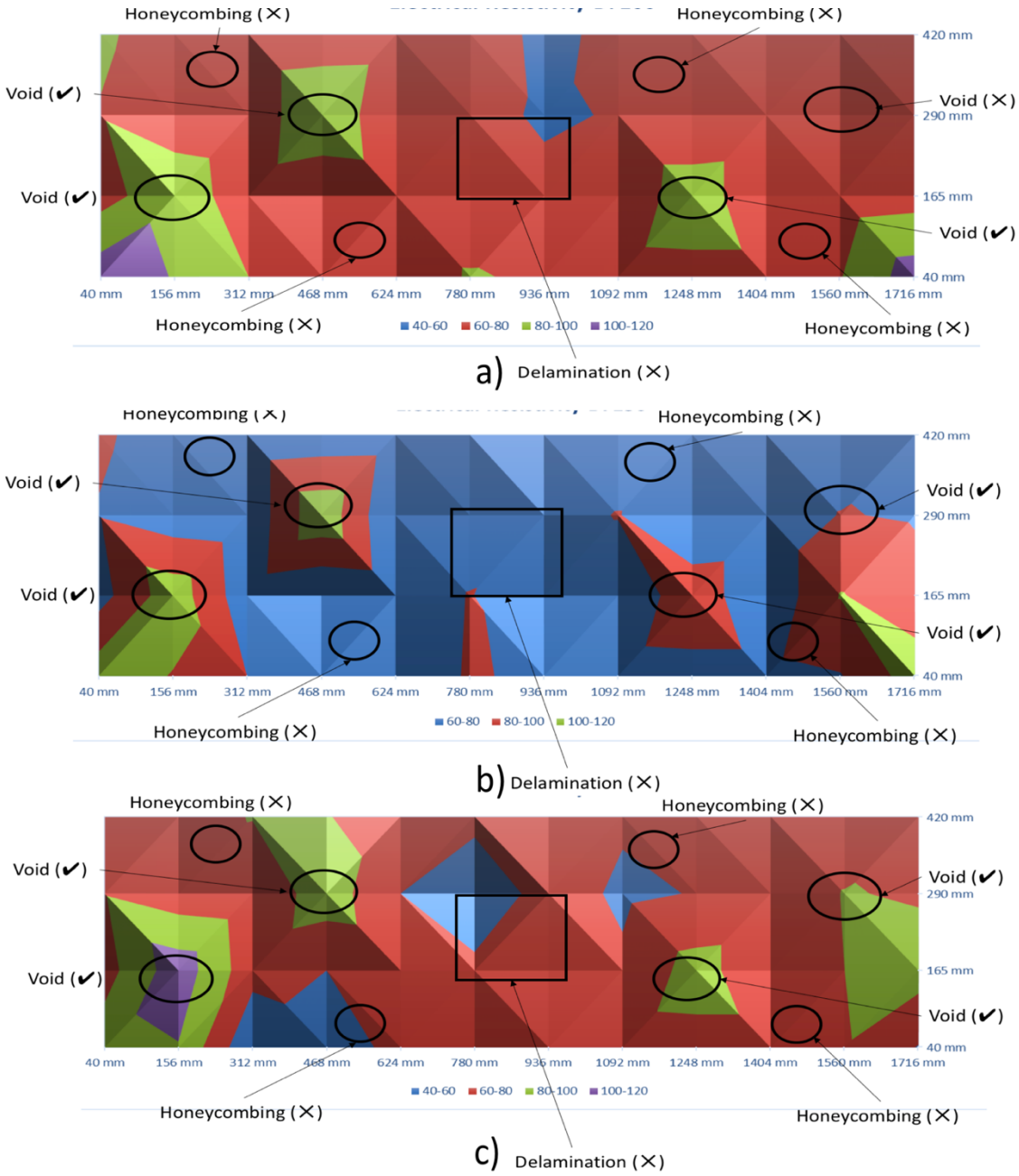

Figure 28: ER Contour Maps- slabs with subsurface defects - a) 100 mm, b) 150 mm, and c) 200 mm

Figure 29 and Figure 30 show the contour maps produced using the data obtained from Ultrasonic Pulse Velocity. These maps are for 100 mm, 150 mm and 200 mm slabs (both control and with defects).

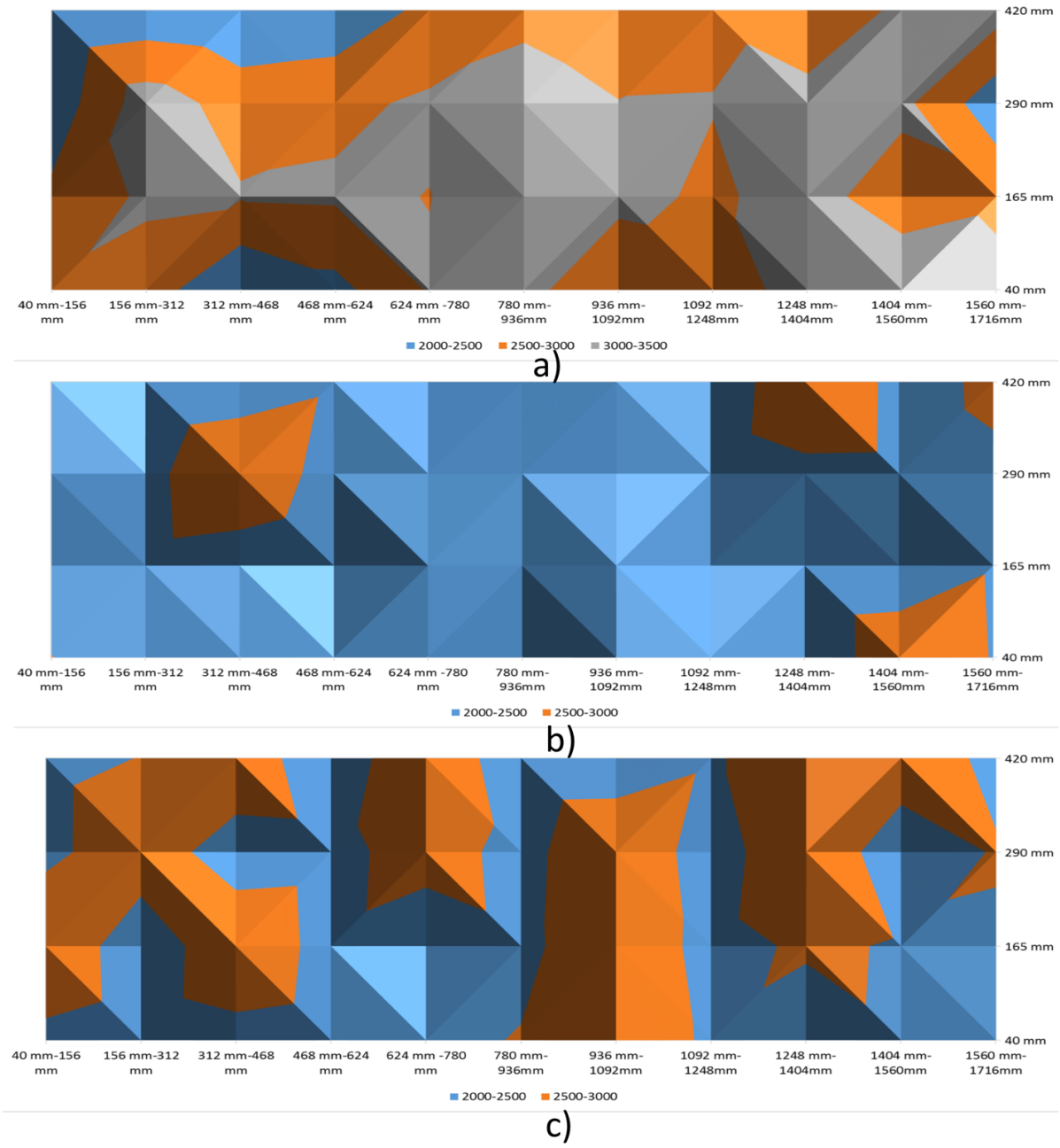

Figure 29: Ultrasonic Pulse Velocity-control slabs - a) 100 mm, b) 150 mm, and c) 200 mm

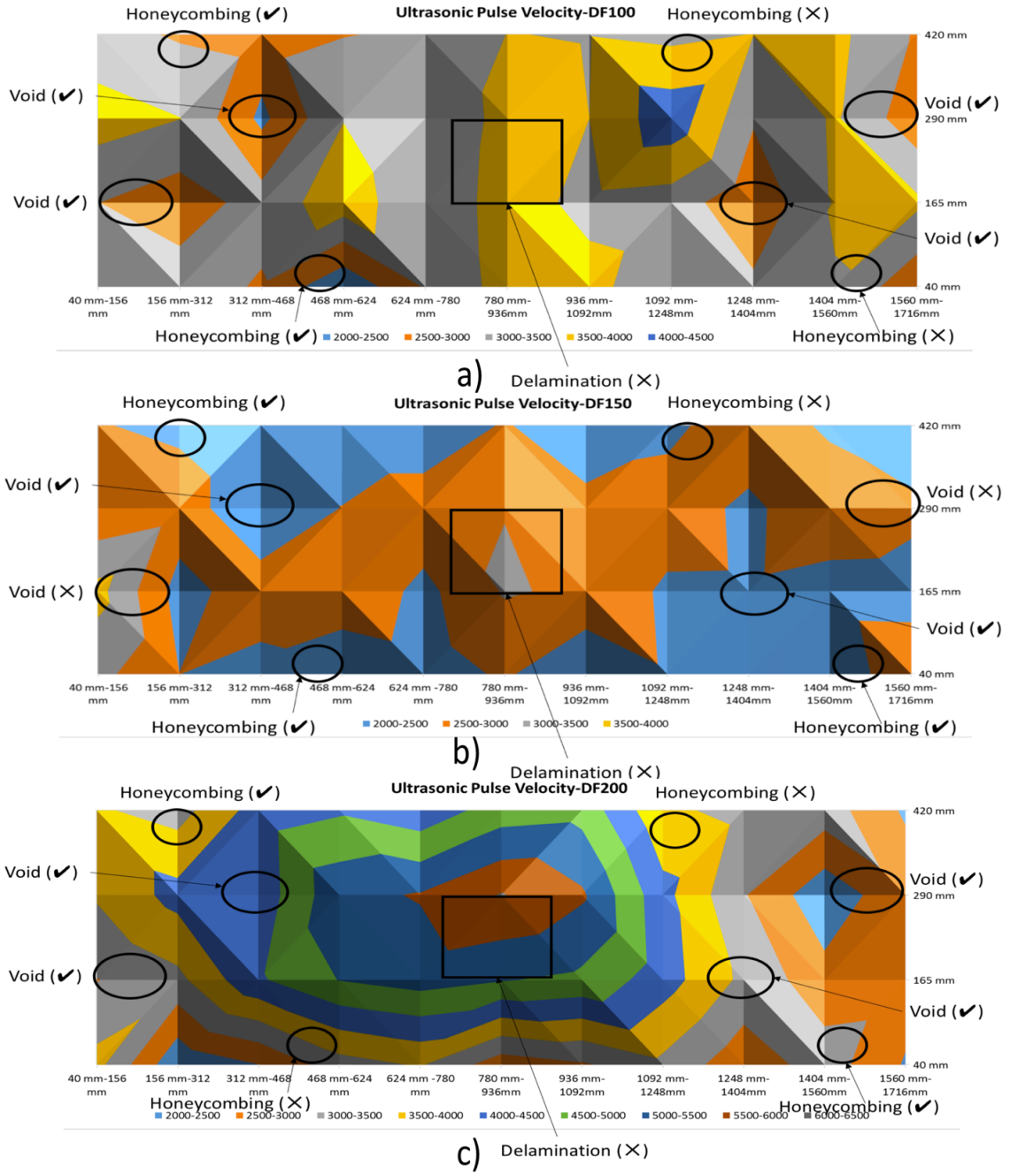

Figure 30: Ultrasonic Pulse Velocity-slabs with defects - a) 100 mm, b) 150 mm, and c) 200 mm

Figure 31 and Figure 32 show the contour maps produced using the data obtained from Half-Cell Potential Technique. These maps are for 100 mm, 150 mm and 200 mm slabs (both control and with defects).

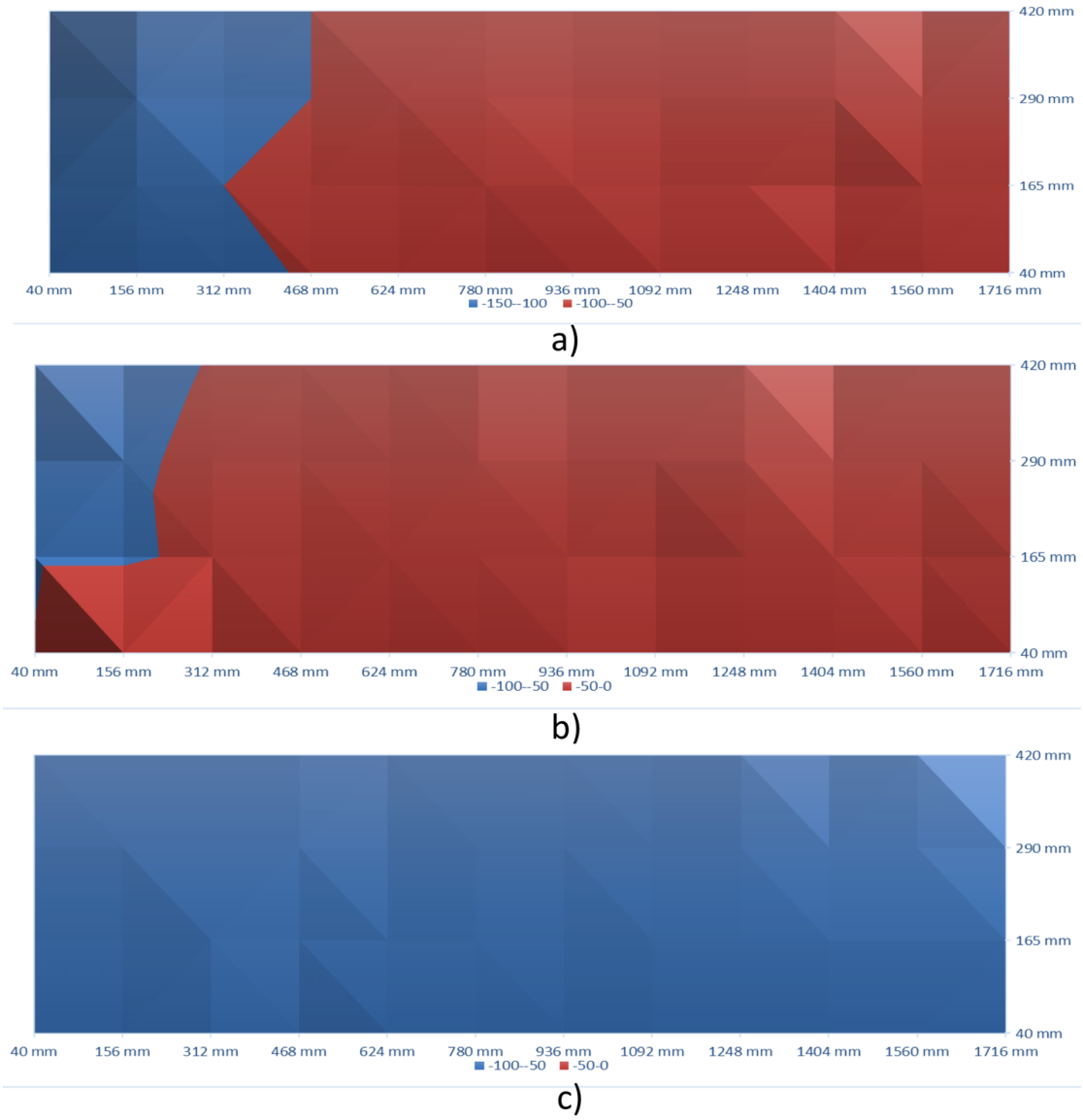

Figure 31: Half-Cell Potential - control slabs - a) 100 mm, b) 150 mm, and c) 200 mm

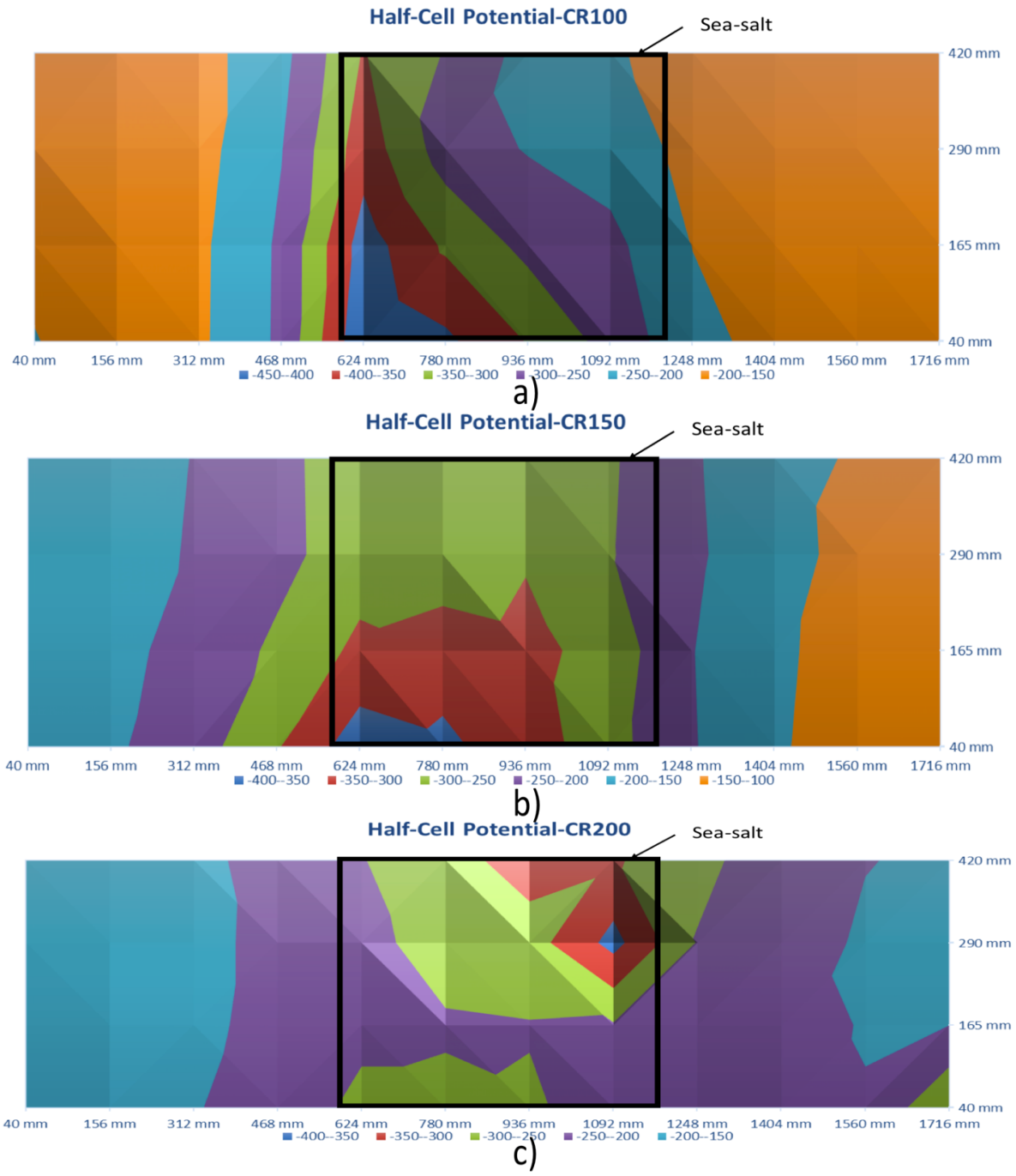

Figure 32: Half-Cell Potential-corrosion slabs - a) 100 mm, b) 150 mm, and c) 200 mm

3B: Applicability of GPR and a rebar detector to obtain Rebar information of existing concrete structures

Article Link : https://doi.org/10.1016/j.cscm.2019.e00240

Harsh Rathod[1], Scott Debeck[2], Rishi Gupta[3], Brian Chow[4]

[1]PhD Research Scholar, Department of Civil Engineering, University of Victoria, Victoria, BC, Canada, Email: hmrathod@uvic.ca

[2]Resource Technologist, Engineering Branch -Timber Operations, Pricing and First Nations Division, Ministry of Forests, Lands, Natural Resource Operations and Rural Development, Victoria, BC, Canada

[3]Associate Professor, Department of Civil Engineering, University of Victoria, Victoria BC, Canada

[4] Chief Engineer, Engineering Branch -Timber Operations, Pricing and First Nations Division, Ministry of Forests, Lands, Natural Resource Operations and Rural Development, Victoria, BC, Canada

Note: This section is adapted in part from published work (Rathod et al., 2019c) in Elsevier, Journal of Case Studies in Construction Materials (Open Access Journal) with permission where appropriate. In this section, GPR and cover meter are elaborated further to identify their applicability in determining rebar characteristics. For this, an accuracy model of GPR and cover meter is developed.

3.1b Abstract

Much of Canada's existing infrastructure was constructed during the 1950s, 1960s, and 1970s. These include all transportation infrastructures such as bridges, highways, tunnels, etc. It is important to know the condition of these aging infrastructures in terms of their load carrying the capacity to ensure their safety and serviceability. There are several old reinforced concrete slab bridges within the network of Ministry of Forests in B.C. Canada that has unknown rebar spacing, cover, and diameter. This research paper discusses the application of Ground Penetrating Radar (GPR) and a Rebar detector in obtaining valuable information about rebar diameter, spacing, and cover depth required to determine the structural capacity (load rating) of bridge decks. For this, GPR and the rebar detector have been applied on an existing bridge deck, a precast bridge girder and a reinforced concrete test slab panel available in the materials lab at the Facility for Innovative Materials and Infrastructure Monitoring (FIMIM) at the University of Victoria (UVic). To assess the applicability of GPR and Profoscope (Rebar Detector) in obtaining rebar information, the results obtained using both the techniques were compared in terms of their errors in determining all three parameters of rebar; diameter, spacing, and cover depth. The results were validated by measuring the actual diameter, spacing and cover depth of the rebar in the reinforced concrete test slab available in the lab at UVic.

3.2b Introduction

A large part of Canada's infrastructure was constructed between 1950-1970. This includes water mains & Sewers but also includes bridges and overpasses. In Canada bridges have a mean service life estimated at 43.3 years and in 2007, they passed 57% of

their useful life already (Gagon et al., 2008). It is important to know the condition of these aging infrastructures in terms of residual load carrying capacity to ensure the safety and serviceability of the structures and people using them. The Ministry of Forests, Lands, Natural Resource Operations and Rural Development (MFLNRO) currently maintains over 6000 bridge structures across British Columbia (Kashif Ur Rehman et al., 2016). There are several old bridges under the network of MFLNRO of British Columbia that have unknown rebar spacing, cover and diameter due to the non-availability of their structural drawings. Information on rebar diameter, spacing, and cover depth is essential in determining the load rating (Structural Capacity) of bridge decks. The present research uses two different non-destructive testing techniques to determine rebar diameter, spacing, and cover depth in reinforced concrete sections. The principle of both the techniques along with the previous research work is described here in this section separately for ease of reading.

Ground Penetrating Radar (GPR)

GPR's popularity is due to its advantages over the other techniques. Benedetto et al., 2017 describes the advantages of GPR and the major GPR strengths for its use in the field of civil engineering. These include the non-destructive nature, lower costs compared to the traditional methods, and higher reliability in the measurement.

The most common and wide use of GPR for concrete analysis has been found for mapping delamination in Reinforced Concrete (RC), detecting pipes, finding steel rebar and identifying the thickness of pavements (Zhao et al., 2017 and Ayela-Cabrera et al., 2017). Apart from the identification of the defects in RC, GPR is also being used for verifying design plans by mapping the true rebar grid layout and prestressing tendons (Cruz et al., 2010).

Although many researchers have published their work related to identifying rebar diameter (Mechbal et al., 2010, Zanzi et al., 2013, and Utsi et al., 2004), the signal processing techniques they proposed, have been proven to be difficult and time-consuming.

It should be noted that GPR does not directly measure the diameter of rebar, cable or conduit (Concrete Handbook-GSSI, 2015). GPR when used with the larger diameter of rebar, can produce a stronger reflection of the radar wave. Due to signal wavelength, any object under 2" (5 cm) in diameter is a "dot" with no visible size (Concrete Handbook-GSSI, 2015). It should be noted that the reflection strength depends on several factors such as depth of the slab, area of slab and properties of concrete and steel. Thus, it is very difficult to obtain an accurate measurement of the diameter of rebar in concrete.

Rudimentary estimations of rebar diameter can be made, if the rebar is stacked perpendicularly, by subtracting the cover of the top rebar from the cover of the bottom rebar. This method can be accurate up to 3 mm, but can only estimate the top rebar diameter (Hong et al., 2017). The present research uses this methodology. However, this is not helpful in most Ministry applications, as the top rebar is typically shear stirrups which are almost exclusively 10M (11.3 mm) rebar.

The GPR equipment typically consists of two antennas; transmitter and receiver antenna, a radar control unit, data acquisition system and display devices. GPR technique detects the changes in electromagnetic properties of the material from the reflected Electro-Magnetic (EM) waves that are sent into the material's subsurface. It uses high-frequency-pulsed EM waves (from 10 to 3000 MHz) (often called radar waves) to acquire subsurface information. The present research uses a GPR (Model Name- Structures Scan Mini) that

utilizes 2600 MHz electromagnetic waves transmission antenna to detect the subsurface features.

Post Processing of GPR data and Development of 3-Dimensional Maps

2-Dimensional line scans collected by Structures Scan Mini is post-processed using the control unit's post-processing software. The post-processing includes time zero correction (set ground surface), background removal (remove horizontal banding), bandpass filtering (remove high/low-frequency noise), and Range Gain (normalize gain curve across depth range). In-order to convert 2D profiles into 3D maps, a 3-dimensional mapping function integrated within the Structure Scan Mini's control unit was used in this research. This function performs a fairly linear interpolation between adjacent profiles on a grid to map subsurface features as a function of the depth of the slab. The 3D gridding process itself does not introduce significant errors. The major source of errors in 3D datasets is inherited from data collection, such as incorrect distance encoder calibration, the position of the antenna on starting/ending grid baselines, improperly configured survey grid, local topographic irregularities, and other variables (Concrete Handbook-GSSI, 2015).

It should be noted that one of the most important elements of post-processing of GPR data is calibration of depth. Calibration of depth is achieved using a process/algorithm called migration. Structure Scan Mini uses Kirchoff's migration algorithm (Yao et al., 2012) to remove hyperbolic tails by collapsing them into dots representing the actual targets (in this case, rebar). Also, data with hyperbolic reflections need to be migrated in order to achieve a quality 3D display (Concrete Handbook-GSSI, 2015). The migration process is very useful (it reduces clutter in the image) when identifying rebar that is close to each other in a concrete slab.

Rebar detector (Profoscope)

Unlike GPR, the Profoscope uses the magnetic field to identify rebar layout in concrete. It uses electromagnetic pulse induction technology (Handlon et al., 2000) to detect metallic object beneath the concrete surface. As can be seen in Figure 33, the pulse induction technology has coils that are charged using the current pulses to generate a magnetic field around the electrically nonconductive concrete surface. The magnetic field generated by coils is opposite in the direction which creates the difference in voltage that can be used for the measurement. Using signal processing techniques, the rebar detector determines the various characteristics such as cover depth, diameter, and spacing of rebar.

There are several research articles that describe the effectiveness of a rebar detector for its use in detecting rebar embedded in RC sections (Fan et al., 2013, Delgado et al., 2016, Ahmedov et al., 2015 and Prabakar et al., 2007). This particular paper describes the use of a Profoscope from Proceq, in determining rebar diameter, cover depth, and spacing in concrete sections. It is suggested that before testing, the Profoscope must be calibrated, and all metal must be removed from the area. The calibration of Profoscope is performed on site right after turning on the equipment using the test jig provided by the supplier. All the metallic objects (rings, watches, keys, toolbox, etc.) are kept at least 3 m away from the calibration setup. When rebar is passed under a Profoscope, crosshairs travel across the screen. When the crosshairs are in the middle of the screen, a light illuminates to indicate the Profoscope is over a target. The nature of this technique makes it difficult to know what the orientation of the rebar is. A method to determine the orientation of the rebar is to move

the Profoscope around this target, until the target light remains constant, meaning the rebar is parallel to the line of movement. This method can be difficult to perform if there is a high concentration of rebar in the slab. Rebar diameter can be accurately measured when the rebar is spaced 150 mm apart, and the cover is less than 65 mm (Profoscope Operating Instructions, 2017). Measuring range and standard resolution of Profoscope depends on the rebar diameter. The charts showing the effects of rebar diameter on measuring range and standard resolution are given in (Profoscope Operating Instructions, 2017).

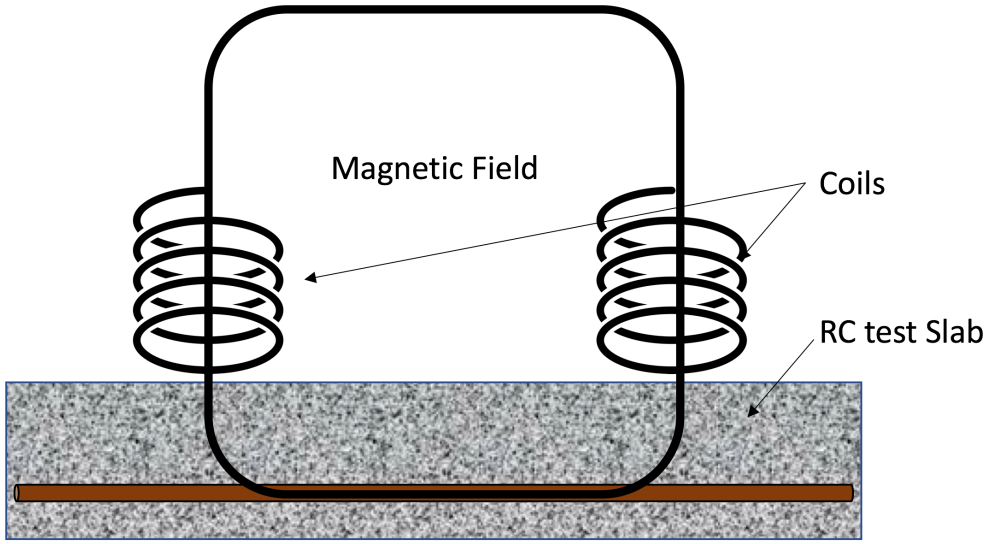

Figure 33: Measurement Principle of Profoscope (Modified from the Profoscope Operating Instructions, 2017)

3.3b Research Significance

The present research demonstrates the applicability of the Profoscope and GPR to determine rebar information such as diameter, cover, and spacing in existing RC bridge decks. Past research shows that the Profoscope and GPR both could be used to detect and characterize the features of subsurface metallic objects in concrete sections. However, research conducted in the past on comparison of both the methods in terms of accuracy in determining rebar information is very limited. This information would be very valuable to the infrastructure owners (e.g. MFLNRO) in making necessary decisions for managing their structures. The paper also highlights the key challenges of both the techniques that were faced during the experiments.

3.4b Experimental Investigation

Experimental work was carried out at three different site locations: a) Stocking Creek Bridge Site (SI-3006A) in Duncan, BC, Canada b) Surespan Structures precast facility and c) Civil Engineering Materials lab at University of Victoria. GPR and Profoscope were applied to three different RC sections at different site locations. A smaller area of the slab examined at Surespan was measured due to time constraints, which means fewer assumptions can be made for the rest of the section of the bridge. It should be noted that during the experiments conducted at the bridge site and at the precast site, the weather

conditions included cloudy skies with a few showers and ambient air temperature of about 7 ºC. The experiments were conducted right after the showers. At the Civil Engineering Materials Lab, the test slabs were in a controlled environment (ambient air temperature 15 ºC) isolated from the outside weather. The procedure of conducted non-destructive testing at all three locations is described here separately.

Reinforced concrete bridge deck at site SI-3006A

The reinforced concrete precast bridge deck at Site SI-3006A (Figure 34) located at 10675 S Watts Rd. Ladysmith, BC, Canada (48.947040, -123.785428) was assessed from the bottom side using GPR and Profoscope. Record drawings were not reviewed before proceeding with experiments to simulate assessing a bridge with unknown reinforcement. To perform the Profoscope and GPR tests, a 2'x 2' (610 mm x 610 mm) grid (169 data points) was drawn on the bottom side of the bridge deck. The location of the grid was measured relative to the edge of the structure for reference.

a) b)

Figure 34: GPR and Profoscope tests on the bottom of the bridge deck slab; a) Test grid, b) Test Site SI-3006A

To calibrate the Profoscope, all metal was removed from the testing area. The diameter input of the Profoscope was estimated to be 20 mm, as the rebar diameter was not known. No spacing adjustment was made, as the spacing of the rebar was a parameter to obtain from the test. To detect lateral rebar, the Profoscope was placed on the y-axis of the grid and moved in the positive x-direction until the Profoscope indicated the location of rebar with a constant beeping sound with a red light. The coordinates, cover, and diameter of the rebar were marked on the grid. The Profoscope was then moved in the x-direction until all lateral rebar which was located on the x-axis within the grid were identified. This process was done a total of two times, increasing the y-value each time. To detect transverse rebar (rebar running in the x-direction), a similar methodology was used. GPR data were collected using the same 2'x 2' (610 mm x 610 mm) grid used previously. The GPR was run along each of the grid lines, totaling 26 different passes with the GPR (13 vertical lines, 13 horizontal lines).

Precast bridge girder at Surespan structures

The procedure undertaken for performing non-destructive testing at Surespan Structures was similar to the procedure prepared for the testing at the bridge site. The girder tested at Surespan Structures was a 12 m concrete interior slab. Instead of a 2'x 2'(610 mm x 610 mm) grid size, a 1'x 1' (305 mm x 305 mm) paper grid was used due to closely spaced rebar. The actual (design) rebar spacings are given in Table 10.

Table 10: Comparison of Profoscope and GPR average estimates versus drawing values

Rebar Parameters (Average values in mm)		**Site SI-3006A**			**SureSpan Structures**			**Materials Lab at University of Victoria**		
		NDT techniques		**Actual**	**NDT techniques**		**Actual**	**NDT techniques**		**Actual**
Type	**Direction**	**Profoscope**	**GPR**		**Profoscope**	**GPR**		**Profoscope**	**GPR**	
Cover	Lateral	33	34	40	84	95	65	77	93	112
	Transverse	28	24	30	83	74	75	86	106	123
Spacing	Lateral	120	73	75	104	148	125	218	236	229
	Transverse	187	150	125	255	204	200	227	234	229
Diameter	Lateral	40	Could not be determined	30	Could not be determined	Could not be deter mined	16	9	13	11.3
	Transverse	30	10	11.3		22	11.3	Could not be determined	Could not be deter mined	11.3
Cover (Difference)	Lateral	-7	-6	-	19	30	-	-35	-19	-
	Transverse	-3	-6	-	8	-1	-	-37	-17	-
Spacing (Difference)	Lateral	45	-2	-	-21	23	-	-11	7	-
	Transverse	62	25	-	55	4	-	-2	5	-
Diameter (Difference)	Lateral	10	Could not be determined	-	Could not be determined	Could not be deter mined	-	2.3	1.7	-
	Transverse	19	-1.3	-		10.7	-	Could not be determined		-

The grid paper was taped to the top surface of the concrete girder, as can be seen in Figure 35. The location of the grid paper was measured relative to the edge of the structure for reference.

Figure 35: GPR and Profoscope tests on the top the precast girder at Surespan Structures

Reinforced concrete test slab panel at the University of Victoria

Reinforced Concrete slab panel was tested at the University of Victoria using both GPR and Profoscope. Testing was performed on one of the 914 x 914 x 140 mm (thick) concrete slabs with a single layer of 10M (11.3 mm) reinforcement, as seen in Figure 36. This slab was further destructively tested to validate the rebar cover and spacing obtained by GPR and Profoscope.

To collect the data using GPR and Profoscope, a 2'x 2' (610 mm x 610 mm) paper grid was taped to the top surface of the concrete slab, as seen in Figure 37. The location of the grid paper was measured relative to the edge of the concrete sample in order to identify the exact location of the test results. Guidelines of the grid were traced onto the slab for use during future destructive testing. To identify rebars in both the directions, Profoscope and GPR was moved in both the directions. For Profoscope, measurements were taken along the lines y =3, 6, 9, and 12 respectively when detecting lateral rebars. For transverse rebar detection using Profoscope, measurements were taken along the lines x=16, 19, 22, and 25 respectively. Please note that each line on the grid is spaced at 50.8 mm.

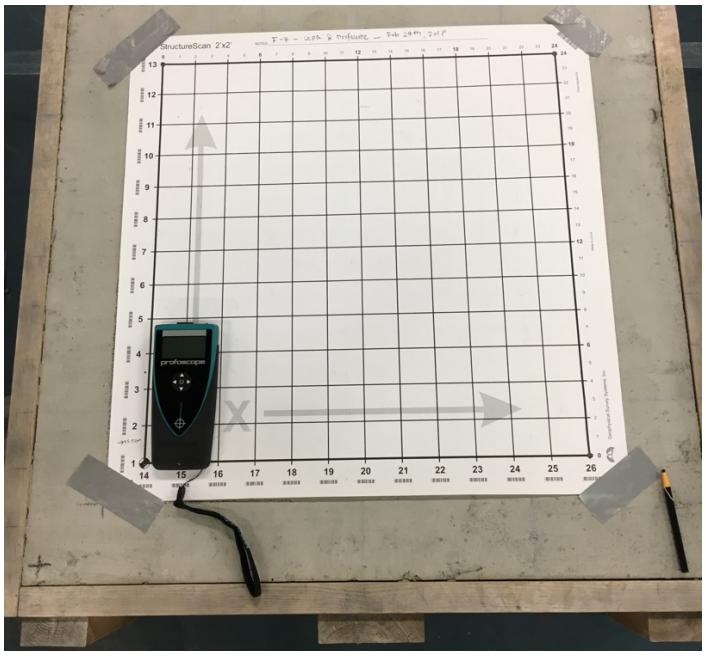

Figure 36: GPR and Profoscope tests on the top the reinforced concrete slab panel at the University of Victoria

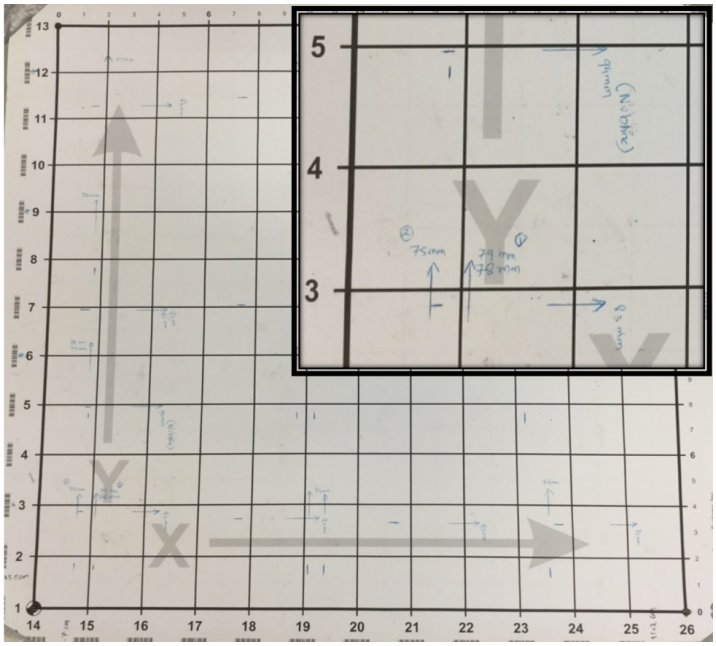

Figure 37: Mapped Profoscope data on the 2’ X 2’ grid (610 mm x 610 mm) (Arrows in the zoomed view indicate the direction of the rebar; the numbers indicate the cover of the rebar. No diameter was obtained as the cover was over 65 mm)

GPR data were collected using the same 2’x 2’ (610 mm x 610 mm) grid. The GPR was run along each one of the grid lines, for a total of 26 different passes with the GPR (13 vertical lines, 13 horizontal lines).

3.5b Results and Discussions

The collected results from both techniques are discussed separately for the ease of understanding.

GPR

The collected GPR data was modeled in the GSSI software called RADAN. In order to compare the GPR data with the record drawings, the GPR data points (in terms of x-y coordinates) were exported as a .csv file and modeled into AutoCAD software. RADAN uses specialized module- StructureScan to map reinforcement over large areas in large structures. Prior to the depth calculation, the concrete surface is automatically located into the software. RADAN software locates the points of maximum amplitude within the slab layers or rebar (Concrete Handbook-GSSI, 2015). The software extracts coordinate and amplitude information into a numerical database which is then exported into a .csv file as mentioned earlier.

In Figure 38 to Figure 40, the GPR data points were modeled in red while the record drawings (design rebar grid) were modeled in black. It can be seen that the modeled GPR results do not exactly match the record drawings. However, in the data from all the experiments, the shapes of the grids were reflective of the designs as can be seen in Figure 38 to Figure 40. The error in determining the spacing at the University of Victoria was least for both directional (lateral and transverse) rebar. In addition, the lateral rebar spacing at Site SI-3006A was 73 mm compared to 75 from the drawing and the transverse rebar spacing at SureSpan Structures was 204 mm compared to 200 mm from the drawing. The other two instances, transverse rebar spacing difference at Site SI- 3006A and lateral rebar spacing difference at SureSpan Structures were very high as can be seen in Table 10.

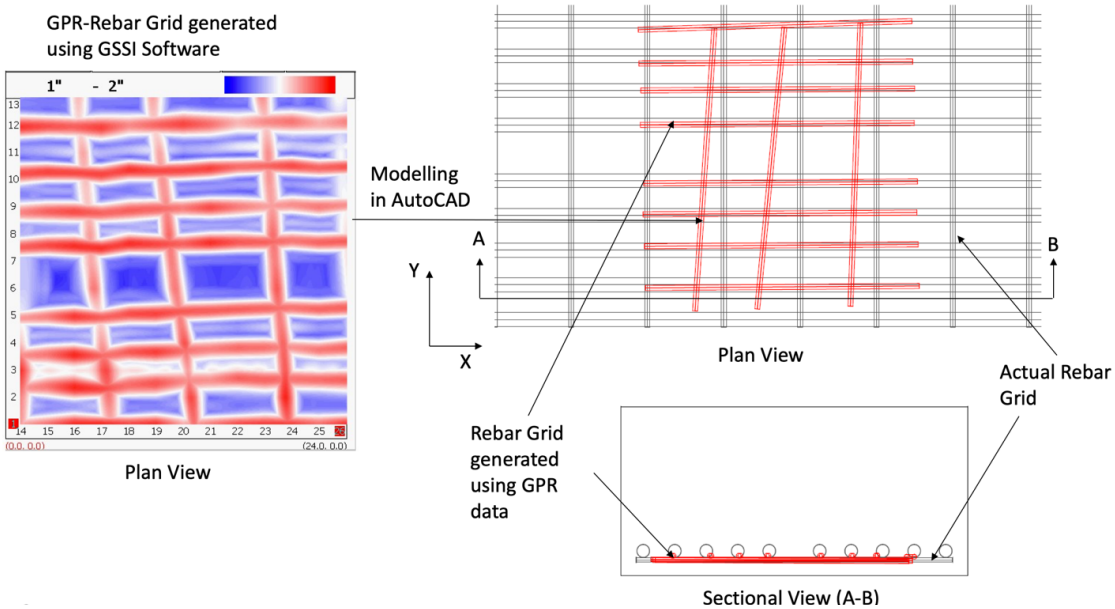

Figure 38: Rebar Grid generated using GPR data (RC Bridge Deck Slab at Site SI-3006A)

Note: The rebar co-ordinates from the GPR rebar grid are reversed in the AutoCAD model

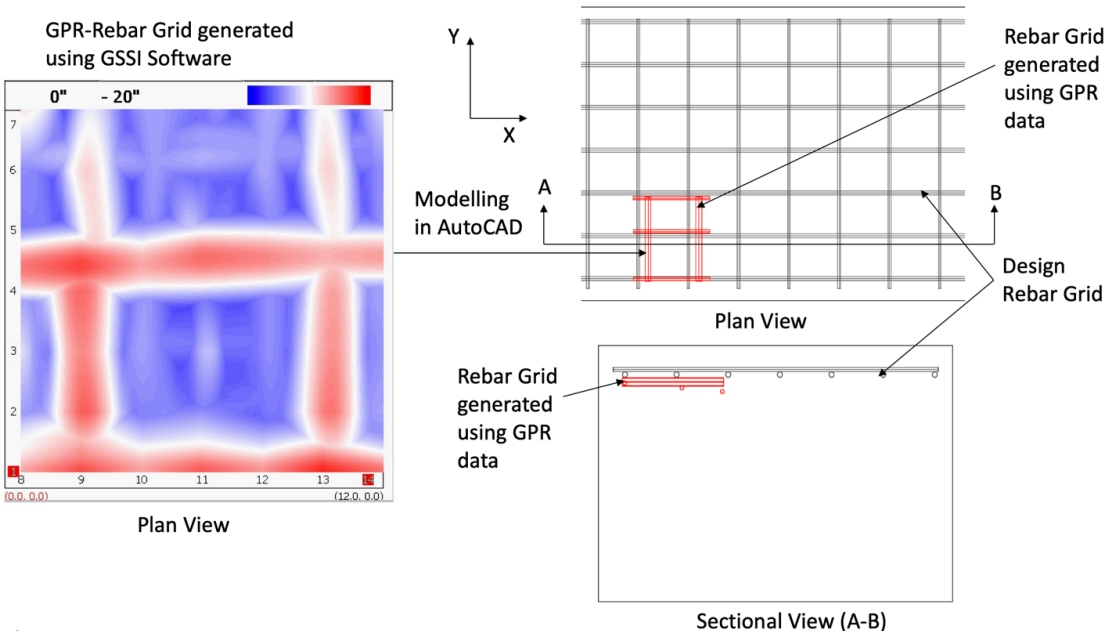

Figure 39: Rebar Grid generated using GPR data (RC Precast Girder at Surespan Structures)

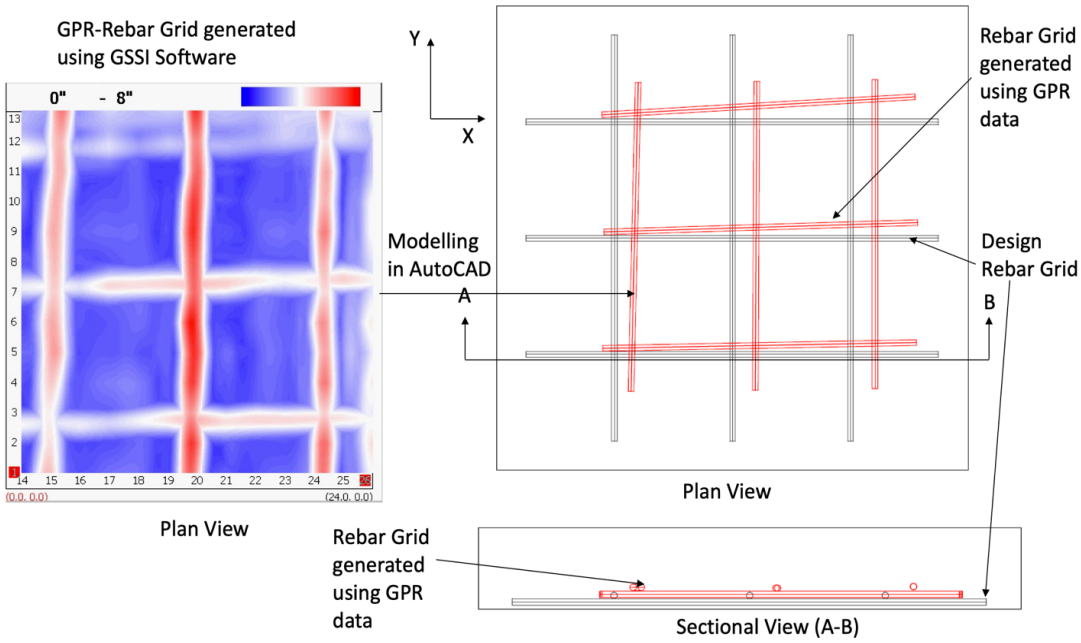

Figure 40: Rebar Grid generated using GPR data (RC slab panel at the University of Victoria)

The covers were found to be within 30 mm of the design drawings. The diameter of the rebar could only be obtained for the first rebar from the surface. The rebar diameter measured for the slab located at Surespan was estimated to be 22 mm when it is actually 11.3 mm (10M), which is a significant error. The possible reasons for this could be the closely spaced rebar and/or the thickness of the girder. The diameter values obtained using

GPR at other locations (at Site SI-3006A and the lab) were close (difference of 1.3 mm (at SI-3006A) and 2.3 mm (at the lab)) to the design values.

Errors of measurement with the GPR were likely introduced when drawing and measuring the grid. Small skews in the alignment of rebar were likely caused by incorrectly measuring the squareness of the grid with relation to the slab. This error was likely to be most prevalent on the slab from SI-3006A, as the paper grid would not stay on the bottom surface of the bridge, so the grid had to be drawn by hand. Other misalignments with existing drawings could be due to variation in construction, such as adding additional rebar, or lap splicing. The two girders tested in the field may have had different surface moisture content. The variation of surface moisture on the slabs may have affected the accuracy of the GPR because the dielectric constant (an input of the GPR which effects signal resolution) changes with moisture within concrete. Different values of dielectric constants were assumed depending upon the type of concrete. The dielectric constant of 6 was chosen for moderately dry concrete and 9 for saturated concrete. A dielectric of 3 to 12 corresponds to radar velocities from 7 to 3.5 inches per nanosecond (or 18 to 9 cm per nanosecond), respectively. GPR determines the radar velocities depending upon the chosen dielectric constant.

Key challenges of using GPR (StructureScan Mini) in the field

Following is the list of some of the key challenges that authors have faced during the use of GPR,

1. While moving the equipment on the grid, it is very difficult to maintain the alignment. Any misalignment has a direct effect on the results produced.
2. StructureScan mini requires the concrete surface to be smooth as the wheel size are very small. Concrete surface irregularities may introduce error in rebar grid mapping. In addition, GPR will also detect any subsurface anomalies such as honeycombing, delamination, and voids due to the difference in the dielectric constant. Any subsurface anomalies will be displayed in the 3D rebar grid map. It should be noted that any subsurface defects may not necessarily interfere with the results of mapping rebar grid as the dielectric constant of steel is very different.
3. The equipment is very difficult to work with when used underneath (upside-down) or on the side of a slab or girder.

Rebar detector-Profoscope

From the testing on three different types of RC slabs, it was found that the Profoscope tests were much more prone to error. The method used works well for slabs with largely spaced reinforcement that have drawings available due to the fact that the instrument requires an estimated rebar diameter for higher accuracy. It was very difficult to identify rebar when testing a slab with unknown reinforcement, or tightly spaced rebar. Also, it is difficult to differentiate between a lateral and transverse rebar, or if the measurement is being taken at an intersection between the two.

The test results from the bridge deck (Figure 41) and the precast girder (Figure 42) both poorly reflected the general shape of the rebar grid: missing rebar, large skews, and strange spacing. As noted, the results obtained by the Profoscope on RC slab panel at the University of Victoria reflected the layout of the grid well (Figure 43), and rebar spacing was estimated

to be within 7 mm of the design drawings. This is likely due to the larger spacing between the two rebars.

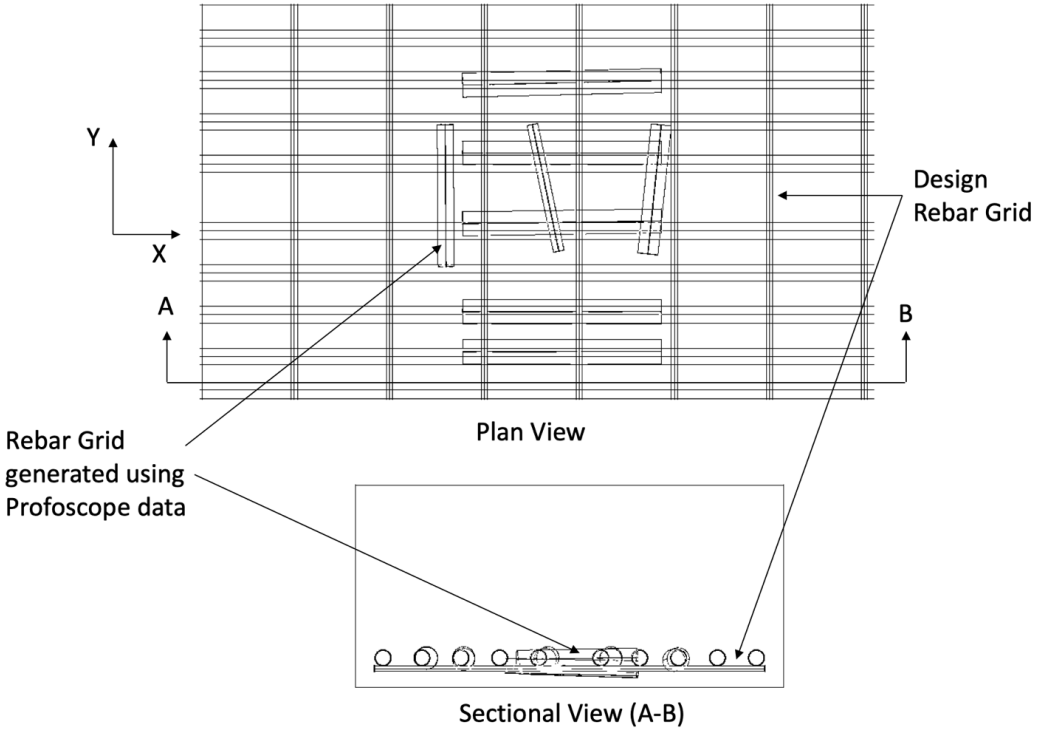

Figure 41: Rebar Grid generated using Profoscope data (RC Bridge Deck Slab at Site SI-3006A)

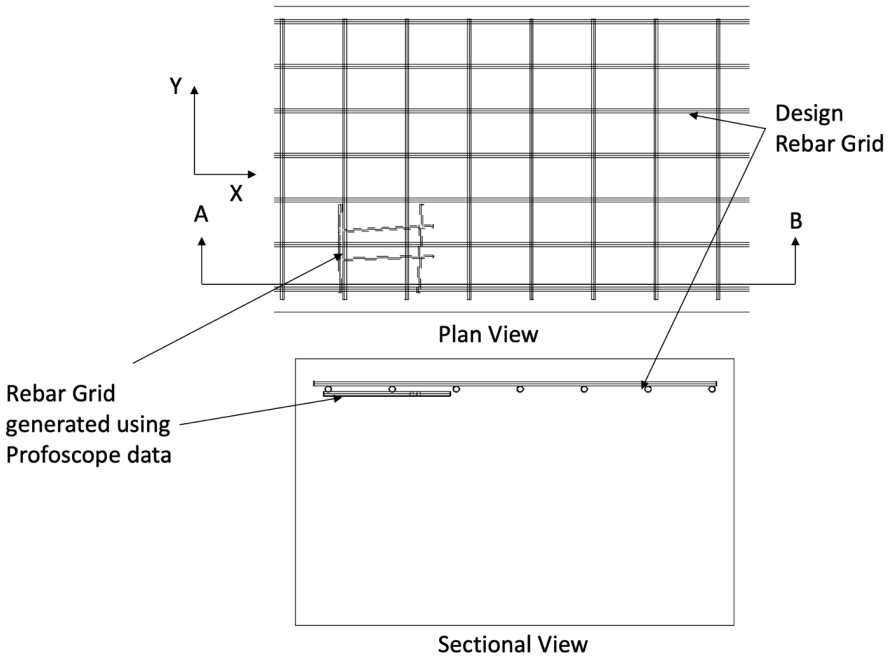

Figure 42: Rebar Grid generated using Profoscope data (RC Precast Girder at Surespan Structures)

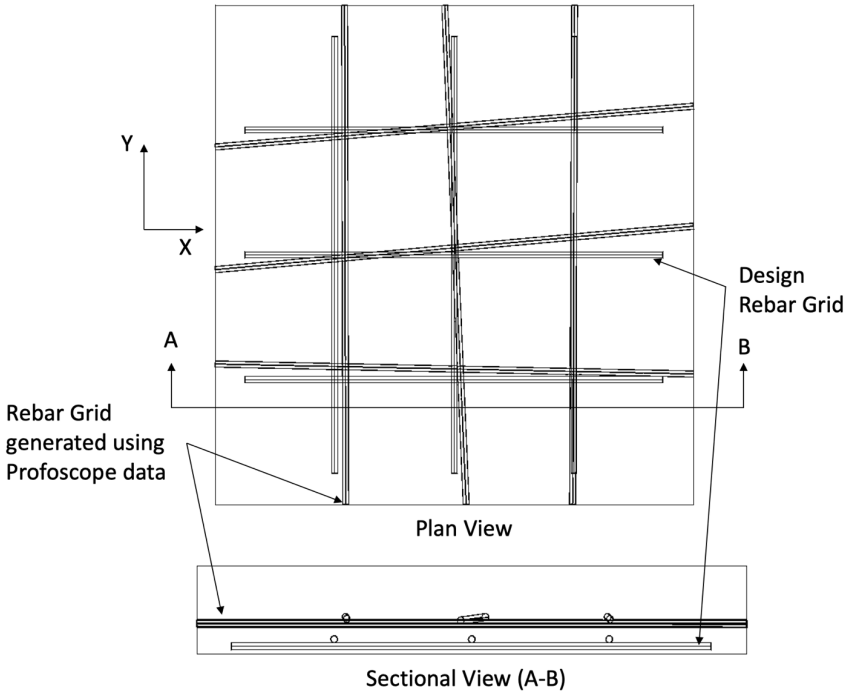

Figure 43: Rebar Grid generated using Profoscope data (RC slab panel at the University of Victoria)

The average spacing for the Profoscope testing ranged from 2-62 mm of the design. The average cover was within 37 mm of the design, which is a large range. The Profoscope can only measure rebar diameter to a depth of 65 mm, as such, only the diameters of the slab at SI-3006A could be determined. Measured rebar diameter was within 10-19 mm (for lateral rebar: Profoscope result = 40 mm, and design value = 30 mm, for transverse rebar: Profoscope result = 30 mm, and design value = 11.3 mm) of the design drawings.

Key challenges of using Profoscope in the field

In addition to the limitations mentioned above, following is the list of some of the key challenges that authors have faced during the use of Profoscope,

1. The equipment requires a firm contact with the concrete surface in order to detect rebar in concrete. It is difficult to maintain firm contact when the concrete surface is not smooth.
2. The sensitivity of the equipment in detecting rebar is quite low.

Destructive testing

In order to validate the NDT techniques' results, the RC slab at the University of Victoria was destructively tested to expose the rebar using a chisel and hammer as shown in Figure 44. This was the only way to confirm the results of the NDT techniques against a "real" value. It was found that the spacing and cover both were equal to the dimensions mentioned in the drawings. The results obtained from the NDT techniques were compared against the drawing dimensions as shown in Table 10. It should be noted that the RC deck slabs at the other two sites were not destructively tested due to restriction from the owner. However, both the slabs were constructed in a very controlled environment at SureSpan Structures precast facility.

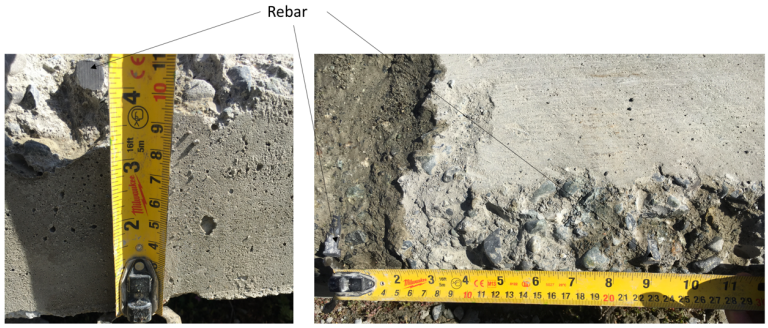

Figure 44: Destructive testing of the Slab at the University of Victoria to locate the rebar spacing and cover

3.6b An accuracy model of GPR and Profoscope

In order to determine the measurement accuracy of both the techniques, the values obtained were compared against the true values given in the drawings. It is assumed (with the exception of the test slab at UVic) that the values in the drawings are the true values. The values compared in Table 10 were used to determine the percentage error in the measurements. Figure 45 shows the calculated percentage error of both techniques at all three locations.

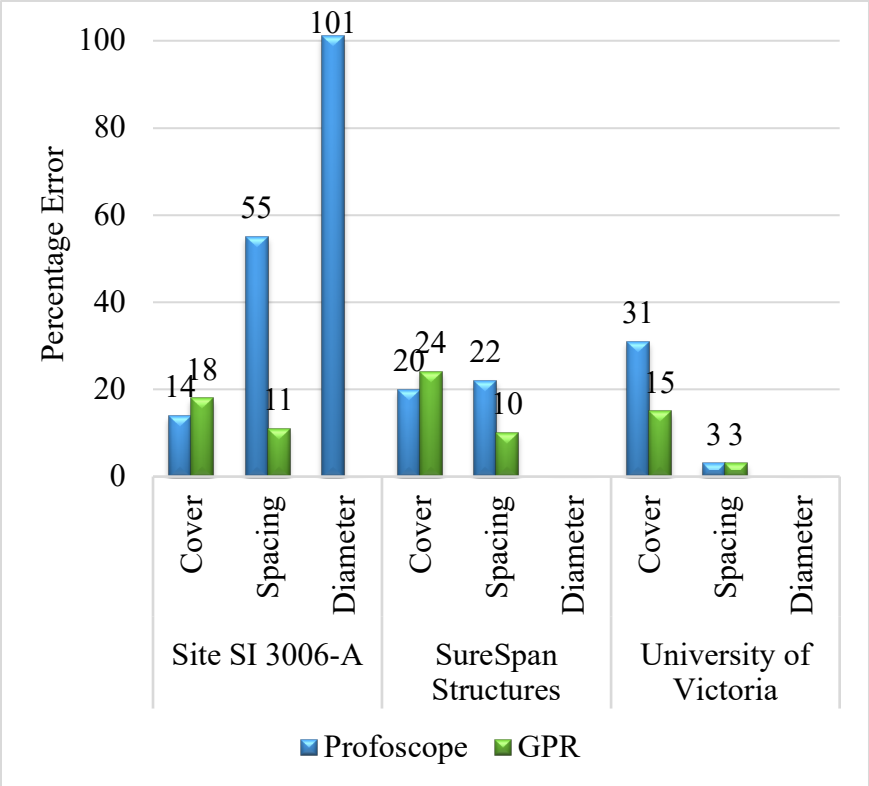

Figure 45: Percentage error model of GPR and Profoscope

Percentage error from the rebar cover data collected from Profoscope was 14%, 20% and 31% at the Bridge site, at Surespan Structures and at UVic respectively. This shows that as the rebar cover increases the error from the data collected by the Profoscope increases. For

GPR, percentage error from the rebar cover data collected was 18, 24 and 15 at the Bridge site, at Surespan Structures, and UVic respectively. The percentage error in determining the rebar spacing using Profoscope was 55%, 22%, and 3% and using the GPR, it was 11%, 10% and 2% at the Bridge site, at Surespan Structures and at UVic respectively. It can be seen that the percentage error using both the techniques in determining rebar spacing at the bridge site was highest due to the fact that the readings were collected upside down (bottom part of the bridge deck). From Table 10 and Figure 45, it can be seen that the percentage error in determining rebar diameter using both the techniques was very high (more than 100%) at some of the locations. It also includes some of the instances where the diameter could not be determined. It should also be noted that the GPR was unsuccessful in determining rebar diameter at all three locations. Rebar spacing determined by GPR has the least error. Overall percentage error for the Profoscope is higher compared to GPR as expected. The overall percentage errors by the two techniques at the bridge site were found to be the highest compared to other locations.

3.7b Conclusions

Both GPR and the Profoscope may be used to assess in situ rebar detail, but users should be aware that both testing methods lack accuracy. Matching the results of both tests to record drawings with a high amount of confidence could be difficult without background information or destructive testing. The data collected suggests that GPR gives more consistent and accurate data with regards to spacing and cover. It should also be noted that the cost of the GPR equipment used in this study is $15,000 CAD while the cost of the Profoscope is $5000 CAD. GPR took about 3 hours in total to map the rebar grids while Profoscope took about 15 hours in total to map the rebar grids at all three locations. Following conclusions can be drawn from this research study,

1. The GPR was found to be much easier to use in the field. The data collection process was simple and easily repeatable, with very little chance for human error. The testing was fast, taking 10-15 min to do a 2'x 2' grid at all three locations.
2. Data collection for the Profoscope was slow, difficult to repeat, and required many inputs which increased the chance of an error occurring. The testing of a 2'x 2' grid took more than 1.5 hours at all three locations. In addition the authors took more than 2 hours in mapping the rebar grid at each site location.
3. Percentage error (with respect to the design drawings) from the rebar cover data collected from Profoscope was 14%, 20%, and 31% at the Bridge site, at Surespan Structures, and UVic respectively. This shows that as the rebar cover increases the error from the data collected by the Profoscope increases.
4. For GPR, percentage error (with respect to the design drawings) from the rebar cover data collected was 18, 24, and 15 at the Bridge site, at Surespan Structures, and UVic respectively.
5. Percentage error (with respect to the design drawings) in determining the rebar spacing using Profoscope was 55%, 22%, and 3% and using the GPR, it was 11%, 10% and 2% at the Bridge site, at Surespan Structures, and UVic respectively. It should be noted that GPR processed images shown in figures 6 to 9 have a slight skew in the rebar grid. This could be due to the construction error where the rebar might not be properly positioned as per the design drawing and the GPR data could be accurate.

Chapter 4: UAV-assisted Condition Assessment of Long Span Railway Bridges

Harsh Rathod[1], Rishi Gupta[2], Manivannan Rangasamy[3], and Balasubramanian Esakki[4]

[1]PhD Student, Department of Civil Engineering, University of Victoria, Victoria BC, Canada, email: hmrathod@uvic.ca

[2]Associate Professor, Department of Civil Engineering, University of Victoria, Victoria BC, Canada, email: guptar@uvic.ca

[3]Junior Research Fellow, Department of Electronics and Communication Engineering, Vel Tech University, Chenna, Tamilnadu, India, email: manivannanrangasamy@gmail.com

[4]Associate Professor, Centre for Autonomous System Research, Vel Tech University, Chennai, Tamilnadu, India. email: esak.bala@gmail.com

Note: This chapter is adapted in part from submitted work (Rathod et al., 2019d) in infrastructures, MDPI, with permission where appropriate. This chapter presents a new Unmanned Aerial Vehicle (UAV)-assisted American Association of State Highway and Transportation Officials (AASHTO) guideline-based damage assessment technique. In addition, at the end of this chapter in section 4A and 4B, two novel patent pending robotics-based data collection and data analysis methodologies are presented.

4.1 Abstract

Visual inspection is the most commonly used technique to assess and inspect bridges globally. This technique frequently becomes inadequate and unreliable when inaccessible areas of infrastructure cannot be inspected. Also, this technique is laborious, time-consuming, and expensive in case of long span and elevated bridges where expensive scaffold or other arrangements are required for condition assessment. One of the solutions to this problem lies in incorporating the use of Unmanned Aerial Vehicles (UAVs) to conduct a non-contact assessment at a reduced operating cost with high reliability. The use of UAVs allows coverage of large areas in a very short duration and can also be made autonomous to inspect different structural elements, including ones that are otherwise inaccessible to people. The present research utilizes a combination of a UAV system, an image processing tool and the guideline published by the American Association of State Highway and Transportation Officials (AASHTO) to inspect a long span railway bridge. This paper describes the difference between two different inspection methods; the damage computed by solely conducting an on-site visual inspection, and the damage calculated using image processing tool integrated with the AASHTO guide manual. It has been found that the new technique (IPA- image processing tool integrated with the AASHTO guide manual) proposed by the authors could improve inspection accuracy, save time, and save cost. However, the use of a UAV system is very sensitive to external weather condition, a UAV cannot clean up the surfaces that a visual inspector could clean before taking a photo, and the areas where the GPS satellites are not available, a UAV is difficult to fly.

4.2 Introduction

Bridges are a vital component of any rail or road network, providing connectivity links to serve domestic and industrial transportation needs in any country. Apart from personal mobility, bridges also support commerce and economic vitality. As an example, the Indian Railways have about 127,000 bridges out of which about 16,000 are steel girder bridges, many of them are old and in a deteriorated condition (Gangopadhyay et al., 2016). There is an immediate need to inspect and monitor the condition of these bridges on a timely basis. At present, the bridge inspection is mostly confined to visual means, which is inadequate and also not reliable (Rice et al., 2016) when several areas of a bridge are not accessible for inspection. The labor-intensive approach for inspection of the bridges requires a huge investment in terms of the arrangement of temporary scaffoldings/permanent platforms, labor charges, and so on. Besides, this approach is also time-consuming and managerial intensive (Dong et al., 2003). Certain routes in the Indian Railways have been identified to carry mineral loaded trains with special wagons, which are more substantial and faster (Bhattacharya et al., 2007). Bridges on these routes desperately need condition assessment regularly to enable them to service safely. One of the solutions to these problems lies in conducting an Unmanned Aerial Vehicle (UAV)-assisted condition assessment.

Usage of UAVs can allow coverage of large areas in a very short duration and can be made autonomous to inspect a wide variety of structures. The inspection instruments are mounted on UAVs to transmit information in real-time, thereby facilitating inspection from the ground station. Along with that, real-time interfacing with image processing systems can support the processing of thousands of images which can expedite the diagnosis process significantly. The unique benefit is that digitization of the entire monitoring activity has widened the scope for easy storage, sharing, and better accessibility to end user. Another advantage is that the whole inspection technique is cost-effective (Gillins et al., 2016) as the entire structure could be inspected automatically using cost-effective UAV-images (Truong-Hong et al., 2018).

In recent years, there has been significant progress in UAV research, including in the field of Structural Health Monitoring. Major work conducted is around image processing and damage detection. One of the ways to inspect bridges using UAV is to collect images and convert them into a 3-dimensional imagery model. Khaloo et al., 2018 have discussed the application of such a 3-D model for inspecting a bridge. The effect of angles and distance is discussed by Chen S. et al., 2016, when constructing a 3-D model.

The work conducted by Sankarasrinivasan et al., 2015 and Pragalath et al., 2018 have demonstrated the use and effectiveness of UAVs and image processing algorithms to quantify the surface deteriorations like cracks, discoloration, efflorescence, leaching and spalling in bridges. The research conducted by other researchers has also demonstrated the use of UAVs and image processing tools to quantify surface damage in civil infrastructures. Ellenberg et al., 2016 used techniques such as homography and lens distortion correction in a post-processing framework that allows the use of color images obtained by UAVs for actual damage quantification measurements. The experiments were conducted on the structures with simulated damage. Research conducted by Kim et al., 2017 showed a crack identification strategy by combining hybrid image processing with UAV technology. Using the combination, they were able to successfully measure cracks thicker than 0.1 mm with the maximum length estimation error of 7.3%. Kim et al., 2018 have also successfully

applied the developed Crack Identification Techniques for inspecting an aging concrete bridge. Another research by Krick et al., 2015 and Ellenberg et al., 2016 demonstrated the use of photogrammetric and Simultaneous Localization and Mapping (SLAM) algorithms through X-Box Kinnect (optical metrology system) to measure deformation on bridges. Indoor and outdoor inspections were conducted using UAVs to detect cracks and corrosion using image processing algorithms. Recently conducted research by Chiu et al., 2017 shows the use of UAVs to measure the displacement of large structures. However, a significant knowledge gap remains that helps quantify the improvements UAVs can offer to the current practice of visual condition assessment using existing bridge inspection guidelines such as that published by AASHTO. The present research by the authors shows the difference between the damage computed solely by very subjective on-site visual inspection and compares this to the results of a more objective approach where AASHTO-based inspection guide manual (American Association of State Highway and Transportation Officials, 2014) is complemented with an image processing tool. This paper also reports the research conducted on the development of a UAV system that could be used effectively for performing a condition assessment of bridges, especially long span railway bridges. Although the research presented in this paper focuses on a long span railway bridge, the majority of the outcomes could be applied on long span vehicular bridges/overpasses.

4.3 Research Significance

There has been past research work related to UAVs (Unmanned Aerial Vehicles) in the field of Structural Health Monitoring. However, this manuscript has a unique aspect, mainly the development of a new inspection methodology which integrates UAV-based data collection, and image processing with AASHTO-based condition assessment guideline. Also, the manuscript highlights the differences between two inspection methodologies; the damage computed by solely conducting an on-site visual inspection, and the damage calculated using image processing tool integrated with the AASHTO guide manual. Note that in North America, majority of DOTs (Department of Transportations in the U.S.) and provincial governments (in Canada) use AASHTO guide manual in conjunction with the AREMA (American Railway Engineering and Maintenance-of-Way Association) Bridge Inspection Handbook when conducting a railroad bridge inspection. However, the railroad bridge inspected in this research work is in similar nature of other highway bridges where an inspector could only use the AASHTO guide manual for bridge element inspection to perform the inspection.

4.4 Development of a UAV system

The Rotary Unmanned Aerial Vehicles (RUAVs) are promising due to its inherent ability to hover, vertical take-off and landing and autonomous navigation capabilities. Due to its overwhelming advantages, RUAVs are deployed in multiple missions, including environmental monitoring, agricultural applications, disaster management, power line inspection, and military surveillance. The RUAVs used in these areas have several common features such as intelligent flight control (Autonomous flying capability), higher payload carrying capacity (usually greater than 1 kg), excellent stability against strong wind and, excellent battery endurance (on average more than 20 min.). RUAVs used in the field of Structural Health Monitoring (Particularly bridge inspection) are slightly different

as they require some additional features such as the ability to look up when inspecting bridge deck from underneath, obstacle avoidance system (Ultrasonic sensors-based) and ability to fly without GPS. One such system has been developed and proposed by Chen J. et al., 2016. In their study, they developed a hexarotor frame with an upward camera gimbal (to look up) with a capability to avoid obstacles and the ability to fly without GPS. Similar, aircraft has been designed and built by the authors of this paper.

The design specifications of the custom-built RUAV is given in Table 11. From Figure 46, it can be seen that the RUAV is equipped with not only an optical camera sensor but also an infrared camera. However, the infrared thermographs are not included in the scope of this paper. The RUAV used in this work has a payload of 2 kg with an endurance of approximately 20 minutes with a range of 2 km depending upon the weather conditions. The constructed RUAV has autonomous capabilities (Using GPS shown in Figure 46) wherein predefined waypoints can be selected with geotagging on video locations, speed, and directions of the vehicles are controlled precisely. A high-end autopilot system is embedded into the RUAV to control the vehicle and navigate into the prescribed location of interest. Using the autopilot capability, all sides (360 degrees) of bridge piers can be inspected efficiently without manually controlling the vehicle. The vehicle also has the capability to fly without GPS.

Table 11: Custom built RUAV design specifications

Components	**Weight (gm)**	**Quantity**	**Total Weight (gm)**
Motor KV 420 (420 rpm/V); 880 Watts (75% Power)	225 g	8	2040
80A Electronic Speed Controller (Motor Power required per 10 V = 88 A)	106g	8	848
CF 16 X 5.4 Propeller (CW & CCW)	70	8	560
Battery 6s 1000 mAh (Watts = 8 (No. Motors) × 880 = 7040 Watts So, 2 × 10,000 mAh battery = 20,000 mAh 20,000 mAh/1000 = 20 Amps)	575	2	1150
CF Complete Airframe with Landing Skid	850	1	650
Flight Controller	265	1	245
Accessories (Plugs, Connectors & Wires)	250	1	150
Payload (Infrared Camera and Optical Camera)	4000	1	4000
Total Weight = 9.6 kg			
Endurance Limit Calculation is given in appendix B			

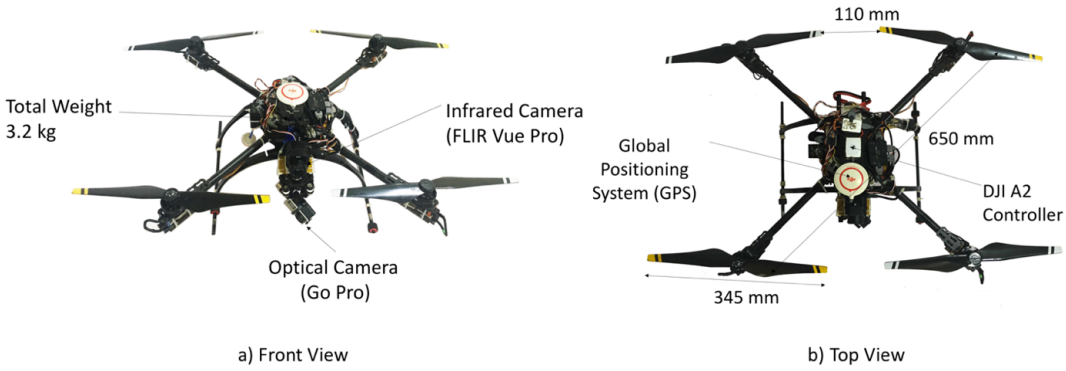

Figure 46: Custom built RUAV for civil infrastructure monitoring

The developed RUAV was tested under various environmental wind load conditions for its stability and hovering aspects. The vehicle has shown tremendous ability to handle diverse wind loads, which is an essential consideration during Structural Health Monitoring (SHM) applications. The vehicle can remain stable for up to 20 km/h (about 10 knots) of wind speed. A high definition (Go-Pro) UAV mountable camera is integrated into RUAV with the aid of a gimbal and videos are streamlined to the Ground Control Station (GCS). The gimbal is rotated in such a way that videos are captured perpendicular to the surface of the structure. This particular aspect is required when processing the collected images and calculating the damage quantity accurately.

The videos are recorded onto the onboard memory and at the same time, transmitted to the GCS. A switch between autonomous to manual mode is directed appropriately for safe landing of the vehicle. The speed of the vehicle is varied between 3 m/s to 5 m/s with respect to the bridge locations in the GCS. Note that the exercise related to determining the optimum aircraft velocity was performed at the University of Victoria prior to deploying for a bridge inspection. From the exercise, it was found that for the specified crack sizes and blur, the operation should take place at a speed of no more than about 8.2 m/s at a distance of about 1.3 m from the concrete surface (Blaney, 2018). The detailed calculations related to various crack size, camera type, and other variables are reported in (Blaney, 2018).

4.5 Long Span Railway Bridge Inspection

A long span 55 years old railway bridge named as Poiney (also called Ponnai) Bridge in India was chosen for inspection as a part of the collaborative project sponsored by Canada-India Research Centre of Excellence (IC-IMPACTS) to accelerate Community Transformation and Sustainability. The bridge is located across the Bahuda river in Thiruvalam, Tamilnadu, India. The bridge has a total of 28 spans (each span is approximately 21.2 m) reinforced concrete deck slab supported by prestressed concrete girders as superstructure (as shown in Figure 47) and concrete abutments and piers as the substructure.

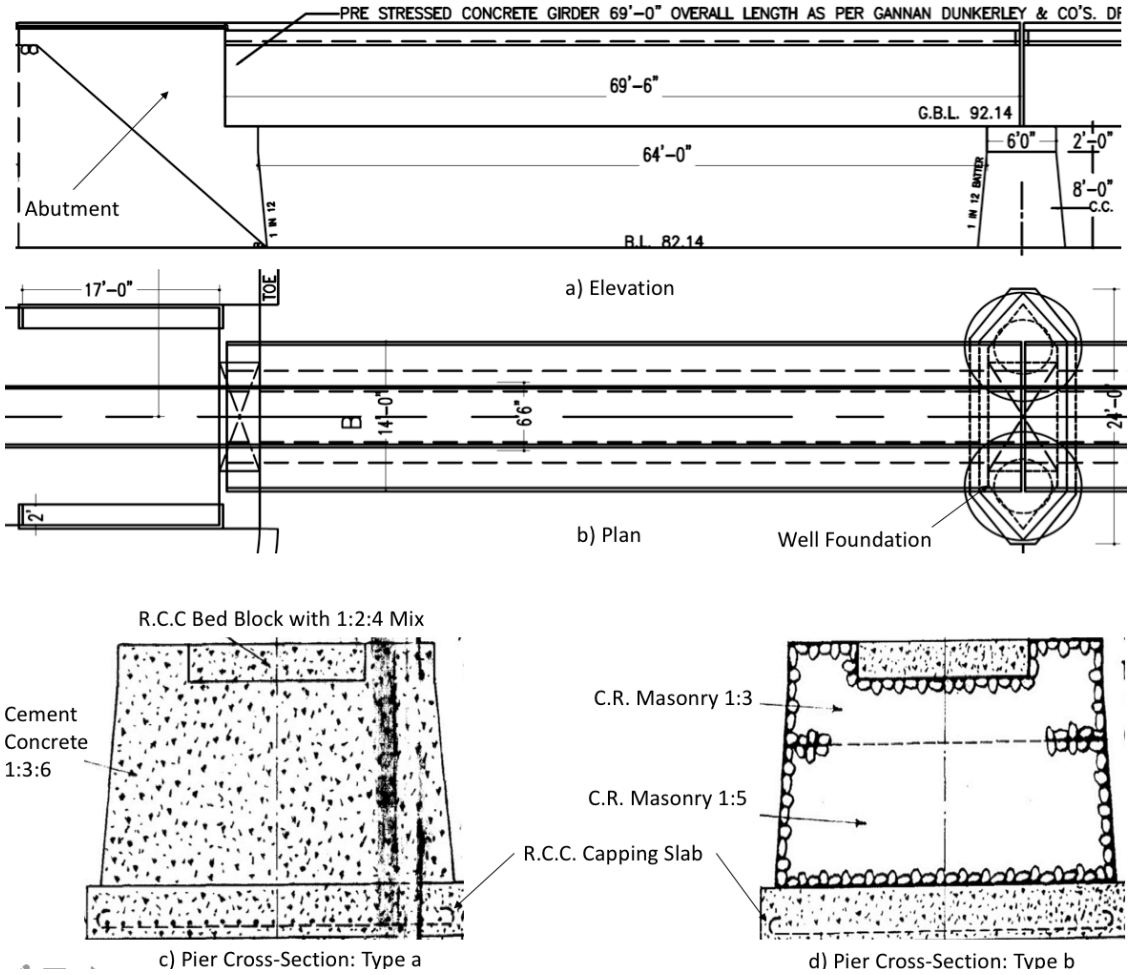

Figure 47: Railway Bridge a) Elevation b) Plan c) Pier Cross Section: Type a, and d) Pier Cross-Section Type b (Source: Ministry of Southern Railways Bridge Drawings Record, India)

The typical cross sections of the piers are shown in Figure 47. This information is obtained from the Engineer-in-charge at southern Indian Railway. From the cross-section of the piers, it can be seen that they were supported on a well foundation with the well diameter (external) of 10 ft. (3.048 m). The circular walls of the well foundation were constructed using concrete (Mix Proportion: 1:3:6; 1 part cement, 3 parts sand, and 6 parts aggregates) as reported in the drawings provided by the Indian Railway Authority. The sand filling was used in all type of well foundations. Reinforced Cement Concrete (RCC) capping slab was used to support load transfer between the piers and the foundation. The piers were constructed using either concrete, coarse rubble masonry in cement mortar or combination of both. Note that all the piers were unreinforced.

Figure 48 shows in schematic form the location and arrangement of the 28 piers along with the UAV flight path (in red) that was designed for inspection of this bridge. Due to the limitation of the battery endurance, only a portion of the bridge was inspected in two visits during this project. As can be seen in Figure 48, the flight path (a-b-c-d) starts with the inspection of two sides first. In order to assess the condition of abutments and piers, a flight path (Shown in Figure 3) e-f-g-h-i-j-k-l-m-n-o-p-q-r-s-t-u-v-w-x-y-z-A-B-C-D-E-F-

G-H-I-J-K-L was followed. To assess the girders from underneath flight paths, M-N, O-P, and Q-S were followed. The inspection was completed at a speed of 4-5 m/s and with a perpendicular distance of about 1 m from the concrete surface. The entire inspection required three people in total. These three people included a pilot in command, a visual observer, and a ground security person. The inspection was completed during daylight hours with a diffuse skylight condition ranging between 3,000 to 18,000 lux.

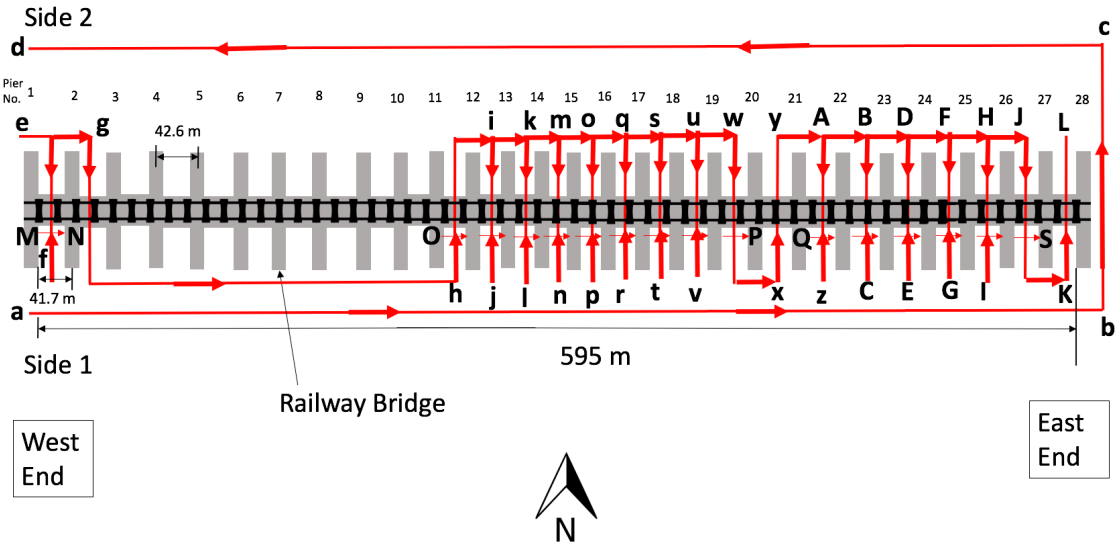

Figure 48: UAV flight path (Shown in RED)

4.6 Results and Discussion

The railway bridge was inspected using two different methodologies, 1) visual inspection on site (with the use of AASHTO guide manual (AASHTO, 2011)), and 2) image processing integrated with AASHTO guide manual procedure (will be called "IPA" throughout the text). The comparison of the results obtained using both the techniques is made in the next section. Damage quantification results in each technique are discussed here.

On-site visual inspection

For this project, special permission was received from Southern Indian Railways to conduct the inspection. However, the requirement was to inspect in the presence of Railway staff and a flagger. This limited amount of time the research team could spend on the bridge, was frequently interrupted by passing trains. Given these limitations, on a small section of the bridge, a focused on-site visual inspection was performed by the authors to quantify the damage in the bridge. The visual inspection was performed from the man refuge (on the bridge) and while standing on the ground. This was done to follow the procedure one would follow during a routine inspection at this bridge. To compare the results with the IPA, the same spans where the UAV flights were run (Figure 48) were selected for visual inspection. The damage rating was assigned to different elements of the bridge by noting various visual defects. The assignment of the damage rating was performed with the use of the AASHTO guide manual (AASHTO, 2011). AASHTO philosophy was used to assign the condition rating (1 to 4 where 1 being good and 4 being severe) of the bridge elements.

Table 12 shows the physical condition states recorded for different elements when visually inspected. The physical condition ratings are the average rating of the same elements of different spans. From Table 12, it can be noticed that majority of the damage was observed in the piers and abutment with mild efflorescence at isolated locations, severe discoloration and severe map cracking possibly due to Alkali Silicate Reaction (ASR)/Alkali-Aggregate Reaction (AAR). Overall condition state of the piers was identified as poor (condition state 3) mainly contributed by severe map cracking. The condition state of the bridge decks was identified as 1 (in good condition) as only minor local cracking (only on the side) were noticed. Prestressed concrete girders were found to be in very good condition with minor discoloration (deemed just an aesthetic issue). Elastomeric bearings were not assessed as they were not visible from either ground or from any of the man refuges. Table 12 shows the "-" sign in % damage to the elements that were not assessed.

Note that the condition rating was assigned by looking at the significance of the defects and their impact on the elements. The percentage of damage was also assigned for each abutment and pier based on judgment. Again, note that this is how one would assign values when inspecting the 28 spans of the bridge. These damage values are compared to image processing values later in the next section.

Table 12: On-site visual inspection results

Element Description	**Condition State 1**	**Condition State 2**	**Condition State 3**	**Condition State 4**
Concrete Abutment (West End and East End)	-	-	Mild efflorescence at isolated spots, severe discoloration and severe map cracking were observed possibly due to Alkali Silicate Reaction (ASR)/Alkali-Aggregate Reaction (AAR). Rust Staining (1120), Cracking (1010), and Deterioration (1220) with Element 1- 30% damage, Element 28 – 20% damage	-
Reinforced Concrete Deck	Multiple vertical cracks were observed on the one side of deck	-	-	-
Prestressed Concrete Girders	No defects were observed	-	-	-
Elastomeric Bearing	Not completely identifiable			
Pier Walls	-	-	Severe map cracking was observed possibly due to Alkali Silicate Reaction (ASR)/Alkali-Aggregate Reaction (AAR). Rust Staining (1120), Cracking (1010), Deterioration (1220), and Scour (6000)	-

Element #	2	3-11	12	13	14	15	16	17	18	19	20	21	22	23	24	25	26	27
% Damage	25	-	35	60	25	35	45	70	15	40	25	25	50	15	20	35	30	-

Image processing integrated with AASHTO guide manual (IPA)

Guide Manual for Bridge Element Inspection published by AASHTO (AASHTO, 2011) relies on multipath and defect concepts for condition assessment. The manual is intended to be used by an inspector or a professional engineer for simplifying the much more complex conventional inspection procedure that is unstructured, subjective and totally dependent on the visual judgment as discussed earlier. The manual divides the bridge elements into two groups: National Bridge Elements (NBEs) and Bridge Management Elements (BMEs). The combination of both the element groups comprises the full AASHTO element set. In order to assign a condition rating, the bridge elements are quantified in terms of either area or length (as shown in Table 13). Depending upon the area or length of the defects in a particular element, the element is assigned a condition index (1 to 4) based on the judgment. This is a slightly more structured way of assessing, but still based on judgment. To overcome some of the issues faced during the methods discussed earlier, this paper suggests the use of the AASHTO guide manual along with an image processing tool for accurately quantifying defects. The use of a UAV is suggested to assess inaccessible elements of the bridge and expedite the process of inspection while maintaining the safety of personnel.

Table 13: Calculated bridge element dimensions from the available drawings

Element	**Width (m)**	**Length (m)**	**Height (m)**	**Quantity**
Deck				
Reinforced Concrete (RC) Bridge Decks (Total 28 Spans)				
Span 1	4.4	21.184	0.2	93.2 m^2
Span 2 to Span 27	4.4	21.336	0.2	2440.8 m^2
Span 28	4.4	21.387	0.2	94.1 m^2
Super Structure				
Prestressed Concrete Girder-Tapered I shape- (Total 28 Spans) - 2 girders/span				
Span 1	0.65	21.184	0.2	42.368 m
Span 2 to Span 27	0.65	21.336	0.2	554.736 m
Span 28	0.65	21.387	0.2	42.774 m
Elastomeric Bearing (Total 28 spans) each span has 4 bearings = Total 112				
Sub Structure				
Concrete Abutment (Unreinforced) - 1 side - visible				
West end	6.4	-	3.329	21.3056 m^2
East end	7.5	-	3.329	24.9675 m^2
Concrete and Masonry Pier walls (Unreinforced) - All 4 sides -visible				
Pier 1 -Pier 27	2.15	-	3.312	384.53 m^2

The bridge discussed in the previous section was divided into different elemental quantity (shown in Table 13) as described in the Bridge Inspection Manual published by AASHTO. The elemental quantity was calculated by the authors using the drawings provided by the Indian Railways. The quantification was done in either area or length depending upon the type of element. For example, reinforced concrete decks and piers were quantified in terms of the area while prestressed concrete girders were quantified in terms of length. Table 14 and Table 15 show the condition of the deck, superstructure, and substructure. Note that not all of the bridge elements are shown in the tables. The images included in Table 14 and Table 15 are extracted from the videos collected using UAV flights on the day of the inspection. After extracting the images, they are cropped to avoid unnecessary noise picked up during the image collection. Table 15 contains both unprocessed and processed images. The resolution of the images was 640 × 480 pixels with type-RGB. Only certain images with good clarity have been shown here in Table 15. Two extreme cases for Pier 13 and Pier 24 are shown in Figure 49. Image processing was performed using MATLAB's Image Region Analyzer tool. In order to quantify and detect the edges of cracks, image segmentation approach was used. In this approach, initially, the images were converted into binary images. The cracks and void structures to be segmented should differ greatly in contrast to the background. The gradient and threshold of the test images were calculated and applied to create a binary mask containing the segmented cracks and voids. In order to achieve these tasks, edge and Sobel operators were used. Detailed information on the image processing techniques is given in (Sankarasrinivasan et al., 2015 and Pragalath et al., 2018). Table 16 shows the damage computed using image processing. Note that the damage was quantified only for the piers due to the severe map cracking observed on the pier walls. Image processing for the deck and superstructure was not performed as from Table 14 it can be seen that no significant defects were found on the superstructure including the deck. The image processing results were used to assign condition ratings of the piers, as can be seen in Table 17. The condition rating was still assigned based on the guideline published by AASHTO (described earlier). The material defects given in the guideline were assigned to the bridge elements based on the condition state, as shown in Table 17.

Table 14: Representative photos of Deck and Superstructure of the bridge captured by UAV mounted camera

Span 1		**Span 12**		**Span 13**	
Side 	Bottom 	Side 	Bottom 	Side 	Bottom 
Span 16		**Span 17**		**Span 19**	
Side 	Bottom 	Side 	Bottom 	Side 	Bottom 
Span 21		**Span 22**		**Span 23**	
Side 	Bottom 	Side 	Bottom 	Side 	Bottom 
Span 24		**Span 25**		**Span 26**	
Side 	Bottom 	Side 	Bottom 	Side 	Bottom 

Table 15: Condition of Pier Walls (shown without and with image processing)

Pier 2		**Pier 12**		**Pier 13**	
Unprocessed	Processed	Unprocessed	Processed	Unprocessed	Processed
	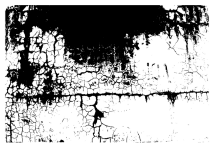				
Pier 16		**Pier 17**		**Pier 19**	
Unprocessed	Processed	Unprocessed	Processed	Unprocessed	Processed
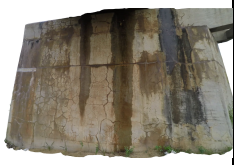			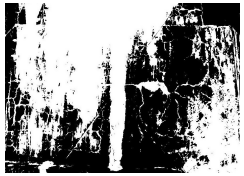		
Pier 21		**Pier 22**		**Pier 23**	
Unprocessed	Processed	Unprocessed	Processed	Unprocessed	Processed
					
Pier 24		**Pier 25**		**Pier 26**	
Unprocessed	Processed	Unprocessed	Processed	Unprocessed	Processed
	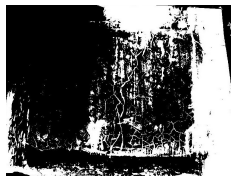		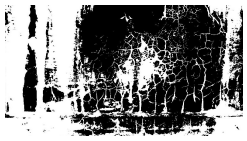		

Table 16: Damage calculation using Image Processing

Reinforced Concrete Bridge Deck																				
Element #	1-27																			
% Damage	No Significant Damage was observed																			
Prestressed Concrete Girder-Tapered I shape																				
Element #	1-27																			
% Damage	No Significant Damage was observed																			
Elastomeric Bearing																				
Element #	1-28																			
% Damage	No Significant Damage was observed																			
Sub Structure (Abutment (1, 28) and Pier Walls (2-27))																				
Element #	1	2	3-11	12	13	14	15	16	17	18	19	20	21	22	23	24	25	26	27	28
% Damage	38	44	-	42	62	59	51	56	57	48	45	37	50	35	35	34	48	53	-	31

Note- "-" = Not Assessed

Table 17: Unmanned Aerial Vehicle (UAV)-assisted AASHTO Guide Manual-based Condition Ratings

Element Description	**Condition State 1**	**Condition State 2**	**Condition State 3**	**Condition State 4**	**Defects**
Reinforced Concrete Bridge Deck	No defects have been observed	-	-	-	-
Prestressed Concrete Girder-Tapered I shape	No defects have been observed	-	-	-	-
Elastomeric Bearing	No defects have been observed	-	-	-	-
Concrete Abutment (Unreinforced)	-	Rust Staining (1120), Cracking (1010), and Deterioration (1220)		-	Average Area of Cracking and Rust Staining- 34%
Concrete Pier walls (Unreinforced)	-	-	Rust Staining (1120), Cracking (1010), Deterioration (1220), and Scour (6000)	-	Average Area of Cracking and Rust Staining- 50%, Scouring observed on Pier Walls 12, and 17
Masonry Piers Walls (Unreinforced)	-	-	Rust Staining (1120), Mortar Breakdown (1610), and Scour (6000)	-	Rust Staining and Area of Mortar Breakdown – 42%, Scouring observed on Pier Wall 25

Note: It should be noted that the defects code (example: Cracking (1010)) are obtained from the AASHTO guide manual

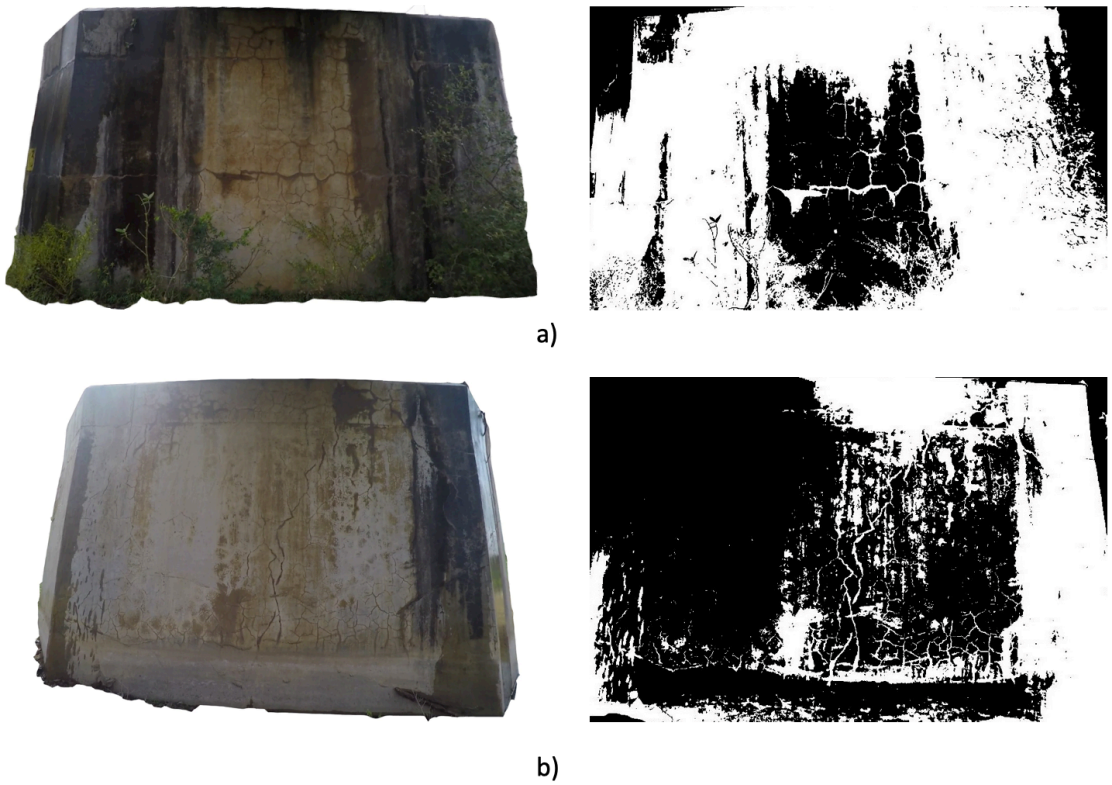

Figure 49: Damage quantification in the piers using image processing; a) Pier 13:62% damage and b) Pier 24:34% damage

The condition rating in Table 17 states that the substructure of the bridge is in poor condition with abutments having average area of cracking and rust staining of 34%, concrete pier walls have average area of cracking and rust staining of 50%, and masonry pier walls have rust staining and area of mortar breakdown of 42%. Figure 49 shows the most severe and the mildest damage on the pier 13 and pier 24 respectively. The superstructure including the bridge deck was found to be in good condition with no significant defects.

4.7 Comparison between the Visual inspection and UAV-based inspection

Both on-site visual inspection and UAV-based inspection were performed for the same spans of a long span railway bridge. Based on the information in Table 12 and Table 16, it can be seen that the reinforced concrete bridge decks, prestressed concrete girders, and elastomeric bearings have almost same condition states when compared using both the inspection methodologies. This is due to the fact that no major defects have been noticed on those elements. The comparison is made between the percentage damage calculated by image processing and visual inspection (human judgment) as can be seen in Figure 50. The positive difference shows an underestimation of the damage by visual inspection compared to the image processing, whereas, the negative difference shows overestimation. Note that the percentage of damage in piers/abutment differs significantly with an average percentage underestimation of 35% by visual inspection. However, in some cases, image processing overestimated the damage due to the presence of moisture (as can be noticed

from Table 15). For instance, for piers 21 and 24, the image processing overestimated the % damage by 50 and 41 respectively due to the moisture.

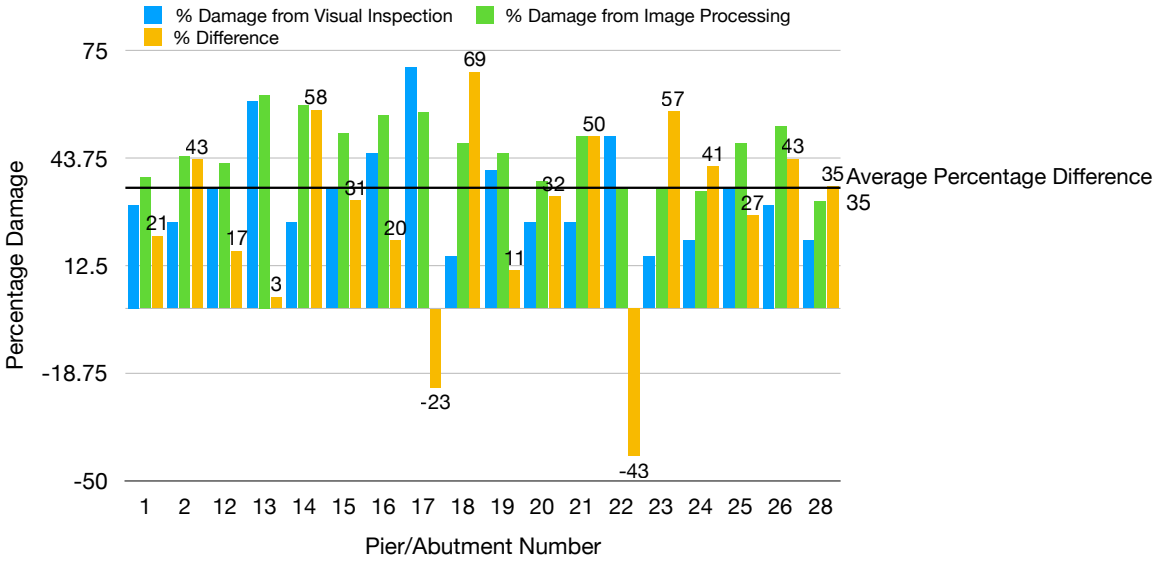

Figure 50: Percentage difference in the damage of piers from Visual inspection and Image Processing

Note that the moisture accumulation may not be significantly detrimental to material degradation at the current state. However, these regions can lead, in the long term to rapid material degradation. The authors re-evaluated the other extremes (% damage difference (Underestimation or overestimation) more than 40) as well. However, it was found that the condition rating given during visual inspection was a relative judgment looking at the condition of other piers. This was the main reason for the introduction of the error during visual inspection.

In addition to the technical accuracy, the time it took for visual inspection compared to the UAV-based inspection was significantly different. The authors took about 5 hours to visually inspect all the spans (shown in Figure 48) and assign condition state for different elements of the bridge. On the other hand, using the UAV system, the same spans of the bridge were inspected in about 1 hour plus another 2 hours of image processing and condition state assignment time. However, this does not include the prep time to assemble the drone on site, mounting the batteries and the back-end work such as charging of batteries, and other usual maintenance tasks. Other unquantified differences between the two methodologies include ease of inspection, cost of the inspection, compromise of safety, and access to inaccessible elements of the bridge. UAV-based methodology integrated with image processing tool and AASHTO guideline has outperformed the visual-based inspection in all the parameters mentioned above. The visual inspection was found less sensitive to weather elements such as wind and rain (including existing moisture condition) compared to the use of UAV system as the UAV system is more sensitive to extremely windy and rainy conditions (more details are given in Dorafshan et al., 2017). Furthermore, the UAV System used cannot clean up surfaces that a visual inspector could clean before taking a photo of the true condition of the element inspected.

4.8 Conclusions

This paper highlights the outcomes of two inspection methodologies applied on a long span railway bridge and compares the findings of the two. Out of a total 28 spans, a total of 19 spans (more than 60 elements) were inspected and more than 200 images processed. It has been found that the new technique (IPA) proposed by the authors could improve inspection accuracy, save time, and save cost. However, the use of a UAV system is very sensitive to external weather condition, a UAV cannot clean up the surfaces that a visual inspector could clean before taking a photo, and the areas where the GPS satellites are not available, a UAV is challenging to fly. Following are some of the specific conclusions that can be drawn from this study:

1. The damage identified by visual inspection underestimated the average damage in piers and abutments by 35% compared to the image processing.
2. In some cases, image processing introduced error due to the presence of moisture. For example, image processing results for piers 21 and 24 overestimated the damage due to the presence of moisture.
3. The visual inspection performed by authors took about 5 hours whereas, UAV-based inspection took about 3 hours including back-end image analysis. However, the visual inspection results were available as soon as the inspection was completed. Whereas, the images collected using the drone system had to be analyzed later.
4. Condition States Comparison between the Visual method and IPA show that there is no major difference in the rating of the reinforced concrete deck, prestressed concrete girder, pier walls, and elastomeric bearings. However, the condition rating of abutments from the visual inspection was found to be in Condition state 3 (Poor) while from image processing, it was found to be in Condition state 2 (Moderate).

4A: Multi-device Robotics-based Sensor Data Acquisition System for Mapping and Assessing Defects in Infrastructure

Harsh Rathod[1], and Rishi Gupta[2]

[1]PhD Student, Department of Civil Engineering, University of Victoria, Victoria BC, Canada, email: hmrathod@uvic.ca

[2]Associate Professor, Department of Civil Engineering, University of Victoria, Victoria BC, Canada, email: guptar@uvic.ca

Note: This section is adapted in part from submitted work (Rathod et al., 2019: Licensed to HRG Infrastructure Monitoring Inc.) in the United States Patent and Trademark office with permission where appropriate. The section outlines a patent pending multi-device robotics-based sensor system to acquire and analyze the inspection data. The data is collected using a UAV system in three layers to obtain a condition rating of civil structures.

Background and Problem Statement

There are several NDT techniques (both contact and non-contact) that are currently being used to map cracks, corrosion, and delamination on bridge decks. Standard practice in the field for identifying cracks, corrosion, and other surface defects currently relies on human visual inspection and judgment, which is subjective, prone to errors, and can be unreliable. The means of accessing various substructures of bridges can also be limited and difficult, as workers currently rely on a combination of snooper trucks, scaffoldings, ladders, cranes, and helicopters to conduct visual inspections. Some of the popular techniques in the field for detecting delamination include Ground Penetrating Radar (GPR), Infrared Thermography, Chain-drag, and other stress wave methods. GPR is an accurate method for mapping delamination, but it requires lane closures during the inspection and makes it difficult to inspect the underside of a bridge deck. The non-contact nature of Infrared Thermography makes it very useful in mapping delamination in a bridge deck without requiring lane closures. However, the method is highly sensitive to climatic conditions (mainly temperature and wind). The Chain-drag method is the most widely used technique due to its simplicity and lower cost. However, the current practice involves human judgment. The other major drawbacks of this technique are its inability to inspect any bridge deck elements on the underside of the bridge, as well as the many hours of manual labor required.

The proposed invention has the advantages of improved reliability and speed in detecting multiple defects, through the use of multiple devices and techniques in a single integrated system that can operate without requiring lane closures. The novel defect mapping system also provides improved accessibility, as it can be hosted on many different types of robotic devices, including (but not limited to) Unmanned Aerial Vehicle (UAV) and rover technology. The proposed invention utilizes a versatile hardware system, capable of integrating multiple layers of data from a combination of devices (an optical camera, an infrared camera, an acoustic sensor and laser measurement devices), to automatically map bridge defects and quantify the structural damage using proprietary software (see Figure 51).

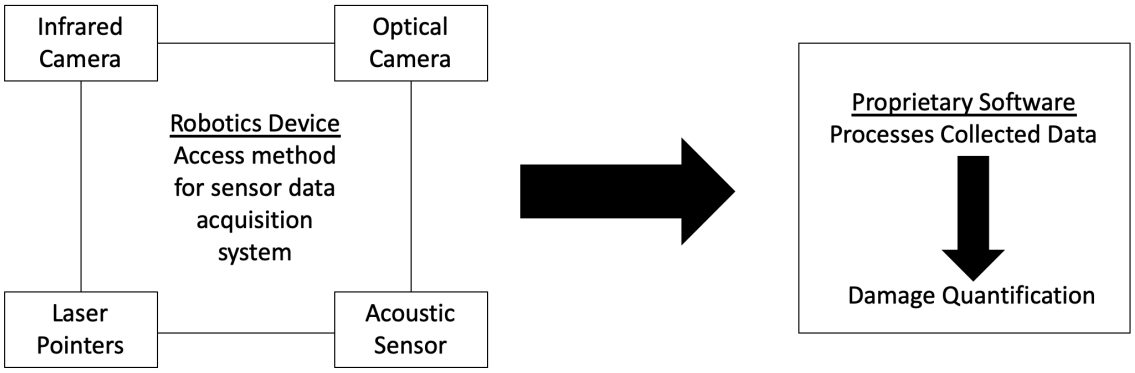

Figure 51: Diagram of invented sensor data acquisition system (indicating hardware components hosted by a robotic device) and invented data analysis and damage quantification software

Brief Description of the Invention

The invention disclosed here is a novel robotics-based measurement technique – employing the use of the optical camera, infrared camera, laser measurement system and sound/acoustic measurement technique – for mapping/identifying cracks, corrosion, and delamination in reinforced concrete slabs. The innovation/novelty lies in the integration of the multiple hardware devices and data acquisition techniques within a single robotics system, as well as the newly developed/invented software for processing the multiple layers of data and quantifying the structural damage. The existing prototype utilizes a UAV to access bridge decks with the sensor data acquisition system installed and activated. Note that UAV technology is just one possible means of deploying the sensor data acquisition system and accessing bridge decks, but the innovation is not limited to UAV technology.

Using the proposed invention, bridge inspection is conducted with the integrated robotics and sensor data acquisition system:

1. The inspection involves capturing high resolution optical and infrared video/images of all concrete surfaces (the top, side, and underside of the bridge deck) and using sounding/acoustic data acquisition for detecting delamination, and the laser measurement system is used to measure crack dimensions at each potential area of concern.
2. The acquired data is processed by the developed proprietary software as it is collected (frequently and in real time) and areas of possible defects are mapped, based on any surface cracks identified via image recognition that exceed the established threshold of tolerance.
3. Once the inspection is completed, all four of the collected data layers are processed by the developed proprietary software, and the overall damage is quantified (as well as the damage of individually assessed subcomponents). The software produces a final comprehensive map for the defects identified and quantified from all the integrated data layers. Figure 52 outlines one possible method of applying the developed technique on a structure to identify any defects.

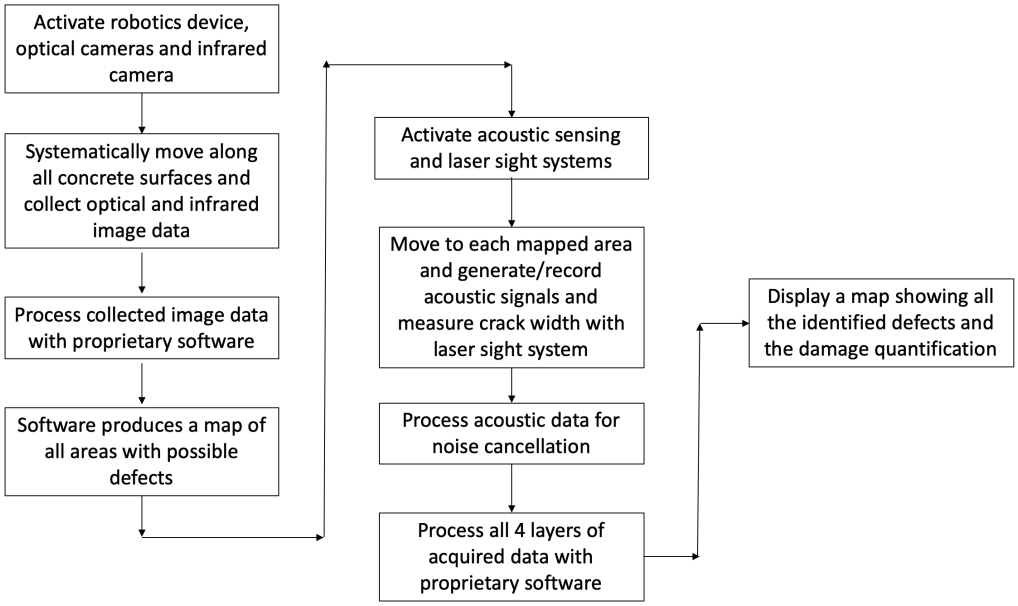

Figure 52: Flowchart outlining the process of applying the integrated robotics and sensor data acquisition system and software quantification for mapping and assessing structural defects

The integrated sensor data acquisition system has a number of configurations available, which allows access to a variety of surfaces such that bridges can be effectively mapped. Although a variety of different types of robotics can be used, the configurations for the existing UAV prototype hardware components are described below:

1. Optical Camera

The primary (built-in) optical camera is situated on a gimbal at the bottom and lateral center of the UAV. The gimbal allows for multiple viewing angles, supporting optical inspection of top and side surfaces of bridge decks. The designed prototype also supports a configuration for a secondary optical camera, situated at the top of the UAV, facing upwards (see Figure 53). This allows for optical inspection of the underside of bridge decks.

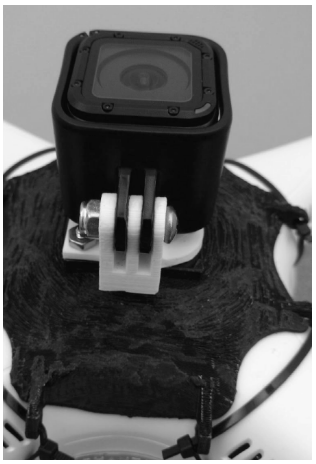

Figure 53: Upward facing optical camera for inspecting the underside of bridge decks

2. Infrared Camera

The infrared camera is positioned in line (laterally, at the same height) with the primary optical camera. The two cameras are 10 cm apart for the current prototype. The infrared camera has two possible orientations: facing forward and facing down.

3. Laser Measurement System

The laser measurement assembly currently consists of two laser pointers (but can incorporate numerous alternative laser measurement devices), each one situated equidistantly from the center of the UAV, fixed at the front of each of the UAV's landing gears (the inner sides of the lower payload assembly). Refer to Figure 54 for one possible configuration of the laser measurement assembly, as well as the forward-facing infrared camera and a primary optical camera.

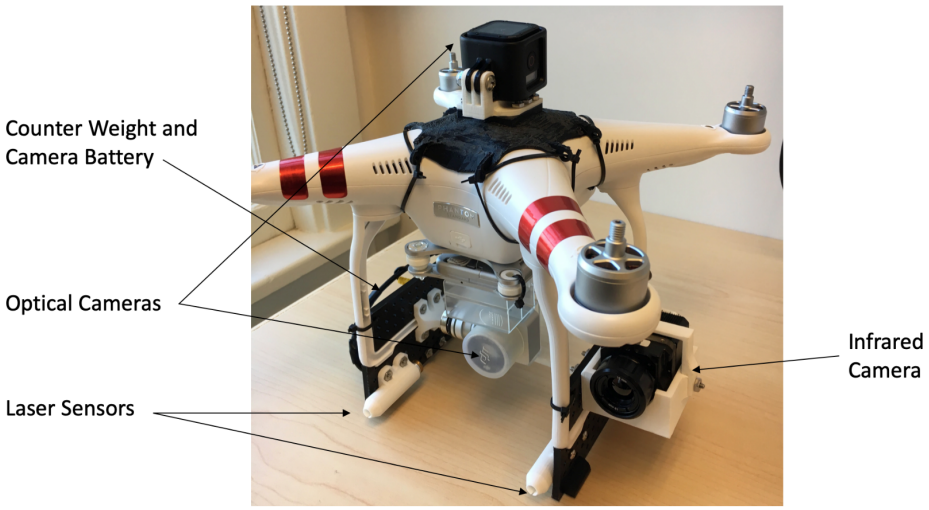

Figure 54: One possible configuration for the existing integrated sensor data acquisition and UAV prototype (laser assembly, primary optical camera and forward-facing infrared camera)

4. Acoustic Assembly

Some of the possible configurations for the acoustic assembly are detailed in section 4B of this chapter.

4B: UAV-based Acoustic Technique for Mapping Defects in Civil Infrastructure

Harsh Rathod[1], and Rishi Gupta[2]

[1]PhD Student, Department of Civil Engineering, University of Victoria, Victoria BC, Canada, email: hmrathod@uvic.ca

[2]Associate Professor, Department of Civil Engineering, University of Victoria, Victoria BC, Canada, email: guptar@uvic.ca

Cross-reference to related application

This application claims the benefit of U.S. Provisional Application No. 62/666,512, filed May 3, 2018, which is hereby incorporated by reference in its entirety.

Field

The disclosure pertains to inspection of bridges and other structures.

Note: This section is adapted in part from submitted work (Rathod et al., 2019f: Licensed to HRG Infrastructure Monitoring Inc.) in the patent under the Patent Cooperation Treaty (PCT) with permission where appropriate. It highlights a novel inspection apparatus that comprises of a UAV and an acoustic signal generator coupled to the UAV to detect and quantify subsurface defects. The acoustic signal generator includes a hammer having a contact surface situated with respect to the UAV to be movable by the UAV to produce an acoustic signal in a structure.

Acknowledgement: Inventors acknowledge the help from Mr. Sean Blaney in collecting acoustic data using a UAV.

Abstract of the disclosure

Unmanned Aerial Vehicles (UAVs) are provided with hammers having contact surfaces to produce acoustic signals in structures to be inspected. By selecting a suitable flight path, the contact surface can be dragged across or tapped against the structure to produce acoustic signals indicative of structure condition. Acoustic detectors are coupled to the UAV to produce detected acoustic signals that can be stored, communicated, and/or processed to access to arbitrary structure surfaces, including bottom surfaces of bridge decks and to locate delamination.

Background

While many bridge defects are of concern, one of the most common defects found in bridges including reinforced concrete bridge decks is delamination. Several NDT techniques, both contact and non-contact, have been used to map delamination. Typical methods include Ground Penetrating Radar (GPR), Infrared Thermography, chain drag, and other stress-wave methods. GPR is a very accurate method for mapping delamination, but requires lane closures during the inspection and is not convenient for inspecting the bottom of a bridge deck. The non-contact nature of Infrared Thermography makes it useful in mapping delamination in a bridge deck without requiring bridge closure. However, this method is sensitive to climatic conditions such as temperature and wind. The chain drag

method is the most widely used technique due to its simplicity and low cost. This method uses an acoustic signal processing unit to accurately map delamination. Unfortunately, this technique does not permit inspection of a bridge deck element from the bottom side. Improved approaches are needed.

Summary

Some examples are described below, and the features of any of these examples can be used in other situations as well. In one example, methods include positioning an acoustic signal generator with respect to a selected region of a structure with an unmanned aerial vehicle (UAV). The acoustic signal generator is connected to the UAV, and an acoustic signal is coupled into the structure at the selected region using the acoustic signal generator. With an acoustic detector connected to the UAV, at least one acoustic signal received from the structure is detected that is responsive to the acoustic signal coupled to the structure. In some examples, the detected acoustic signal is transmitted to a ground-based receiver. In typical embodiments, the detected acoustic signal is processed to identify one or more portions of the structure as having a structural anomaly. In representative examples, the acoustic signal generator includes a hammer having a contact surface, and the UAV is moved so that the contact surface of the hammer contacts a surface that is acoustically coupled to the selected region of the structure. In some approaches, the acoustic signal is coupled into the structure by dragging the contact surface of the hammer with the UAV. According to some implementations, the hammer is a ball end that is stiffly coupled to the UAV.

In still further examples that can be combined with any other examples, the acoustic signal generator includes a hammer such as a ball end having a contact surface, and the UAV is moved so that the contact surface of the hammer taps a surface that is acoustically coupled to the selected region of the structure. For convenience, the hammer can be coupled to the UAV with a spring. According to representative alternatives, first and second acoustic signals are detected with first and second acoustic detectors connected to the UAV, respectively, wherein the first and second detected acoustic signals are responsive to the acoustic signal coupled to the structure. A difference signal is obtained based on the first and second detected signals, and one or more portions of the structure are identified as having a structural anomaly based on the difference signal. In some cases, an acoustic detector is situated at least 1 m from the UAV.

Inspection apparatus comprises a UAV and an acoustic signal generator coupled to the UAV. The acoustic signal generator includes a hammer having a contact surface situated with respect to the UAV to be movable by the UAV to produce an acoustic signal in a structure. An acoustic detector is coupled to the UAV and situated to receive acoustic signals from the structure in response to the acoustic signal produced in the structure. In some examples, the hammer comprises a ball end that can be secured to the UAV with a spring. An audio recorder can be coupled to the acoustic detector and configured to produce digital audio signals based on the acoustic signals received by the acoustic detector. In particular examples, a transmitter is coupled to audio recorder and operable to wirelessly transmit the digital audio signals. In some examples, a processor is fixed to the UAV and coupled to produce at least one spectrum based on the digital audio signals.

Additional features of any of the disclosed examples include that the acoustic detector comprises first and second acoustic detectors situated to have substantially the same

acoustic coupling to the UAV and substantially different acoustic couplings to the contact surface of the hammer and/or the structure under inspection. The audio recorder can be coupled to produce digital audio signals based on a difference between detected audio signals from the first and second detectors, and the audio processor can produce the at least one spectrum based on the difference.

In a specific example (which may also include any or all of the features described above), methods comprise moving a hammer with an unmanned aerial vehicle (UAV) so as to drag a contact surface of the hammer or tap the contact surface of the hammer on a region of a surface of a structure to apply an acoustic signal to the structure. At least one acoustic signal from the structure produced in response to the applied acoustic signal is detected with at least one microphone that is secured to the UAV. Based on a spectrum of the detected acoustic signal, a location of a structural defect in the structure is indicated.

Inspection apparatus comprise a UAV and a hammer connected to the UAV. At least one microphone is secured to the UAV and an audio recorder is coupled to the at least one microphone to receive an acoustic signal from a structure produced in response to dragging or tapping the contact surface of the hammer on the structure. A corresponding digital acoustic signal is stored in a computer readable medium, and a processor is coupled to receive the digital acoustic signal, reduce UAV noise in the digital acoustic signal, and produce at least one spectrum associated with the noise-reduced digital acoustic signal. A structural defect such as delamination is identified based on the spectrum or otherwise based on the noise-reduced digital acoustic signal.

The foregoing and other features and advantages of the disclosed technology will become more apparent from the following detailed description, which proceeds with reference to the accompanying figures.

Detailed description

The disclosure pertains to methods and apparatus for inspection and evaluation of bridges and other structures. In typical examples, Unmanned Aerial Vehicles (UAVs) are used to permit access to arbitrary surfaces of a structure under evaluation. However, the use of UAVs is optional and the disclosed approaches can be implemented in other ways. In some examples, steel ballpoints or other devices are placed into contact with a region of interest in a structure undergoing the test. Other devices can be used, such as metal pieces of other shapes, stone, or ceramics or other materials preferably robust enough to be used to contact a surface periodically. Steel balls or other hard metallic shapes are convenient. Spherical or curved shapes are not required but can be advantageous. Objects situated to tap a surface, drag across a surface, or otherwise interact with a structure or a surface of stricture are referred to as “hammers’ herein. UAVs are controlled so that hammers contact a surface associated with the structure to be inspected. Typical contacts are referred to as “tapping” in which a single contact or series of contacts are applied or “dragging” in which a hammer surface is urged into contact with the surface while being moved across the surface. The associated methods are referred to as a “tap” or “tapping” method and a “drag’ or dragging” method.

As used herein, “acoustic signals” generally refers to propagating sound waves while “detected acoustic signals” refers to corresponding electrical signals produced with an acoustic detector such as a microphone, a piezoelectric transducer, or other sound detector. Examples are described with reference to acoustic detectors, but it will be appreciated that

in typical frequency ranges of interest (less than about 5-10 kHz), microphones are particularly convenient due to their wide availability and low cost, but other acoustic detectors can be used. In many examples, time-domain acoustic signals are Fourier transformed (such as with an FFT) to produce signal spectra in a particular time window or as a function of time. “Detected signal” also refers to a digital representation such as stored in a computer-readable medium, usually by directing time-varying detected acoustic signals (i.e., a time-varying electrical signals) to an analog-to-digital converter (ADC). A detected acoustic signal from a single detector is referred to in some examples as a single channel signal, as it can be convenient to record acoustic signals from a structure under inspection using a stereo (2-channel) audio recorder to permit obtaining a difference signal using two or more acoustic detectors.

Some embodiments are described with reference to inspection of bridge decks. This is merely a representative example, and other structures and other components of structures can be similarly evaluated such as bridge piers, abutments, girders or components of dams, power plants, and buildings. The disclosed methods and apparatus can be used with any surface or structure for which acoustic signal based inspection is intended, and the disclosed approaches permit inspection of arbitrary surfaces (tops, sides, interiors, bottoms) that are accessible with a UAV. Various kinds of defects can be detected such as delamination and subsurface defects such as cracks, voids, corrosion, and debonding, and inspection for delamination is only as a representative example.

Example 1

Referring to Figure 55a, a structure test apparatus comprises a UAV to which one or more cameras are secured. A steel ballpoint is secured to the UAV with a connector such as a rigid or stiff rod. The ballpoint is thus flexibly coupled to the UAV but stiffly enough to be urged against a test surface. As the acoustic transducer is secured to the steel ballpoint and is electrically coupled to the UAV with a cable. In Figure 55a, the steel ballpoint is positioned proximate a surface of a structure such as a bridge deck. The UAV is manipulated so that the steel ballpoint contacts the surface so as to either tap the surface or to drag the steel ballpoint across the surface. An acoustic signal is produced in the structure, and portions returned from the structure are received by the detector, and the detected (electrical signals) are coupled to the UAV for transmission to a fixed location or are processed at the UAV. Figure 55b illustrates the apparatus of Figure 55b in a position so that the steel ballpoint contacts a side surface of a substrate. In Figure 55c, the apparatus is positioned so that the steel ballpoint contacts a bottom surface of a substrate. In this example, the UAV flies below the structure and is then directed upwards to provide contact.

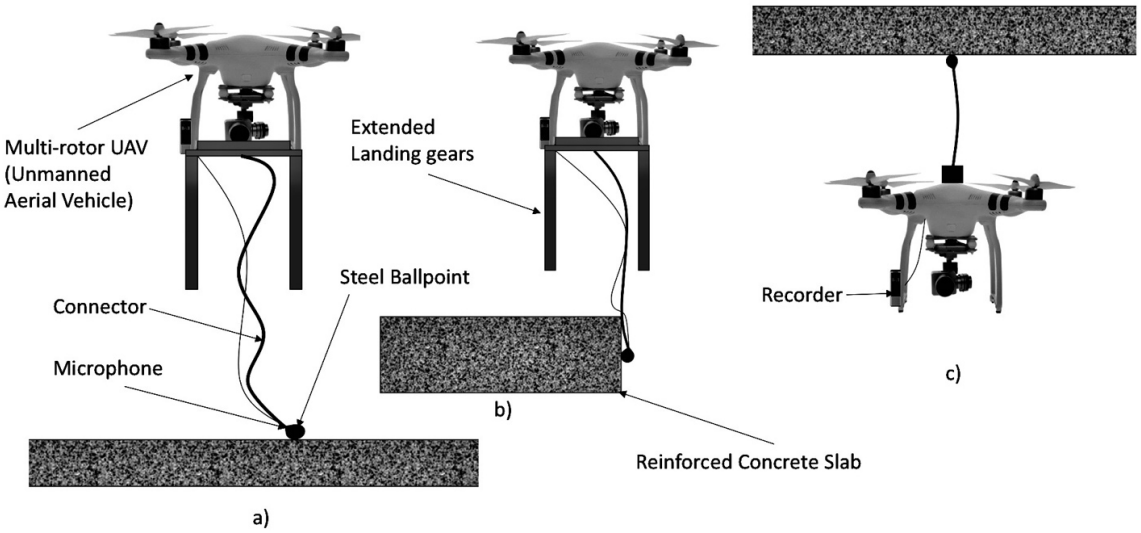

Figure 55: UAV-based acoustic data collection on an upper surface of a bridge deck, on a side of a deck slab, and on bottom surface, under the deck slab, respectively.

The connector that couples the steel ballpoint to the UAV can be metallic and have suitable stiffness to remain substantially fixed with reference to the UAV but suitably flexible so that contact can be maintained in the presence of changes of surface topography. In apparatus that include a connector such as the connector, an object that is to contact a surface of a structure (such as a steel ballpoint) it typically dragged over the surface by movement of the UAV. In some cases, the object is made to tap the surface (often repetitively). Using either a drag or tap method, an acoustic signal is produced in the structure under test.

Example 2

Figure 56a shows a representative test apparatus that includes a UAV have a transmitter/receiver for data communication with fixed transmitters and receiver, a memory that stores computer-executable instructions for data collection, processing, and communication, and an acoustic recorder that receives acoustic signals and processes (with, for example, one or more amplifiers and filters), and then converts the acoustic signals to digital signals using an A/D converter. In general, recorded (i.e., digital) data signals are further processed to produce superior structure evaluations, but for convenience herein, both analog and digital acoustic signals are referred to simply as “acoustic signals.” A processor can be coupled for noise reduction, digitization, filtering, Fourier transformations or other operations on the digital acoustic signal. The processor can be implemented as a CPU, a gate array such as an FPGA, or other processing hardware. In some example, recorded data is transmitted for remote processing, and additional processing is not done at the UAV.

Figure 56: An apparatus that deliver acoustic signals to a structure for structure evaluation and illustration of placement of acoustic detectors (length -180 cm) to reduce UAV noise in a difference signal.

A contact assembly is secured to the UAV with the first end of a spring or other flexible member. A second end of the spring is fixed to a plate. An extension such as a metal rod or other rigid element is coupled to the plate and to a contact element. The contact element can have a spherical, cylindrical, planar, or another shaped contact surface. One or more cameras can be secured to the UAV, and one or more acoustic transducers are situated to receive acoustic signals from a substrate under test that is produced in response to contact with the contact surface.

In use, the UAV is flown to urge the contact surface against a surface of a structure (or another surface that couples acoustic signals to the structure under test). Typically, the UAV repetitively contacts the structure with the contact surface and responsive acoustic signals are detected by one or more of the acoustic detectors and coupled to the recorder with respective cables such as cable. While either a drag or tapping method can be used to produce acoustic signals with the contact surface, the configuration of Figure 56a is typically used to tap a surface of a structure. As discussed below, it can be desirable to have a distance from the UAV to the plate and/or from representative UAV rotors sufficient so that rotor noise contributions are diminished. In addition, the placement of multiple acoustic detectors can be arranged to reduce UAV noise contributions. In addition, some of the other techniques that can be used to reduce or account for noise include use of directional microphones, measuring the external traffic noise separate from the UAV system (for subsequent cancelation), and using a previously recorded rotor acoustic pattern with a single microphone mounted on the UAV. The contact assembly is shown secured to a side of the UAV opposite the rotors but can be placed on the same side in the box as shown in the box defined with dotted lines.

Example 3

Referring to Figure 57, a representative method includes moving a contact assembly to a location of interest at with a UAV and generating an acoustic signal in a structure to be

tested at, generally by dragging a hard object across the surface or tapping the surface with a hard object using the UAV. Acoustic signals from the structure are detected and recorded, typically, by storing in a computer readable memory. Noise contributions to the recorded acoustic signals are reduced, and, acoustic signals having magnitudes greater than a user-adjustable or predetermined threshold are identified and areas associated with damage are marked while areas appearing satisfactory are marked as safe or acceptable. If additional areas are to be inspected as determined, the process returns to initiate an inspection of a different area or re-inspection of a previously inspected area. Upon completion or during processing, a map of identified defects (on non-defective areas) can be displayed as indicated. In some examples, signal magnitudes are referenced to a signal magnitude associated with the initial contact with the structure so that signal variations due to differences in tapping or dragging are reduced. In typical examples, structure defects are identified by examination of spectral peaks.

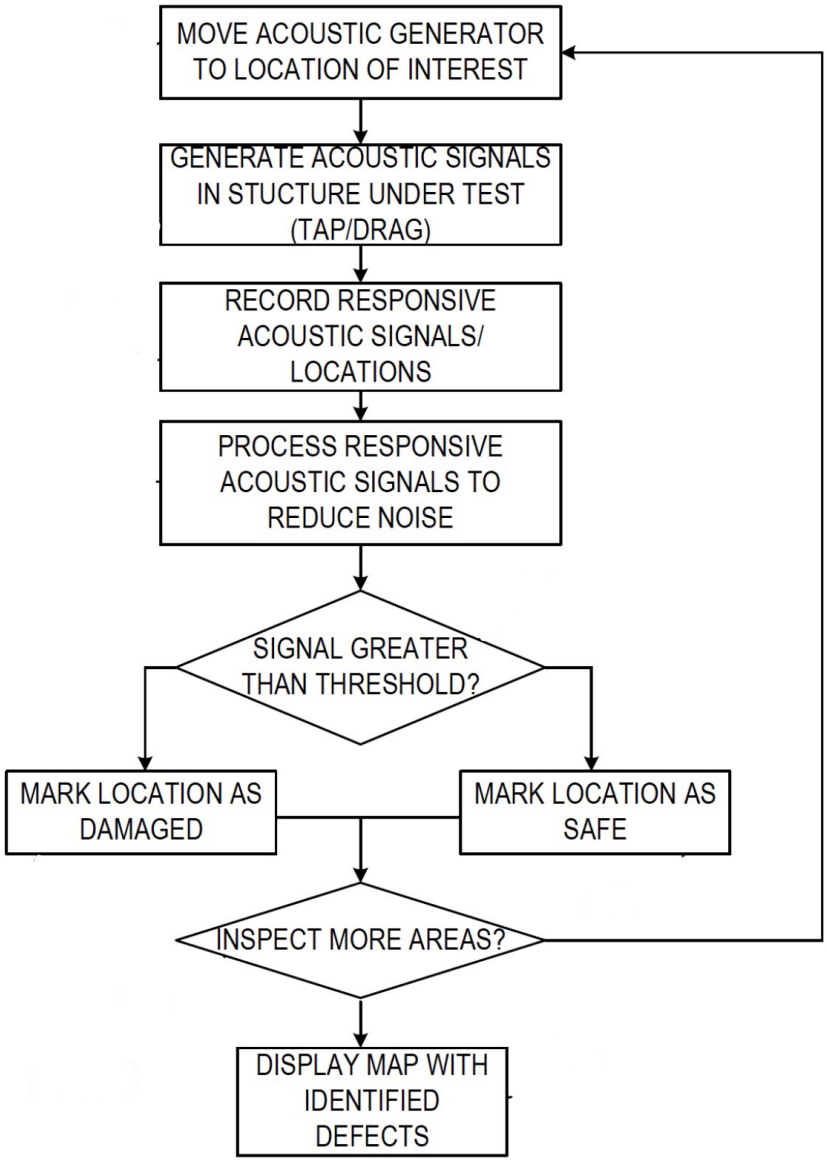

Figure 57: Flowchart showing a method of mapping defects in a bridge or other structure

Example 4

A UAV used to transport a contact assembly can generate acoustic noise which is preferably eliminated or reduced using one or more of the following approaches, or a combination thereof. A distance between the UAV and the acoustic detectors can be made sufficiently large to reduce UAV signal contributions, a difference signal can be obtained to compensate UAV noise, and/or the detected signals can be processed based on a noise profile and Fourier transformed or filtered as discussed below. For example, acoustic detectors can be situated at distances of 0.5 m, 1.0 m. 1.5 m, 2.0 m, 3.0 m or more from a UAV, generally by connecting a striking surface of a hammer to the UAV with a sufficiently long connector.

Example 5

A difference-signal based approach to reducing noise in detected audio signals is illustrated in Figure 56a. A ball is secured to a mounting plate that is coupled to a UAV with a spring. Acoustic detectors are situated with different lateral displacements with respect to the ball but at substantially the same distance from the UAV. In one example, acoustic detectors are situated at 25.4 mm and 50.8 mm lateral distances from the ball. As a result, the acoustic detectors, receive substantially the same acoustic signal from the UAV but receive signals of different magnitudes from a test structure in response to tapping, dragging, or another contact with the ball. Detected acoustic signals from the acoustic detectors are coupled to respective amplifiers and/or filters and A/D converters. Digitized acoustic signals are stored in a memory. The digital acoustic signals are processed to produce a difference signal using processing hardware in the UAV or provided in an audio recorder. The difference signal will tend to reduce noise that is common to both acoustic detectors. In this example, the difference signal is produced digitally, but in other examples, an analog difference signal can be used as provided by, for example, a differential amplifier. Although not shown, in many examples, multiple detected acoustic signals are acquired and averaged to reduce noise. Results obtained with difference-based noise reduction with acoustic signals at delamination are shown in the spectral plots of Figure 58. A curve corresponds to a detected signal from a single transducer while the curve is a spectrum associated with a difference signal. Acoustic transducers situated so that UAV generated noise signals are within about 10%. 5%, 2%, 1%, 0.5%, or less are referred to herein as being substantially equidistant. Two acoustic transducers situated so that acoustic signals from a substrate differ by 10%, 20%, 25%, 50%, or more are referred to herein as being at substantially different distances. In producing difference signals, the electronic gain can be adjusted so that UAV noise reduction is improved.

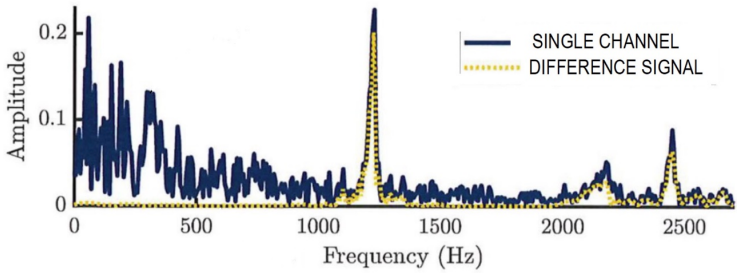

Figure 58: Illustration of noise reduction in a detected acoustic signal using two acoustic detectors to produce a difference signal

Example 6

Referring to Figure 59a-c, in another approach, acoustic signals are recorded in response to contact with a surface of a structure under inspection. Figure 59a illustrates spectra of a single acoustic channel as a function of time. Contact/impact with a structure to be inspected occurs at about t = 7.5 s; the acoustic signal spectra prior to this time corresponds to background noise, generally UAV noise. Spectra as a function of time for a difference signal (two acoustic detectors) are shown in Figure 59b; background noise is reduced but is still apparent. To further reduce noise, a section of the pre-contact acoustic signal (tapping method) or a section of the acoustic signal not associated with a defect (drag method) can be is used to generate a spectral noise profile and this spectral noise profile is then applied. Figure 59c illustrates spectra as a function of time for a different signal for which a noise profile has been used to further reduce noise. Noise contributions are removed, and spectra associated with contact remain. Noise-reduced spectra as shown in Figure 59c simplifies the identification of defects in the structure under evaluation. In the example of Figure 59c, approximately 0.5 s of the acoustic difference signal was used to obtain the spectral noise profile. Figure 59c shows a structure defect at a contact location at about t = 7.5 s. Location is established based on a starting contact location and a velocity at which the UAV is moved across the surface of a structure. In any of the above methods, spectral filtering can be used. For example, signal contributions at frequencies above about 4 kHz (in this example) can be removed with a spectral filter.

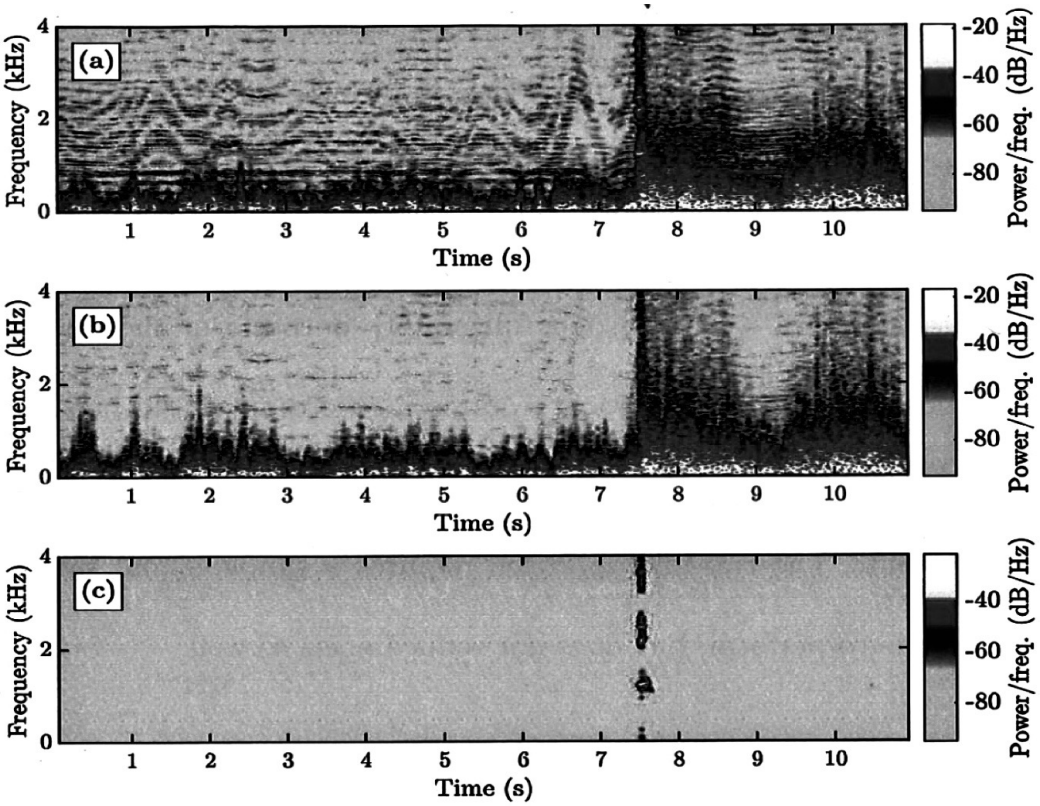

Figure 59: Spectrograms of a recording of an impact/drag above the defect (delamination): a) no noise reduction, b) dual mono-mic noise reduction, c) Audacity spectral noise gating noise reduction

Example 7

Figure 60a-b illustrate unprocessed detected acoustic signal data (single channel) obtained by a drag test (Figure 60a) and a tap test (Figure 60b) in the evaluation of a concrete slab that includes voids. Figure 60c-d show corresponding spectra. For reference, Figure 61a-b illustrate unprocessed detected acoustic signal data obtained by a drag test (Figure 61a) and a tap test (Figure 61b) in the evaluation of a control concrete slab without voids. Figure 61c-d show corresponding spectra. As shown in Figure 60c and Figure 61c, delamination is associated with wider spectral spreads in response to a drag test. The wider spectral spread is evident in Figure 60c which has a frequency spread approximately between 0-3 kHz with a spike exceeding 4 kHz matching a location of a defect. In contrast, Figure 61c indicates a narrower spread between 0-2.5 kHz.

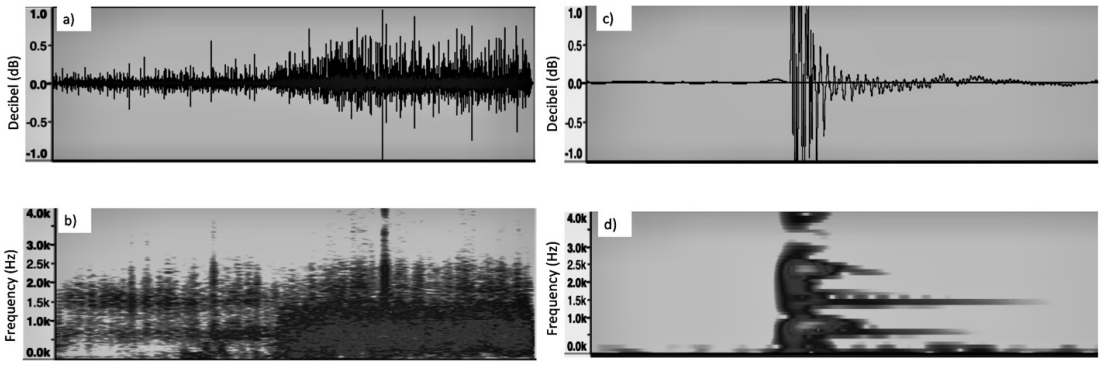

Figure 60: Unprocessed acoustic data collected from a slab with voids: a) acoustic signal - drag test b) frequency spectrum - drag test c) acoustic signal - tap test and d) frequency spectrum - tap test

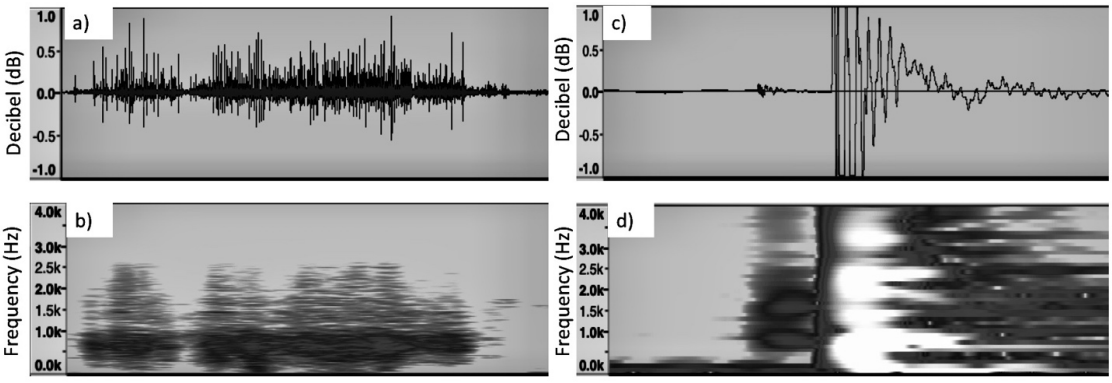

Figure 61: Unprocessed acoustic data collected from the control slab: a) acoustic signal - drag test b) frequency spectrum - drag test c) acoustic signal - tap test and d) frequency spectrum - tap test

Example 8

To inspect an upper surface (such as a top surface of a deck), a UAV system is controlled to maintain a flight path that is parallel to the surface. A constant distance of about 5 m to 10 m above a location of interest on the upper surface can be used, depending on a length

of a connector that couples the hammer to the UAV. During the flight, the UAV then drags the hammer across the surface and acoustic signals are detected and stored. Inspection using a lower surface (such as a bottom surface of a deck) can be similar, with the UAV controlled so that the hammer is in contact with the lower surface. Using a UAV-based inspection system, a lower surface can be readily inspected and inspection can be no more difficult than inspection of an upper surface. Moreover, for bridge inspections, because the UAV is below the deck, it is not necessary to restrict access to or close the bridge or one or more lanes to traffic. To inspect a side (vertical) surface, the UAV is directed along a flight path that is parallel to the surface while keeping the hammer in contact with the surface. While flight paths are referred to as parallel, flight paths can vary considerably if surfaces that are non-planar are to be inspected. In some cases, a connector is flexible enough so that a parallel flight path maintains contact even for non-planar surfaces.

Example 9

Methods for processing detected acoustic signals include placing acoustic detectors at to permit differencing to reduce UAV noise. One or more acoustic signals are acquired from one or more acoustic detectors. Signal noise is reduced by applying one or more processes from a library such as filtering, obtaining a difference signal, or processing with a spectral noise profile. One or more location are identified, typically based on spectra associated with the noise-reduced signal.

Example 10

An apparatus for structural evaluation includes a UAV having representative rotors and includes a transceiver for sending and receiving measurement data associated with structure assessment as well as communications associated with UAV path and UAV control generally (including flight path). A memory is coupled to store measurement data and processor-executable instructions for UAV operation and structure assessment and is in communication with a processor. An audio or other acoustic receiver is coupled to an acoustic transducer that is secured to an actuator. A hammer has a contact surface for tapping or dragging on a structure is operably connected to the actuator so that the hammer is movable in directions indicated by an arrow. The actuator can be secured to the UAV with an extension such as a post or other object so that the acoustic detector is sufficiently distant from the rotors to reduce noise in detected acoustic signals. Additional acoustic detectors can be used as discussed above. If desired, the memory can be coupled to store noise characteristics to aid in noise removal or attenuation in acoustic signal measurements. An electromagnetic actuator such as a push or pull type actuator which is operable to tap the contact surface against a selected surface can be used, or any other type of actuator such as a piezoelectric actuator. The actuator is typically operated in response to control signals provided by drive circuitry or other actuator drive components as controlled by the processor. Use of an actuator permits control of a tap rate by the processor, and the UAV is navigated to be within the range of a surface of interest with an extension provided by the actuator.

An actuator is mounted on a shaft or other extension from a UAV, but in other examples, the actuator can be secured directly to the UAV, and an extension used to distance a hammer and an acoustic detector. An extension is not required. As discussed previously, detected acoustic signals can be processed on board the UAV, transmitted without

processing, or noise-reduced and then transmitted for further processing. In some cases, two acoustic signals or a differential acoustic signal are transmitted, or an acoustic noise signal recorded during, prior, or after an acoustic signal used for inspection is acquired is transmitted for remote noise reduction.

Additional General Considerations

As used in this application and in the claims, the singular forms "a," "an," and "the" include the plural forms unless the context clearly dictates otherwise. Additionally, the term "includes" means "comprises." Further, the term "coupled" does not exclude the presence of intermediate elements between the coupled items. The systems, apparatus, and methods described herein should not be construed as limiting in any way. Instead, the present disclosure is directed toward all novel and non-obvious features and aspects of the various disclosed embodiments, alone and in various combinations and sub-combinations with one another. The disclosed systems, methods, and apparatus are not limited to any specific aspect or feature or combinations thereof, nor do the disclosed systems, methods, and apparatus require that any one or more specific advantages be present or problems be solved. Any theories of operation are to facilitate explanation, but the disclosed systems, methods, and apparatus are not limited to such theories of operation.

Although, the operations of some of the disclosed methods are described in a particular, sequential order for convenient presentation, it should be understood that this manner of description encompasses rearrangement, unless a particular ordering is required by specific language set forth below. For example, operations described sequentially may in some cases be rearranged or performed concurrently. Moreover, for the sake of simplicity, the attached figures may not show the various ways in which the disclosed systems, methods, and apparatus can be used in conjunction with other systems, methods, and apparatus. Additionally, the description sometimes uses terms like "produce" and "provide" to describe the disclosed methods. These terms are high-level abstractions of the actual operations that are performed. The actual operations that correspond to these terms will vary depending on the particular implementation and are readily discernible by one of ordinary skill in the art.

In some examples, values, procedures, or apparatus' are referred to as "lowest", "best", "minimum," or the like. It will be appreciated that such descriptions are intended to indicate that a selection among many used functional alternatives can be made, and such selections need not be better, smaller, or otherwise preferable to other selections.

In view of the many possible embodiments to which the principles of the disclosed technology may be applied, it should be recognized that the illustrated embodiments are only preferred examples and should not be taken as limiting the scope of the disclosure. We, therefore, claim as all that comes within the scope and spirit of the appended claims.

Chapter 5: Conclusions and Future Scope of Work

This chapter summarizes the final conclusions of this dissertation work and recommends areas for future work.

5.1 Conclusions

The main goal of this dissertation work was to improve the existing visual inspection methodology and increase the accuracy of detecting and quantifying surface and subsurface defects. While working towards this goal, following set of objectives were accomplished and conclusions were drawn.

1. Image processing algorithms were developed to detect and quantify surface defects in concrete structures.

A number of image processing techniques were tested to detect and quantify surface deterioration. It was found that using HSV, crack is detected at higher accuracy compared to BHT.

2. A damage assessment software tool was developed to assign condition assessment rating for civil structures.

An innovative graphical user interface was developed to help field inspectors quantify surface damage using the image processing algorithm. Using fuzzy logic network, a damage rating can be assigned which provides an insight to the infrastructure owner about any repair work that may be required.

3. A new NDT data refinement model was developed to determine the performance of commercially available NDT techniques in detecting and quantifying subsurface defects

A number of commercially available NDT techniques were applied on RC slabs with simulated damage to determine their performance. More than 300 data points were collected to develop an refinement model. These data points were also converted into data maps to help field practitioners interpret the data correctly. Using the refinement model, it was found that by combining three NDT techniques strategically, the percentage error could be lowered down to 26% for these slabs.

4. A new methodology (termed IPA) was developed that integrates a UAV system into a visual inspection-based guideline to detect and quantify condition of surface defects.

To improve the accuracy and reliability of AASHTO guideline based visual bridge inspection, a new methodology (IPA) that incorporates the use of a UAV system and Image processing was developed. Using IPA, field inspectors can collect the required inspection dataset using a UAV system. The defects can be quantified using image processing to assign a damage rating as per the AASHTO guideline.

5. A novel multi-device robotics-based sensor data acquisition system was developed for mapping and assessing defects in civil structures.

A patent pending damage assessment technique which utilizes a combination of multiple sensors was developed. These sensors include two optical cameras, an infrared camera, an acoustic assembly, and two laser sensors. The sensors are integrated in such that the data

collected could be overlaid on top of each other to detect and quantify damage more accurately and reliably.

6. A novel UAV-based acoustic technique was developed for mapping subsurface defects in civil structures.

A patent pending UAV-based acoustic technique was developed to detect and quantify subsurface defects. It highlights a novel inspection apparatus that comprises of a UAV and an acoustic signal generator coupled to the UAV to detect and quantify subsurface defects. The acoustic signal generator includes a hammer having a contact surface (movable by the UAV) to produce an acoustic signal in a structure. Using this technique, field inspectors can conduct the assessment without having to use an expensive snooper truck, scaffolding platform or a ladder.

5.2 Future Scope of Work

A number of significant advancements have been made in this dissertation work. However, some of the work performed in this study can be expanded further in the following two categories.

1. Development of a Damage Assessment Software for Civil Infrastructures

There are three techniques that have been developed for the improvement of visual inspection method; 1) Combined use of fuzzy logic and image processing algorithm to quantify defects, 2) UAV-assisted AASHTO guideline-based damage assessment technique, and 3) Multi-device robotics-based sensor data acquisition system for mapping and assessing defects in civil structures. It is suggested that the first two techniques could be combined into one single technique where fuzzy logic-based decision making could be replaced by Artificial Intelligence (AI)-based decision making. The AI could be relying on AASHTO-based guideline (AASHTO, 2011) at the beginning until the sufficient dataset (large enough) is available. In order to make an AI-based surface damage detection, it is suggested to have more ground truth data in terms of the images to train the image processing algorithm. Following objectives and tasks could be followed to develop the first prototype of an AI-based damage assessment software for civil structures.

Objectives

1. To develop a refined and complete version of a damage assessment tool which is capable of processing image datasets as large as 3000 images (first target) and returning a damage assessment in less than 2 seconds

For this, improve and optimize the existing damage assessment software through iterative testing, improving the algorithm and refactoring the code on 3000 image datasets until program execution can be reliably completed in less than 2 seconds as a fist target. The higher target in terms of more number of images and less computational time could be set depending upon the capacity.

2. To accomplish improved image processing for crack detection of concrete (0.12 mm width or greater), within the software tool, to be used alongside human discernment (85% success rate (first target) in matching ground truth data)

To achieve this target, acquire, label, and process 15,000 high resolution digital images (first target) of bridge structures, with thousands of images designated for crack detection as well as sound bridge components

3. To develop improved detection of delamination in bridge decks, within the software tool (85% success rate (first target) in matching professional civil engineer discernments)

Train the neural network continuously using the accord.net framework, iteratively refining datasets for each defect (cracks and delamination). Accord.NET is a machine learning framework for scientific computing in .NET.

In addition to the cracking and delamination, other defects mentioned in AASHTO guideline could be used to train the algorithm. The list of defects is mentioned in Table 18. Each defect is assigned with a unique code to assign a combined code to national bridge elements as shown in Figure 62. For example, reinforced concrete bridge deck (element 12/38) has a defect code- "EAHI", where E is cracking, A is spalling, H is efflorescence, and I is load capacity. The AI model could be trained to detect and quantify all of these defects ("EAHI") for reinforced concrete bridge decks.

Table 18: List of Defects from AASHTO guide manual (AASHTO, 2011)

Code	**Type of Defect**	**Code**	**Type of Defect**
A	Spalling	U	Stands and Banding
B	Corrosion of Reinforcement	V	Anchors
C	Leaching	W	Distortion
D	Scaling	X	Settlement
E	Cracking	Y	Scour
F	Honeycombing	Z	Leakage
G	Delamination	1	Seal Adhesion
H	Efflorescence	2	Debris Impaction
I	Load Capacity	3	Adjacent Deck or Header
J	Connectors	4	Seal Cracking
K	Decay	5	Movement
L	Checks/shingles	6	Alignment
M	Splits	7	Loss of Bearing Area
N	Abrasion	8	Bulging or Tearing
O	Exposed Rebar	9	Chalking
P	Exposed Prestressing	10	Peeling/bubbling
Q	Compression Members	11	Wear
R	Mortar Breakdown	12	Effectiveness
S	Block or Stone	13	Damage
T	Patched Areas		

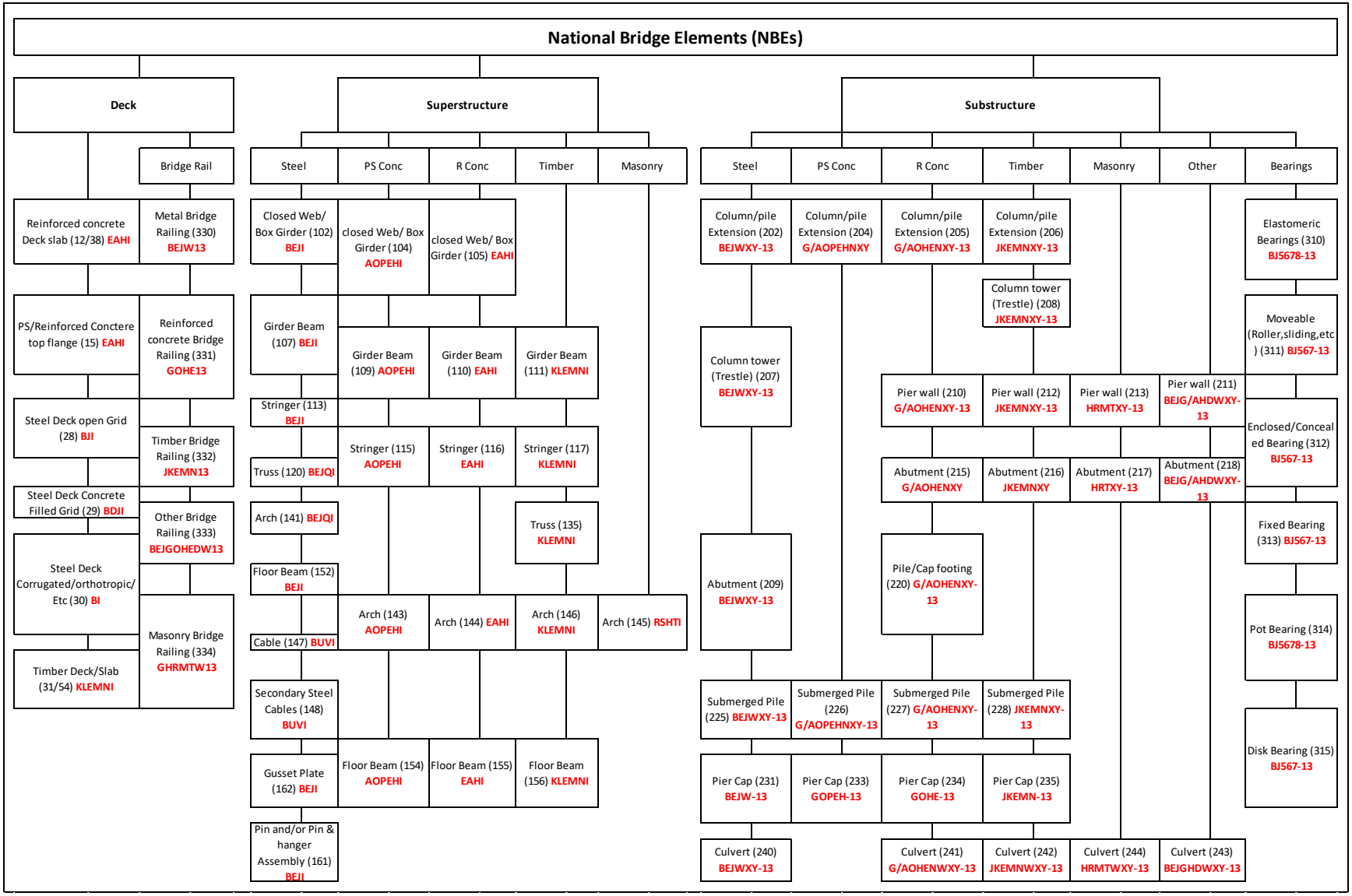

Figure 62: National Bridge Elements with the type of defects (shown in red bold letters), (AASHTO, 2011)

Using the developed prototype (termed "AutoSpex"), the inspectors can login to generate condition assessment report using AutoSpex as shown in Figure 63.

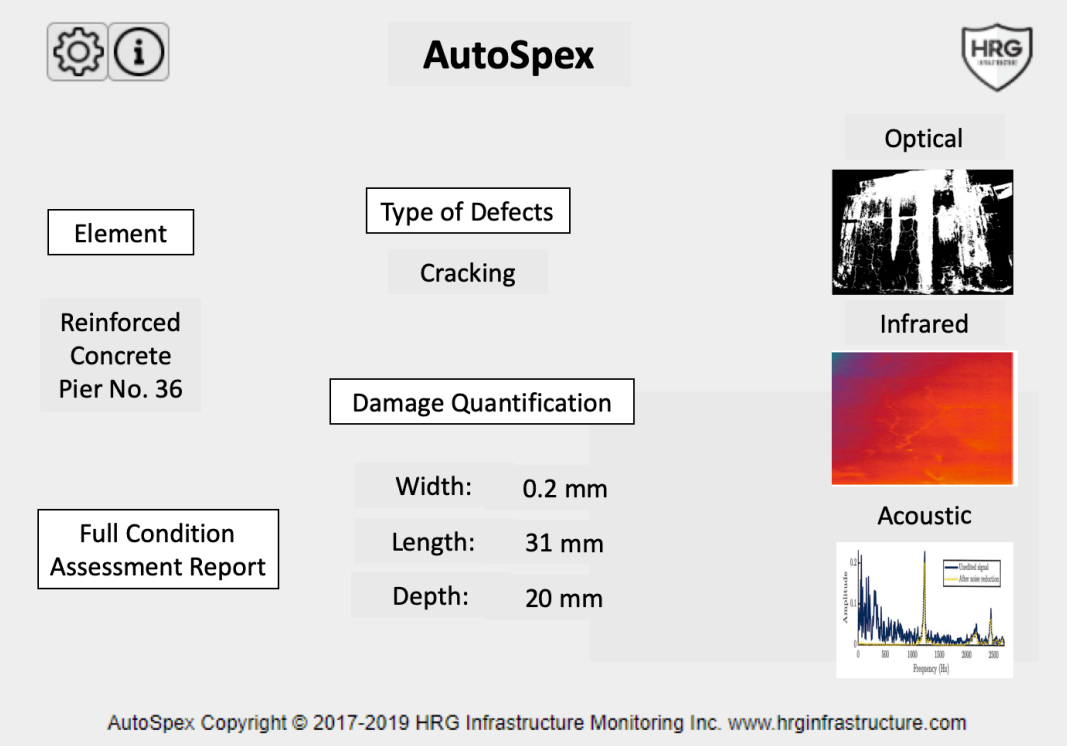

Figure 63: AutoSpex interface

2. Further Development of Multi-Device Robotics-based Sensor System and other Non-Destructive Testing Techniques

More work is required in the area of UAV flight path optimization for condition assessment of bridges. Current flight path optimization only accounts for the camera to concrete surface distance and the UAV speed. However, it is suggested to account for the environmental conditions such as wind speed, wind directions, time of the day, etc. to efficiently plan the battery endurance and acquisition of quality data.

The developed NDT refinement model uses section property and durability to evaluate the performance of NDT techniques. This model could be further expanded to include cost of an NDT technique, reliability, and time as proposed in Figure 64. This will allow NDT practitioners to make more informed decisions.

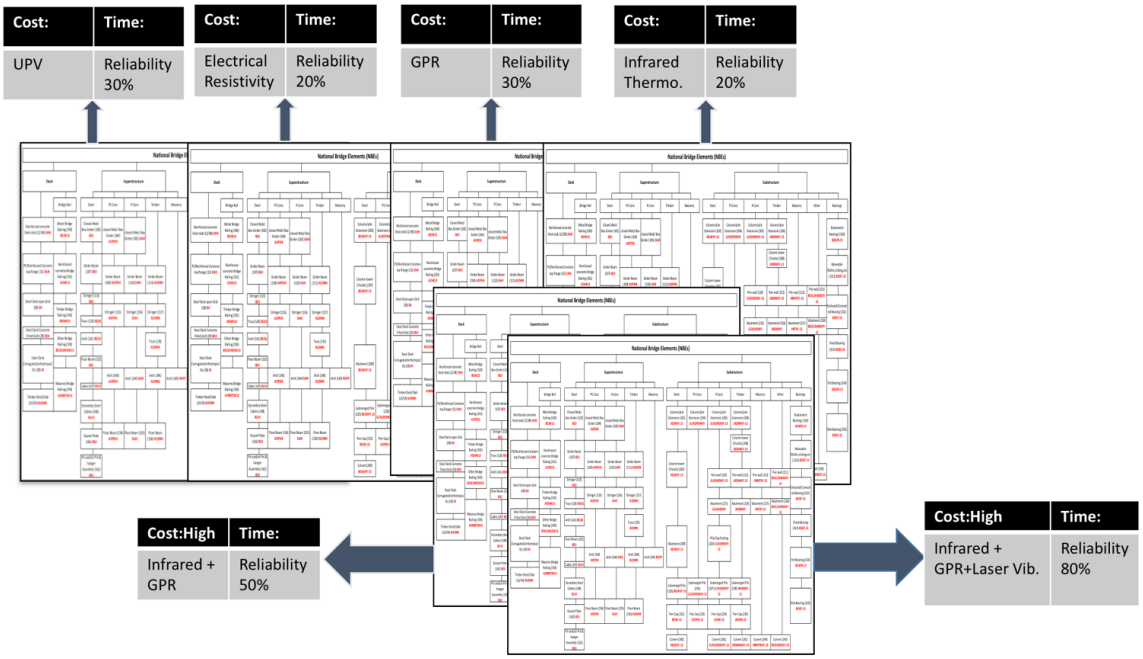

Figure 64: Conceptual layered NDT data refinement model

Bibliography

ACI-228.2R, 2013, “Report on Non-destructive Test Methods for Evaluation of Concrete in Structures”, American Concrete Institute.

Ahmedov, S.V., Stetsenko, I.A. & Grushko, I.S. 2015, "High Precision Device for Diameter Rebar Control in Reinforced Concrete Products", *Procedia Engineering,* vol. 129, pp. 754-758.

American Association of State Highway and Transportation Officials 2011, *Manual for bridge element inspection: 2015 Interim,* 2015 interim [revision]. edn, American Association of State Highway and Transportation Officials, Washington, DC.

American Society of Civil Engineers (ASCE) 2013, “Report card for America’s infrastructure.” 〈http://www.infrastructurereportcard.org〉

Arliansyah J., Maruyama T. and Takahashi O. (2003). “A development of fuzzy pavement condition assessment”, *Japan Soc. of Civ. Engg.*, 61(746), 275–285.

Ayala-Cabrera, D., Herrera, M., Izquierdo, J. & Pérez-García, R. 2011, "Location of buried plastic pipes using multi-agent support based on GPR images", *Journal of Applied Geophysics,* vol. 75, no. 4, pp. 679-686.

Azarsa, P. & Gupta, R. 2017, "Electrical Resistivity of Concrete for Durability Evaluation: A Review", *Advances in Materials Science and Engineering,* vol. 2017, pp. 1-30.

Balageas, D., Fritzen, C. & Güemes, A., 2010, "Introduction to Structural Health Monitoring" in ISTE, London, UK, pp. 13-43.

Benedetto, A., Pajewski, L. & SpringerLink (Online service) 2015, *Civil Engineering Applications of Ground Penetrating Radar,* Springer International Publishing, Cham.

Bhalla, S., Tuli, S. & Arora, R. 2011, "Defect detection in concrete structures using thermal imaging techniques", *Experimental Techniques,* vol. 35, no. 4, pp. 39-43.

Bhattacharya, S. & Maitra, A.K. 2007, "Impact of Coal Beneficiation on Rail Transport in India", *Coal Preparation,* vol. 27, no. 1-3, pp. 149-166.

Birk, A., Wiggerich, B., Bülow, H., Pfingsthorn, M. & Schwertfeger, S. 2011, "Safety, Security, and Rescue Missions with an Unmanned Aerial Vehicle (UAV): Aerial Mosaicking and Autonomous Flight at the 2009 European Land Robots Trials (ELROB) and the 2010 Response Robot Evaluation Exercises (RREE)", *Journal of Intelligent & Robotic Systems,* vol. 64, no. 1, pp. 57-76.

Blaney, S. 2018, *Unmanned aerial vehicle-based non-destructive testing methods for concrete structures*, Thesis Submitted to University of Victoria.

Blockley D.I. (1975). “Predicting the likelihood of structural accidents”, *Proc. Inst. of Civ. Engrs.*, 59(4), 659–668.

Blockley D.I. (1977). “Analysis of structural failures.” *Proc. Inst. of Civ. Engrs*, 62(1), 51–74.

Breysse, D., RILEM Technical Committee 207-INR & ebrary, I. 2012, *Non-destructive assessment of concrete structures: reliability and limits of single and combined techniques: State-of-the-Art Report of the RILEM Technical Committee 207-INR,* 2012th edn, Springer, New York.

Brown C.B. and Yao J. T. P. (1983). “Fuzzy sets and structural engineering.” *J. Struct. Engg.,* 109(5), 1211–1225.

C1202 Standard Test Method for Electrical Indication of Concrete's Ability to Resist Chloride Ion Penetration, 2017, ASTM International.

C597 Standard Test Method for Pulse Velocity Through Concrete, 2016, ASTM International.

C876 Standard Test Method for Corrosion Potentials of Uncoated Reinforcing Steel in Concrete, 2015, ASTM International.

Chang P.C., Flatau , and Liu. S. C. (2003). “Review paper: health monitoring of civil infrastructure.” *Struct. health monitoring*, 2(3), 257-267.

Chang, C., Wang, J., Liang, M. & Lin, M. 2016, "Development of a multicopter-carried whole air sampling apparatus and its applications in environmental studies", *Chemosphere,* vol. 144, pp. 484-492.

Cheng, E. 2015, *Aerial Photography and Videography Using Drones,* 1st edn, Peachpit Press.

Chiu, W.K., Ong, W.H., Kuen, T. & Courtney, F. 2017, "Large Structures Monitoring Using Unmanned Aerial Vehicles", *Procedia Engineering,* vol. 188, pp. 415-423.

Clark, M.R., McCann, D.M. & Forde, M.C. 2003, "Application of infrared thermography to the non-destructive testing of concrete and masonry bridges", *NDT and E International,* vol. 36, no. 4, pp. 265-275.

Concrete Handbook-GSSI, 2015, “GPR Inspection of Concrete”, Published by Geophysical Survey Systems, Inc.

Conde, B., Ramos, L.F., Oliveira, D.V., Riveiro, B. & Solla, M. 2017, "Structural assessment of masonry arch bridges by combination of non-destructive testing techniques and three-dimensional numerical modelling: Application to Vilanova bridge", *Engineering Structures,* vol. 148, pp. 621-638.

Cruz, P.J.S., Topczewski, L., Fernandes, F.M., Trela, C. & Lourenço, P.B. 2010, "Application of radar techniques to the verification of design plans and the detection of defects in concrete bridges", *Structure and Infrastructure Engineering,* vol. 6, no. 4, pp. 395-407.

D4788 Standard Test Method for Detecting Delaminations in Bridge Decks Using Infrared Thermography 2013, ASTM International.

Delgado, J.M.P.Q. & SpringerLink (Online service) 2016, *New Approaches to Building Pathology and Durability,* 1st 2016.;1st 2016; edn, Springer Singapore, Singapore.

Dong W. and Shah H. (1987), “Vertex Method for computing functions of fuzzy variables.”*Fuzzy Sets Syst.*, 24 65-78.

Dong Y., Song R. and Liu H. (2003). “Bridges Structural Health Monitoring and Deterioration Detection - Synthesis of Knowledge and Technology”, *Technical Report*, University of Alaska Fairbanks.

Dorafshan, S., Maguire, M., Hoffer, N.V. & Coopmans, C. 2017, "Challenges in bridge inspection using small unmanned aerial systems: Results and lessons learned", IEEE, pp. 1722.

Ellenberg, A., Kontsos, A., Moon, F. & Bartoli, I. 2016, "Bridge related damage quantification using unmanned aerial vehicle imagery", *Structural Control and Health Monitoring,* vol. 23, no. 9, pp. 1168-1179.

Fan, Y., Ji, X., Cai, P. & Lu, Q. 2013, "Non-Destructive Detection of Rebar Buried in a Reinforced Concrete Wall with Wireless Passive SAW Sensor", *Measurement Science Review,* vol. 13, no. 1, pp. 25.

Fischbach, A. 2014, "Unmanned Aerial Vehicle Inspects Powerlines", *Transmission & Distribution World (Online Exclusive),*

Furuta H., Hirokane M., Tanaka S., and Mikumo Y. (2000). “A study of technology for diagnosing bridge soundness by using portable computer”, *Proc. 8th Int. Conf. on Computing in Civ. and Bldg. Engg.*, Stanford, Ca.,1037–1044.

Fwa T. F, Liu S.B and Teng K. J. (2003). “Airport pavement condition rating and maintenance-needs assessment using fuzzy logic” *Proc., Airfield Pavements: Challenges and New Technologies*, ASCE, Reston, Va., 29–38.

Gagon, M., Guadreault, V., Overton, D., Statistics Canada. Investment and Capital Stock Division & Canadian Electronic Library (Firm) 2008, *Age of public infrastructure: a provincial perspective,* Statistics Canada, Investment and Capital Stock Division, Ottawa, Ont.

Gangopadhyay, A. & Ghosh, A.D. 2016, "Seismic Retrofitting of an Existing Steel Railway Bridge by Fluid Viscous Dampers", *Journal of The Institution of Engineers (India): Series A,* vol. 97, no. 3, pp. 291-297.

Garzon, A.J., Sanchez, J., Andrade, C., Rebolledo, N., Menéndez, E. & Fullea, J. 2014, "Modification of four-point method to measure the concrete electrical resistivity in presence of reinforcing bars", *Cement and Concrete Composites,* vol. 53, pp. 249-257.

Hadipriono F. C. (1988). “Fuzzy set concepts for evaluating performance of constructed facilities.” *J. Perf. Constr. Facil.,* 2(4), 209–225.

Halsall, P. 2016, *Canadian Infrastructure Report Card,* Johnson-Shoyama Graduate School of Public Policy.

Handlon, B., Lorenc, S.J., Bernold, L. & Lee, G. 2000, "Tool integrated electromagnetic pulse induction technology to locate buried utilities", IEEE, pp. 529.

Hanif, M.U., Ibrahim, Z., Ghaedi, K., Hashim, H. & Javanmardi, A. 2018, "Damage assessment of reinforced concrete structures using a model-based nonlinear approach – A comprehensive review", Construction and Building Materials, vol. 192, pp. 846-865.

Hathout I.(1993). “Damage assessment of existing transmission towers using fuzzy weighted averages.”*Proc., Second Int. Symp. on Uncertainty Modeling and Analysis*, Los Alamitos, Ca., 573–580.

Hong, S., Wiggenhauser, H., Helmerich, R., Dong, B., Dong, P. & Xing, F. 2017, "Long-term monitoring of reinforcement corrosion in concrete using ground penetrating radar", *Corrosion Science,* vol. 114, pp. 123-132.

Huang, Q., Gardoni, P. & Hurlebaus, S. 2011, "Predicting Concrete Compressive Strength Using Ultrasonic Pulse Velocity and Rebound Number", *ACI Materials Journal,* vol. 108, no. 4, pp. 403.

Huth, O., Feltrin, G., Maeck, J., Kilic, N. & Motavalli, M. 2005, "Damage Identification Using Modal Data: Experiences on a Prestressed Concrete Bridge", Journal of Structural Engineering, vol. 131, no. 12, pp. 1898-1910

Ikhlas A-Q., Abudayyeh O. and Kelly M.E. (2003). “Analysis of edge-detection techniques for crack identification in bridges.” *J. Comp. Civ. Engg.*, 17 (4), 255–263.

Jahanshahi M. R., and Masri S. F. (2013). “A new methodology for non-contact accurate crack width measurement through photogrammetry for automated structural safety evaluation.” *Smart mater. &Structs.*, 22(3), 035019.

Jahanshahi M.R. and Masri S. F. (2012). “Adaptive vision-based crack detection using 3D scene reconstruction for condition assessment of structures.” *Automn.in Constrn.,* 22,567-576.

Jahanshahi M.R., Kelly J.S, Masri S.F. and Sukhatme G.S. (2009). “A survey and evaluation of promising approaches for automatic image-based defect detection of bridge structures.” *J. Struct. Infrastructural Engg.*, 5 (6), 455–486.

Jain K.K. and Bhattacharjee B. (2012a). “Application of fuzzy concepts to the visual assessment of deteriorating reinforced concrete structures.” *J. Const. Engg. & Mgmt.,* 138(3), 399–408.

Jain K.K and Bhattacharjee B. (2012b). “Visual Inspection and Condition Assessment of Structures [VICAS]: An Innovative Tool for Structural Condition Assessment.” *Int. J. 3 R’s*, 3(1), 349–357.

Kashif Ur Rehman, S., Ibrahim, Z., Memon, S.A. & Jameel, M. 2016, "Nondestructive test methods for concrete bridges: A review", *Construction and Building Materials,* vol. 107, pp. 58-86.

Kim Y. M., Kim C. K. and Hong S.G. (2006). “Fuzzy-based state assessment for reinforced concrete building structures.” *Engg. Struct.,* 28(9), 1286–1297.

Kim, H., Lee, J., Ahn, E., Cho, S., Shin, M. & Sim, S. 2017, "Concrete Crack Identification Using a UAV Incorporating Hybrid Image Processing", *Sensors (Basel, Switzerland),* vol. 17, no. 9, pp. 2052.

Krick, A., Ellenberg, A., Kontsos, A., Branco, L. & Bartoli, I. 2015, "Use of Unmanned Aerial Vehicle for Quantitative Infrastructure Evaluation", *Journal of Infrastructure Systems,* vol. 21, no. 3, pp. 4014054.

Lataste, J. & Breysse, D. 2013, "A Study on the Variability of Electrical Resistivity of Concrete" in , 2013th edn, Springer Netherlands, Dordrecht, pp. 255-261.

Lattanzi D., Miller G. R. (2014). “Robust automated concrete damage detection algorithms for field applications.” *J. Compt. Civ. Engineer.,* 28,2253–262.

Leslie, J., and Cheesman, W., 1949 “An ultrasonic method of studying deterioration and cracking in concrete structures”, Journal of American Concrete Institute, 46, 17-36.

Liang M. T., Wu J. H. and Liang C. H. (2001). “Multiple layer fuzzy evaluation for existing reinforced concrete bridges.” *J. Infrastructure Sys.*, 7(4), 144–159.

Madau, D. P.; Feldkamp, L. A. (1996). "Influence value defuzzification method". *Fuzzy Systems*. 3: 1819–1824.

Mamdani EH, Assilian S. (1975).“An experiment in linguistic synthesis with a fuzzy logic controller.”*Int J Man Mach Stud*,7(1), 13.

Mechbal, Z. & Khamlichi, A. 2017, "Determination of concrete rebars characteristics by enhanced post-processing of GPR scan raw data", *NDT and E International,* vol. 89, pp. 30-39.

Miller, T.H., Kundu, T., Huang, J. & Grill, J.Y. 2013, "A new guided wave–based technique for corrosion monitoring in reinforced concrete", *Structural Health Monitoring,* vol. 12, no. 1, pp. 35-47.

Mitra G., Jain K. K., and Bhattacharjee B. (2010). “Condition assessment of corrosion-distressed reinforced concrete buildings using fuzzy logic.” *Journal J. Perf. Constr. Facil.,* 24(6), 562–570.

Nguyen H-N., Kam T-Y., and Cheng P-Y. (2012). “A novel automatic concrete surface crack identification using isotropic undecimated wavelet transform.” *Intelligent Signal Processing & Comms. Syst.*, 766-711.

Ogawa H., Fu K. S and Yao J.T.P. (1984). “An expert system for structure damage assessment”. *Pattern Recog. Letter*, 2(6), 427–432

Petro, J.T. & Kim, J. 2012, "Detection of delamination in concrete using ultrasonic pulse velocity test", *Construction and Building Materials,* vol. 26, no. 1, pp. 574-582.

Polder, R.B. 2001, "Test methods for on site measurement of resistivity of concrete — a RILEM TC-154 technical recommendation", *Construction and Building Materials,* vol. 15, no. 2, pp. 125-131.

Portland Cement Association, (2002) "Types and Causes of Concrete Deterioration", IS 536.01, 16 pages

Prabakar, J., Bharathkumar, B.H. & Chellappan, A. 2007, "Prediction of rebar profile in a earth retaining RCC structure using cover meter survey", *Construction and Building Materials,* vol. 21, no. 4, pp. 873-878.

Pragalath, H., Seshathiri, S., Rathod, H., Esakki, B., and Gupta, R., 2018, "Deterioration Assessment of Infrastructure Using Fuzzy Logic and Image Processing Algorithm", *Journal of Performance of Constructed Facilities,* vol. 32, no. 2, pp. 4018009.

Prasanna P., Dana K., Gucunski N. and Basily B. (2012). "Computer vision-based crack detection and analysis." *SPIE Smart Structs. & Mater. & Nondestructive Evla. Health Mon.,* International Society for Optics and Photonics, 834542.

Profoscope Operating Instructions, 2017, by Proceq.

Rathod, H. & Gupta, R. 2019a, "Sub-surface simulated damage detection using Non-Destructive Testing Techniques in reinforced-concrete slabs", Construction and Building Materials, vol. 215, pp. 754-764.

Rathod, H. & Gupta, R. 2019b, "Two-dimensional non-destructive testing data maps for reinforced concrete slabs with simulated damage", Data in Brief, vol. 25, pp. 104127.

Rathod, H., Debeck, S., Gupta, R. & Chow, B. 2019c, "Applicability of GPR and a rebar detector to obtain rebar information of existing concrete structures", Case Studies in Construction Materials, vol. 11, pp. e00240. (Open access)

Rathod, H., Gupta, R., 2019e "Multi-device Robotics-based Sensor Data Acquisition System for Mapping and Assessing Defects in Infrastructure", USPTO Provisional Patent, Application No. 62828781; Klarquist Ref. No. 2847-102346-01 (Submission Date- April 15th, 2019) (Licensed to HRG Infrastructure Monitoring Inc.)

Rathod, H., Gupta, R., 2019f "UAV-based Acoustic Technique for Mapping Defects in Civil Infrastructure", Patent Filed under Patent Cooperation Treaty - Ref. No. GUPRI-T3147; Klarquist Ref. No. 2847-100745-01 (Submission Date- May 1, 2019) (Licensed to HRG Infrastructure Monitoring Inc.)

Rice, J.A., Lasa, I.R., Agdas, D. & Martinez, J.R. 2016, "Comparison of Visual Inspection and Structural-Health Monitoring as Bridge Condition Assessment Methods", *Journal of Performance of Constructed Facilities,* vol. 30, no. 3, pp. 4015049.

RILEM TC-154-EMC 2004, "Recommendations of RILEM TC-154-EMC: "Electrochemical techniques for measuring metallic corrosion" Test methods for on-site corrosion rate measurement of steel reinforcement in concrete by means of the polarization resistance method", *Materials and Structures,* vol. 37, no. 273, pp. 623-643.

Rose P., Aaron B., Tamir D.E., Lu L. and Hu J. (2014). "Supervised computer-vision-based sensing of concrete bridges for crack-detection and assessment." *Trans. Res. Board 93rd Annual Meeting*, Washington DC, USA, 14: 3857.

Ross T.J, Sorensen H.C., Savage S. J. and Carson J. M. (1990). "DAPS: Expert system for structural damage assessment." *J. Comp. in Civ. Engg.,* 4(4), 327–348.

Ross TJ. (2005)." Fuzzy logic with engineering applications." India: Wiley-India.

Saari, H., Akujärvi, A., Holmlund, C., Ojanen, H., Kaivosoja, J., Nissinen, A. & Niemeläinen, O. 2017, "VISIBLE, VERY NEAR IR AND SHORT WAVE IR HYPERSPECTRAL DRONE IMAGING SYSTEM FOR AGRICULTURE AND NATURAL WATER APPLICATIONS", *The International Archives of the Photogrammetry,* , pp. 165-170.

Saint-Pierre, F., Philibert, A., Giroux, B. & Rivard, P. 2016, "Concrete Quality Designation based on Ultrasonic Pulse Velocity", *Construction and Building Materials,* vol. 125, pp. 1022-1027.

Sankarasrinivasan S., Balasubramanian E., Karthik K., Chandrasekar U. and Gupta R. (2015). "Health Monitoring of Civil Structures with Integrated UAV and Image Processing System." *Eleventh Int. Con. on Image & Signal Processing,* Elsevier Procedia Computer Science, Bangalore, India, 508-515.

Sasmal S. and Ramanjaneyulu K. (2008). "Condition evaluation of existing reinforced concrete bridges using fuzzy-based analytic hierarchy approach." *Expert System App.,* 35(3), 1430–1443.

Sasmal S., Ramanjaneyulu K., Gopalakrishnan S. and Lakshmanan N. (2006). "Fuzzy logic-based condition rating of existing reinforced concrete bridges." *J. Perf. Constr. Facil.,* 20(3), 261–273.

Savage S.J., Ross T., Sorensen H., Carson J. and Satterthwaite B.(1988), "Development of a rule-based structural damage assessment code", *AFWL-TR-87-19*, Air Force Weapons Laboratory, Kirtland Air Force Base, Albuquerque, NM.

Sengul, O. 2014, "Use of electrical resistivity as an indicator for durability", *Construction and Building Materials,* vol. 73, pp. 434-441.

Souflis C. and Grivas D. A. (1986). "Fuzzy set approach to linguistic seismic load and damage assessments." *J. Engg. Mech.,* 112(6), 605–618.

Stek, T.D. 2016, "Drones over Mediterranean landscapes. The potential of small UAV's (drones) for site detection and heritage management in archaeological survey projects: A case study from Le Pianelle in the Tappino Valley, Molise (Italy)", *Journal of Cultural Heritage,* vol. 22, pp. 1066-1071

Torok M., Golparvar-Fard M., Kochersberger K. (2014). "Image-based automated 3D crack detection for post-disaster building assessment." *J. Comp. Civ. Engg.*, 28(5), A4014004.

"TP 95-11 - Surface Resistivity Indication of Concrete's Ability to Resist Chloride Ion Penetration" 2013, in , 33rd edn, American Association of State Highway and Transportation Officials (AASHTO), pp. 1-1.

Utsi, V. & Utsi, E. 2004, "Measurement of reinforcement bar depths and diameters in concrete", IEEE, pp. 659.

Vazquez M.A., Galan E., Guerrero M.A. and Ortiz P. (2011). "Digital image processing of weathered stone caused by efflorescence: A tool for mapping and evaluation of stone decay." *Const.& Buil. Mater.*, 25(4), 1603-1611.

Vidal M., Ostra M., Imaz N., García-Lecina E. and Ubide C. (*2016*). "Analysis of SEM digital images to quantify crack network pattern area in chromium electro deposit." *Surface and Coatings Tech.,* 285, 289-297.

Wang Y. M. and Elhag T. M. S. (2007). "A fuzzy group decision making approach for bridge risk assessment." *Comp. Indu. Engg.,* 53(1), 137–148.

Washer, G., Fenwick, R., Bolleni, N. & Harper, J. 2009, "Effects of Environmental Variables on Infrared Imaging of Subsurface Features of Concrete Bridges", *Transportation Research Record: Journal of the Transportation Research Board,* vol. 2108, no. 1, pp. 107-114.

Wenzel, H. & Books, I. 2008, Health monitoring of bridges, 1st edn, Wiley, New York.

Xiao, H., Qin, J., Ogai, H. & Jiang, X. 2015, "A new standing-wave testing system for bridge structure nondestructive damage detection using electromagnetic wave", *IEEJ Transactions on Electrical and Electronic Engineering,* vol. 10, no. 2, pp. 157-165.

Yamaguchi T. and Hashimoto S. (2010). "Fast crack detection method for large-size concrete surface images using percolation-based image processing." *Mach. Vis. App.*21(5), 797–809.

Yamaguchi T., Nakamura S., Saegusa R. and Hashimoto S. (2008). "Image-based crack detection for real concrete surfaces." *IEEE Trx. Electrical Electronic Engg.,* 3(1), 128–135.

Yao R. and Pakzad S.N. (2012). "Autoregressive statistical pattern recognition algorithms for damage detection in civil structures." *Mech. Sys. & Signal Prcsg*, 31, 355-368.

Yao, Q. & Qifu, W. 2012, "Kirchoff Migration Algorithm for Ground Penetrating Radar Data", IEEE, pp. 396.

Yehia, S., Abudayyeh, O., Nabulsi, S. & Abdelqader, I. 2007, "Detection of Common Defects in Concrete Bridge Decks Using Nondestructive Evaluation Techniques", *Journal of Bridge Engineering,* vol. 12, no. 2, pp. 215-225.

Yodsudjai, W. & Pattarakittam, T. 2017, "Factors influencing half-cell potential measurement and its relationship with corrosion level", *Measurement,* vol. 104, pp. 159-168.

Yun CB., and Min J. (2011). "Smart sensing, monitoring, and damage detection for civil infrastructures." *KSCE J. Civ. Engg.*, 15(1), 1-14.

Zanzi, L. & Arosio, D. 2013, "Sensitivity and accuracy in rebar diameter measurements from dual-polarized GPR data", *Construction and Building Materials,* vol. 48, pp. 1293-1301.

Zhao, J., and Bose, B. K. (2002). Evaluation of membership functions for fuzzy logic controlled induction motor drive. 28th Annual Conference on IEE Industrial Electronics Society, pp. 229-234.

Zhao, S. & Al-Qadi, I. 2017, "Pavement drainage pipe condition assessment by GPR image reconstruction using FDTD modeling", *Construction and Building Materials,* vol. 154, pp. 1283-1293.

Zhao, S. & Al-Qadi, I. 2017, "Pavement drainage pipe condition assessment by GPR image reconstruction using FDTD modeling", *Construction and Building Materials,* vol. 154, pp. 1283-1293.

Zou Q., Cao Y., Li Q., Mao Q. and Wang S. (2012). "Crack Tree: Automatic crack detection from pavement images." *Pattern Recognition Letters*, 33(3), 227-238.

Appendices

Appendix A

Procedure for Developing Membership Functions:

Step 1: Collect the data from Experts or visual inspectors**.** Table 19 Shows the summary of expert responses used in this study

Table 19: Summary of the expert responses for various distress conditions (Jain and Bhattacharjee, 2012b)

Type of defects due to Corrosion	**Distress State description**	**Assigned Rating and Number of Responses**					
		0	**1**	**2**	**3**	**4**	**5**
Spalling	Depressions less than 20 mm in depth and not exceeding 150 mm in any other dimension	1	5	10	19	10	4
	Depressions of size more than 20 mm in depth with any other dimension greater than 150 mm	0	1	4	9	21	14
Rust Staining & Moisture Marks	Stains visible in isolated patches	10	12	19	8	2	0
	Stains visible covering large area	2	8	11	14	11	5
Cracks	Crack parallel to either stirrups/longitudinal rebars or main rebars , running in one direction only (1-D cracks)	1	9	11	16	10	4
	Isolated cracks parallel to both stirrups/longitudinal rebars and main rebars (2-D cracks)	0	3	14	15	15	4
	Extensive cracks, spanning in both the directions, over relatively large surface area	0	0	4	10	17	20

Following condition rating definition is considered (based on repair priority)
0: Condition doesn't require any repair
1: Very low priority repair, can be delayed for long span of time
2: Low priority repair, actions may be delayed for significant time
3: Medium priority repair, actions may be delayed for some time
4: High priority repair, urgent actions might be required
5: Condition is critical; actions must be carried out immediately

Step 2: Further tune the data as per following equations

If $\left[R_i < R_{i-1} \text{and } R_i < R_{i+1}\right]$,

then update $\left[R_i = 0.5\left(R_{i-1} + R_{i+1}\right)\right]$

and

$$\text{If}\left[R_i < 0.1\times\left(\sum_{i=0}^{5} R_i\right)\right] \text{ then update } \left[R_i = 0\right]$$

Step 3: The obtained numbers are then normalized as

$$\mu_{xi} = \frac{R_i}{\max_{i=0,1,2,\ldots..5}\left(R_i\right)}$$

Step 4: The resulting numbers are shown in the Table 20 after tuning

Table 20: Summary of obtained condition indices based on the distress state

Type of defects due to Corrosion	**Distress State description**	**Condition Indices**					
		0	**1**	**2**	**3**	**4**	**5**
Spalling	Depressions less than 20 mm in depth and not exceeding 150 mm in any other dimension	0.05	0.26	0.53	1.00	0.53	0.21
	Depressions of size more than 20 mm in depth with any other dimension greater than 150 mm	0.00	0.05	0.19	0.43	1.00	0.67
Rust Staining & Moisture Marks	Stains visible in isolated patches	0.53	0.63	1.00	0.42	0.11	0.00
	Stains visible covering large area	0.14	0.57	0.79	1.00	0.79	0.36
Cracks	Crack parallel to either stirrups/longitudinal rebars or main rebars , running in one direction only (1-D cracks)	0.06	0.56	0.69	1.00	0.63	0.25
	Isolated cracks parallel to both stirrups/longitudinal rebars and main rebars (2-D cracks)	0.00	0.20	0.93	1.00	1.00	0.27
	Extensive cracks, spanning in both the directions, over relatively large surface area	0.00	0.00	0.20	0.50	0.85	1.00

Step 5: The obtained MFs are modified using linguistic hedges/modifiers (Mitra et al. 2010) to account for local and global level of defects, which are given by,

$$Local:\ \mu_{x_i}, local = \mu_{x_i}^{1/2} \quad for\ \ x_i \le x_0$$

$$\mu_{x_i}, local = \mu_{x_i}^{2} \quad for\ \ x_i \ge x_0$$

$$Global:\ \mu_{x_i}, global = \mu_{x_i}^{2} \quad for\ \ x_i \le x_0$$

$$\mu_{x_i}, global = \mu_{x_i}^{1/2} \quad for\ \ x_i \ge x_0$$

Where, x_i = condition rating (0–5) and x_0 = condition rating where MF is maximum

Step 6: Each distress can be assigned with applicable MFs and the generalized fuzzy rule will be formulated. In order to account for the combination of defects, a combined MF has to be developed using the following steps. MFs are initially rescaled using the following relation.

$$x_i^{j'} = \frac{x_i^j}{a - x_i^j}$$

Where $x_i^{j'}$ = scaled condition rating for i[th] MF at j[th] distress; x^j_i= unscaled condition rating for i[th] MF at j[th] distress and a = spread of the universe of discourse ≈5.

Step 7: Further, by using the vertex method (Dong and Shah, 1987), the scaled MFs are aggregated to obtain combined MFs as given by,

$\mu_i \mid x_i^{j'}$ for

$\mu_i \in \{0,0.1,0.2,.....0.9,1.0,1.0,0.9,0.8,.....,0.2,0.1,0\}$

Where, $x_i^{j'} = \sum_j x_i^{j'}$ = aggregation of MF on a modified scale.

Finally, the scaled MFs are reverted to the original scale using equation below,

$$x_i^{j'} = \frac{a x_i^j}{1 + x_i^j}$$

where x_i = Original scale rating corresponding to MF value μ_i

Step 8: After formulating the combined distress effects, defuzzification is carried out using the centroid method (Madau and Feldkamp, 1996). The centroid is calculated based on the following formula,

$$Centroid = \sum_{i=1}^{n} \frac{1/6 (x_{i+1} - x_i)(2x_i y_i + x_{i+1} y_i + x_i y_{i+1} + 2x_{i+1} y_{i+1})}{0.5(x_{i+1} - x_i)(y_i + y_{i+1})}$$

Where x = Condition rating, y= degree of MFs, i = number of areas which varies from 1 to 'n'

Appendix B

Endurance Limit Calculation:

1) Trial 1
16 × 5.4 CF Propeller
Tested data – At 50% throttle 10.3 amps required to attain 1.8 kg thrust,
So, 10.3 amps × 8 motors = 82.4 amps
(20 /82.4) × 60 = 14.5 mins
Therefore, endurance = 14.5 mins at 50% throttle

2) Trial 2
15 × 5 CF Propellers
Tested data – At 50% throttle 9.3 amps required to attain 1.6 kg thrust,
So, 9.3 amps × 8 motors = 74.4 Amps
(20 /74.4) × 60 = 16 mins
Therefore, endurance = 16 mins at 50% throttle

3) Trial 3

17 × 5.8 CF Propellers
Tested data – At 50% throttle 7.1 amps required to attain 1.1 kg thrust,
So, 7.1 amps × 8 motors = 56.8 Amps
(20 /56.8) × 60 = 20 mins
Therefore, endurance = 20 mins at 50% throttle

Appendix C

Matlab Codes

Acquisition of Images from Videos

```
vid = videoinput('winvideo', 1, 'YUY2_720x576');

src.AnalogVideoFormat = 'pal_d';

vid.ReturnedColorspace = 'rgb';

vid.FramesPerTrigger = 1;

preview(vid);
```

BHT Transform

```
function [bht]=bhttransform(it)

it=im2double(rgb2gray(it));

se=strel('square',4);

iht=ones(size(it))-imbothat(it,se);

bht=im2bw(iht,0.89);

figure, imshow(bht);

end
```

HSV Threshold

```
function hs=hsvthresh(i1)

i1=rgb2hsv(i1);
```

```
imshow(i1);

ih=i1(:,:,3);

ih1=i1(:,:,2);

[s1 s2]=size(ih);

for m=1:s1
   for n=1:s2
      if (ih1(m,n)>0.1 && ih(m,n)<0.3)
         res(m,n)=0;
      else
         res(m,n)=1;
      end
   end

end

imshow(res);

end
```

Crack Identification Function

```
Y=rgb2grayscale(I)

[~, threshold] = edge(Y, 'sobel');
fudgeFactor=2.4;

BWs = edge(Y,'sobel', threshold * fudgeFactor);

figure, imshow(BWs), title('Crack identification');
```

Crack Properties Function

```
function [BW_out,properties] = filterRegions(BW_in)
%filterRegions  Filter BW image using auto-generated code from imageRegionAnalyzer app.
%  [BW_OUT,PROPERTIES] = filterRegions(BW_IN) filters binary image BW_IN
%  using auto-generated code from the imageRegionAnalyzer App. BW_OUT has
%  had all of the options and filtering selections that were specified in
%  imageRegionAnalyzer applied to it. The PROPERTIES structure contains the
%  attributes of BW_out that were visible in the App.
```

```
% Auto-generated by imageRegionAnalyzer app on 27-Jan-2018
%------------------------------------------------------

BW_out = bwareafilt(BW_in, 1000);

% Get properties.
properties = regionprops(BW_out, {'Area', 'Eccentricity', 'EquivDiameter', 'EulerNumber', 'MajorAxisLength', 'MinorAxisLength', 'Orientation', 'Perimeter'});

% Uncomment the following line to return the properties in a table.
% properties = struct2table(properties);
```

Appendix D

Table 21: Concrete Mix Design

Materials (kg)	**Proportion**
Cement	276
Fly Ash	69
Sand	815
Aggregates	1055
Water	148
Water Reducing Agent (gms)	1883
Air Entraining Agent (gms)	123

Curing Time- 28 days